Structural and dynamic properties of hybrid organolead perovskites for photovoltaic applications

Afonso da Cunha Ferreira

DOCTORAT MATIERE BRETAGNE MOLECULES LOIRE ET MATERIAUX

INSA RENNES

THESE DE DOCTORAT DE

L'INSTITUT NATIONAL DES SCIENCES APPLIQUEES RENNES

ECOLE DOCTORALE N° 596
Matière, Molécules, Matériaux
Spécialité : Sciences des Matériaux

Par
Afonso DA CUNHA FERREIRA

Structural and dynamic properties of hybrid organolead perovskites for photovoltaic applications

Thèse présentée et soutenue au LLB Saclay le 16 Juin 2020
Unité de recherche : LLB, CEA Saclay / FOTON, INSA Rennes

Rapporteurs avant soutenance :

Stéphane PAILHÈS	Chargé de recherche, CNRS, ILM Lyon
Emmanuelle DELEPORTE	Professeur, ENS Cachan

Composition du Jury :

Président :	Bernard HEHLEN	Professeur, Uni. Montpellier II
Examinateurs :	Stéphane PAILHÈS	Chargé de recherche, CNRS, ILM Lyon
	Emmanuelle DELEPORTE	Professeur, ENS Cachan
	Claudine KATAN	Directeur de recherche, CNRS, ISC Rennes
	Bernard HEHLEN	Professeur, Uni. Montpellier II
Dir. de thèse :	Jacky EVEN	Professeur, INSA Rennes
Co-dir. de thèse :	Philippe BOURGES	Directeur de recherche, LLB Saclay

UNIVERSITE MATIERE BRETAGNE MOLECULES LOIRE ET MATERIAUX

INSA RENNES

Intitulé de la thèse :

Structural and dynamic properties of hybrid organolead perovskites for photovoltaic application

Afonso DA CUNHA FERREIRA

En partenariat avec :

Foreword

There is an ever-growing need to address both energy and environmental issues, product of generations of over-exploitation of fossil fuel sources and the increased associated industries, which represent one of the most beneficial and, at the same time, injurious aspects of modern times. Solar energy emerges as a renewable and cleaner alternative energy source, with still a lot of possible room for improvement. Photovoltaic (PV) technology requires materials with high efficiencies, simple processability, low cost and abundant availability on Earth. In the effort of developing new generation PV cells, halide organolead perovskites (HOPs) represent a promising opportunity for incorporating all these requirements.

The general chemical formula for describing perovskite materials is ABX_3, where the A and B sites are occupied by two cations of different sizes and X is an anion. The X-site anion coordinates with the B-site cation to form a corner-sharing network of BX_6 octahedra, resulting in a three dimensional (3D) framework, in which the A-site cations are located in its cavities. HOPs are a subclass of ABX_3 perovskites, where the A, B and X sites correspond to an organic cation, lead and an halide ion, respectively. The incorporation of organic components in the structure of these HOPs introduce additional functionalities and structural flexibility that cannot be achieved in purely inorganic perovskites. After just a decade of material engineering and device optimization, HOP based solar cells already achieve power conversion efficiencies (PCE) of above 25%.

Despite their huge impact on photovoltaics and other optoelectronic applications, only a handful of HOPs that have been discovered so far, are available for use, due to stability requirements in crystal structure formation. The B-site cation is mainly limited to the group IVA metals lead (Pb) and tin (Sn), with divalent charge, and the X-site anion is chosen from the halides Cl^-, Br^- and I^-. The resulting BX_3^- frameworks can thus only accommodate the smallest organic cations, such as methylammonium (MA) and formamidinium (FA), according to the Goldschmidt tolerance factors.

This project focuses on the study of such HOP compounds, namely $MAPbBr_3$, $MAPbI_3$ $FAPbBr_3$ and $FAPbI_3$; from now on referred to as MAPB, MAPI, FAPB and FAPI, respectively. For such a purpose, we heavily rely on inelastic neutron scattering (INS) spectroscopy, as it allows to systematically probe intrinsic properties of these HOPs, which have not been thoroughly investigated so far.

Purpose of the thesis

The structural and chemical variability of HOPs offers substantial opportunities for tuning and modulating their physical properties by facile chemical modification. As a result, besides low cost and low temperature processability, they benefit of various

optoelectronic features such as suitable optical band gap, superb optical absorption across the visible spectrum, low exciton binding energies and long charge-carrier diffusion lengths. These are the fundamental factors that have allowed such rapid success. However, while significant progress on perovskite film synthesis and device architecture engineering has been made, fundamental understanding of these underlying mechanisms related to charge-carrier dynamics remains scarce. Furthermore, the origin of the softness that characterizes HOPs and its influence on the charge carrier dynamics is still lacking a comprehensive understanding and systematic experimental studies.

Study of the lattice dynamics is indeed key in understanding the electron-phonon interactions (EPIs) at play, which are strongly connected to the aforementioned optoelectronic properties. The mobilities of charge-carriers are rather modest when compared to classical inorganic semiconductors and the phonon scattering mechanism setting the limit is still under debate. Besides, atomic-level description of these materials is hindered by the hybridized nature of phonon excitations in the organic and inorganic sub-lattices, which interact with each other via hydrogen bonding. Furthermore, the optical phonon modes partially related to the organic cations seem to overlap with acoustic modes and influence phonon up-conversion efficiencies of the reported hot-phonon bottleneck effect in HOPs. Measurement of the full phonon spectrum becomes then important to shine some light on some of these dynamics. Also, HOPs are known to undergo successive phase transitions as a function of temperature, evolving typically from a high temperature cubic phase, passing by a tetragonal phase down to a low temperature orthorhombic symmetry, on cooling. Many important properties of perovskites are a consequence of these phase transitions and the cooperative behaviour of the A, B and X components. Although not an original goal of the project, we found ourselves in the need to perform some temperature-based studies to complete our analysis.

We address this problems by employing not only INS, but also Raman and Brillouin spectroscopy, to investigate lattice excitations (*i.e.* phonons) in the four of the most technologically relevant HOP compounds. By measuring dispersion curves of acoustic phonons we give a clear picture of the difference in softness between FA and MA based compounds and how it relates to their structural stability and their ultralow thermal conductivities. We also present here an extensive comparison of optical phonon excitations in the four different hybrid compounds, in which we carefully discuss mode attribution to the respective structural vibrations. In contrast to theoretical expectation and classical behaviour in standard semiconductors, the phonon modes show no dispersion, suggesting strong anharmonic behaviour and localization effects. Our results put into question the validity of the quasi-particle picture used for phonon simulation

and the present understanding of the Fröhlich interaction for carrier mobilities, and may help solving the apparent paradox of acoustic-like temperature dependence of the charge-carrier mobilities.

Organization of the thesis

The manuscript is composed by five chapters. In the first, we start by introducing hybrid perovskites, specifically hybrid organolead halide perovskites (HOP), and the evolution of perovskite based photovoltaic technology, since its first implementation in 2009, up to nowadays. Then we discuss the structural characteristics of HOPs, their optoelectronic properties and how these two correlate, not only with each other, but also with the efficiency of solar cell devices.

In the second chapter we go over the characterization techniques employed to study our samples, namely neutron, Raman and Brillouin scattering spectroscopy. A big emphasis is given to neutron scattering. Then, we introduce the properties of neutrons and the advantages of neutron scattering in material analysis, its underlying principles are outlined. We present the main theoretical concepts and results on which our measurements of phonons and analysis are based upon, such as elastic and inelastic scattering and the response function. The end of the chapter consists on the explanation of the instrumentation used and experimental setups.

The remaining half of the thesis concerns the obtained results and has been divided in three chapters, regarding the high temperature (i), low temperature (ii) and temperature-dependent (iii) data:

(*i*) In the first section we investigate the low frequency structural excitations in the cubic phases of the four compounds, via neutron scattering and Brillouin spectroscopy. By measuring dispersion curves of acoustic phonons we are able to present a complete set of elastic constants for all four compounds and relate them, along with the corresponding sound velocities, to properties such as thermal conductivity and hot carrier relaxation, which are expected to be enhanced by lattice softness. Our results also indicate that the charge-carrier mobilities in HOPs are governed by interactions with optical phonons rather than acoustic ones, supporting previous claims.

(*ii*) Next, to better understand the electron-phonon interactions at play in the various optoelectronic properties of these HOPs, the optical phonon spectrum at 5 K (and up to a certain temperature) has been measured, via both INS and Raman spectroscopy. In contrast to theoretical expectation and classical behaviour in standard semiconductors, the phonon modes show no dispersion, attributed to the anharmonicity and suggesting localization effects. These flat modes appear at energies as low as 2-5 meV, merging with the high part of the acoustic phonon branches. This overlap

could part of the explanation for the relatively low mobilities. The dispersionless nature of these optical modes also implicates a glassy-like thermal conductivity, important to the hot-phonon bottleneck effect in HOPs.

(*iii*) Lastly, we study the temperature behaviour of the four compounds. We follow their temperature phases and we examine how their lattice dynamics evolve with temperature. Room temperature spectra, both from Raman and INS, reveal strong phonon overdamping in all momentum space, as a result of intrinsic lattice anharmonicity, which becomes overwhelming at temperatures as low as 80-100 K. Raman response of the lowest frequency mode of each perovskite, as a function of temperature, highlights a unified picture of the vibrational properties in all the four samples.

We end with the concluding remarks, where we briefly touch on the current state-of-the-art and the obstacles/routes for improvement.

Resumé

Motivé par les questions environnementales et de l'énergie, les pérovskites hybrides organo-plombiques (HOP) ont attiré beaucoup d'intérêt dans le domaine des cellules photovoltaïques. Actuellement, l'état de l'art des cellules solaires HOP est basé sur des alliages où le méthylammonium (MA) et le formamidinium (FA) sont tous deux présents dans la même structure et environ 10% sont remplacés par des atomes de rubidium (Rb) et de césium (Cs), ainsi que un alliage concomitant d'halogènes iode(I)/brome(Br), on peut atteindre désormais des rendements de conversion de puissance supérieurs à 25.2%. Ce projet se concentre sur l'étude de plusieurs composés HOP, à savoir $MAPbBr_3$, $MAPbI_3$, $FAPbBr_3$ et α-$FAPbI_3$; dans ce manuscrit par MAPB, MAPI, FAPB et FAPI, respectivement. Pour ce faire, nous nous appuyons beaucoup sur la spectroscopie de diffusion inélastique de neutrons (INS), car elle permet de sonder systématiquement les propriétés structurales de ces matériaux. Aucune étude systématique n'a été effectuée précédemment.

La structure spécifique de ces composés de formule générique ABX_3 est une structure péroskite qui consiste en un sous-réseau de PbX_6^{3-} octaédrique (X = I, Br ou Cl) à partage de coin, avec une stoechiométrie globale PbX_3^- et un sous-réseau de cations A^+ dans les vides cuboctaédriques. Ici, A = Cs, Rb, MA ou FA. Cette variabilité chimique et structurelle des HOP offre de nombreuses possibilités d'ajuster et de moduler leurs propriétés physiques par modification chimique. En conséquence, outre leur coût limité de recyclage et leur aptitude au traitement à basse température, ils bénéficient de diverses caractéristiques optoélectroniques telles que la bande interdite optique appropriée, une excellente absorption optique dans le spectre visible, de faibles énergies de liaison de l'exciton et une diffusion importante des porteurs de charge. Ce sont les facteurs fondamentaux qui ont permis un succès aussi rapide. Cependant, bien que des progrès significatifs aient été réalisés en matière de synthèse de film de pérovskite et d'ingénierie d'architecture de dispositifs, la compréhension fondamentale de ces mécanismes sous-jacents liés à la dynamique des porteurs de charge reste rare. De plus, l'origine de la faible dureté qui caractérise les HOPs et de son influence sur la dynamique des porteurs de charge manque encore d'une compréhension globale et d'études expérimentales systématiques.

En utilisant la diffusion inélastique de neutrons (INS), les dispersions des phonons acoustiques ont été mesurées autour des principales réflexions de Bragg dans MAPB, FAPB, MAPI et FAPI. Des expériences complémentaires de diffusion de la lumière de Brillouin (BLS) ont également été utilisées pour déterminer la vitesse du son dans les composés à base de brome. Cela nous permet de déterminer les constantes élastiques qui caractérisent leur structure dans la phase cubique. En prenant la position de

Bragg (200) à titre d'exemple, les modes de phonons acoustiques longitudinaux (LA) et acoustiques transversaux (TA) ont été mesurés à différentes positions réciproques $Q = (200) + q$ en unités HKL, avec q le long de [200] en géométrie longitudinale (LA) et perpendiculaire en géométrie transverse (TA) (pour TA, q est parallèle à [011]). Des modes de phonons acoustiques sont clairement visibles sur un bruit fond important, qui résulte d'une diffusion quasi-élastique provenant de la diffusion incohérente des atomes d'hydrogène présents dans les molécules MA/FA. Tous les spectres de diffusion de neutrons de cette thèse ont été décrit en fonction de l'energie, $\hbar\omega$, et pour chaque vecteur d'onde Q avec un modèle d'oscillateur harmonique amorti (DHO).

A partir des spectres de neutrons et en faisant varier la distance q jusqu'au point de Bragg le plus proche, on peut tracer les courbes de dispersion de phonons reliant la fréquence/énergie ω en fonction de q. Pour les modes acoustiques, la pente de telles courbes nous donne les vitesses de propagation des phonons, à partir desquelles on peut obtenir les constantes élastiques correspondantes, via l'expression usuelle suivante reliant la vitesse du son, V, avec la constante élastique effective, C_{eff} (ρ est la densité du matériau): $V = \sqrt{C_{eff}/\rho}$. C_{eff} dépend de la direction de propagation en question. On peut obtenir de C_{eff}, via certaines combinaisons, le module de Young (C_{11}), la constante élastique transverse (C_{12}) et le module de cisaillement (C_{44}). Ensuite, celles-ci permettent également de déduire d'autres paramètres structurels tels que le module d'élasticité isostatique (K) et l'indice d'anisotropie de Zener (A).

De cette façon, nous avons mis en place un ensemble complet fiable de constantes élastiques, pour la première fois via INS, pour les quatre composés HOP les plus pertinents - avec un accent particulier sur FAPI, peu étudié dans la littérature en raison de son caractère métastable. En fait, cela se reflète par une constante C_{12} négative et un module d'élasticité très faible. Néanmoins, nous notons un module de cisaillement faible C_{44} $\sim$4 GPa dans les quatre composés HOP et des paramètres C_{11} et K qui diminuent sensiblement avec l'augmentation de la constante de réseau, conduisant à une image de plus faible élasticité pour les composés à base de FA qu'avec MA.

De plus, on observe dans les HOPs un effet de "goulet d'étranglement des phonons" (*hot phonon bottleneck*), un phénomène dans la thermalisation des porteurs de charges qui consiste en la conversion des phonons acoustiques vers les modes optiques de basse énergie, qui recycle l'énergie thermique (vibrationnelle). Cela a pour conséquence de réchauffer les porteurs de charge et de prolonger la durée de vie de porteurs chauds. Les mesures d'absorption transitoire ultra-rapide révèlent deux étapes du processus de refroidissement des porteurs. La première est liée à l'émission intrinsèque de phonons de Fröhlich mentionnée ci-dessous et ne varie pas de manière significative entre les différentes pérovskites. Lors d'une deuxième étape de refroidissement, la dynamique

porteur chaud-phonon se produit. À la température ambiante, le taux de relaxation porteur-phonon de la deuxième étape de refroidissement est généralement 3 à 4 fois plus lent en FAPI, comparé au système MAPB. Ceci est tout à fait compatible avec l'évolution de C_{11} et du module d'élasticité isostatique, mettant en relation directe le phénomène du goulet d'étranglement des phonons et des porteurs chauds dans les HOP avec leur faible rigidité élastique.

Par ailleurs, les courbes de dispersion des phonons acoustiques mettent également en évidence une vitesse de groupe sonore systématiquement plus faible dans les échantillons à base d'iode, ce qui devrait, en théorie, conduire à des mobilités de porteurs de charges plus faibles. Toutefois, tel n'est pas le cas. En fait, en examinant la corrélation entre la variation des constantes élastiques et la mobilité des porteurs (déterminée expérimentalement), ainsi que les études par les résultats d'élargissement de la photoluminescence (PL), il a été déduit que les phonons optiques, plutôt qu'acoustiques, dominent la diffusion des porteurs et les mobilités près de la température ambiante. En revanche, cette interprétation n'est pas cohérente avec l'observation d'une dépendance en fonction de la température de la mobilité de type acoustique, c'est-à-dire $\mu \propto T^{-3/2}$. Nous discutons par la suite ce problème à partir de l'étude du spectre complet des phonons optiques des HOP.

Pour ce faire, nous avons effectué des expériences systématiques d'INS à basse température, où nous avons mesuré le spectre de phonons optiques au point R $(1/2, 1/2, 3/2)$ pour la plupart des composés excepté FAPB où il est mesuré au point M $(5/2, 1/2, 0)$, avec des balayages à Q constant en fonction de l'énergie. Dans ces spectres, nous avons identifié trois gammes d'énergie différentes et rassemblé les modes ou ensembles de modes de chaque composé en trois catégories (a, b et c). A partir de nos données expérimentales et en accord avec la littérature, on en déduit les conclusions suivantes: *i*) Les modes, a, dans la plage des basses énergies (inférieure à 10 meV) sont associés aux vibrations du réseau PbX3, principalement des mouvements de basculement et de flexion. *ii*) En ce qui concerne la gamme d'énergie intermédiaire, modes b entre 10 et 20 meV, on observe une série de modes couplés entre les deux sous-réseaux organiques et inorganiques. Ils présentent donc une nature hautement hybride. *iii*) Au-dessus de 20 meV, les modes c optiques sont principalement associés aux mouvements moléculaires, bien qu'il puisse y avoir aussi des contributions inorganiques dans ces librations des cations, au moins pour les pérovskites contenant du MA. En outre, avec des mesures dans des directions de haute symétrie ($\mathbf{\Gamma} \rightarrow \mathbf{M}$ or $\mathbf{\Gamma} \rightarrow \mathbf{R}$) obtenues avec les spectromètres à trois-axes (TAS) et du facteur de structure dynamique $S(q, E)$ obtenu avec un spectromètre à temps de vol (ToF), nous observons peu ou pas du tout de dispersion des modes de phonons optiques (ou ensembles de modes).

Les spectres révèlent un certain nombre de caractéristiques jusqu'au plus basses énergies. Il a été récemment suggéré que la limite de mobilité imposée par la diffusion électron-phonon (processus de Fröhlich) est définie par les modes optiques longitudinaux (LO) de plus basse énergie (3-20 meV). Par conséquent, la présence de tels modes, observés systématiquement dans les quatre composés, semble favorisée cette explication pour la mobilité des porteurs, qui est relativement faible comparée aux semi-conducteurs inorganiques classiques, tels que Si et GaAs. De plus, il a été suggéré que les modes optiques plats (comme ceux que nous avons observés ici) se mélangent fortement avec les phonons acoustiques qui les croisent, conduisant à une conductivité thermique vitreuse. Généralement, une forte hybridation entre phonons est associée à l'anharmonicité. Par conséquent, non seulement la nature sans dispersion des modes optiques est responsable en grande partie du blocage de la propagation des phonons acoustiques, mais aussi du fort couplage anharmonique acousto-optique. Cet ensemble constitue des facteurs clés dans l'effet de goulet d'étranglement des phonons dans les HOPs, en facilitant la conversion acoustique des phonons et en augmentant la durée de vie de la population des porteurs chauds.

A partir des mesures en fonction de la température, on peut voir que cette anharmonicité se manifeste à des températures basses, bien inférieures à la température ambiante, où les dispositifs optoélectroniques et les cellules solaires sont généralement utilisés. Ces effets conduisent à un suramortissement plutôt rapide de certains modes de phonon à des températures aussi basses que 80 K, ce qui rend difficile d'attribuer correctement la contribution exacte de chaque mode de phonon au spectre global pour des températures plus élevées. L'amortissement des phonons observé ici semble être spécialement influencé par la transition tétragonale-orthorhombique, ce qui cadre bien avec l'affirmation bien établie selon laquelle les transitions découlent du basculement de la cage PbX_3 et de l'ordre d'orientation des molécules organiques, entraînée par des instabilités aux points M et R de l'espace réciproque. L'évolution des spectres montre également l'absence de modes mous particuliers au point M ou R, ce qui signifie qu'ils ne semblent pas se condenser avec la température et pointant vers une transition orthorhombique-tétragonale plutôt ordre-désordre. Alors que l'anharmonicité des pérovskites aux halogénures conduit à des phonons acoustiques basse fréquence, caractéristiques d'un réseau pas très rigide, elle se révèle aussi dans les phonons optiques par un comportement suramorti sur l'ensemble de la zone de Brillouin à la température ambiante. Le caractère anharmonique prépondérant des phonons optiques spécifiques aux pérovskites à halogénures est très probablement un point essentiel pour une description correcte de l'interaction porteurs-phonon de Fröhlich pour cette classe de semiconducteurs "souples".

A haute température, aucun mode phonon bien défini n'est observé par INS dans la gamme mesurée, chaque mode étant suramorti dans tout l'espace réciproque. Nous avons aussi utilisé la diffusion Raman pour mieux caractérise le comportement en température des quatre HOP à travers la transition cubique-quadratique qui a lieu à haute température (typiquement proche de la témpérature ambiante). Les spectres de la réponse Raman conduisent à la une description similaire de la dynamique structurale au centre de la zone de Brillouin des quatre composés, tout au long de leur transition cubique-quadratique. Les phonons sont aussi décrits par une somme de DHO. En particulier la fréquence, ω_1, ddu mode observé à plus basse fréquence reste constante avec la température, comme ce qu'on voit avec l'INS, suggérant à nouveau une transition non displacive. Dans le même temps, bien que la transition cubique-quadratique soit clairement marquée, elle est moins abrupte dans les échantillons contenant du Br, suggérant moins d'effets de pré-transitionnels dans ce dernier. De tels effets pré-transitionnels ont également été observés avec INS dans FAPB avec une tendance à une transition ferroélastique naissante qui est favorisée par le ramollissement du mode acoustique transversal associé à C_{44}.

En conclusion, dans ce travail, nous présentons une étude détaillée des excitations de réseau cristallin (phonons) dans les quatre composés HOP les plus pertinents sur le plan technologique dans le domaine du photovoltaïque. En mesurant les courbes de dispersion des phonons acoustiques, nous donnons une image claire de la faible élasticité. Nous présentons également ici une comparaison détaillée des excitations optiques dans les quatre composés différents, dans laquelle nous discutons avec soin de l'attribution des modes de vibrations structurales respectives. Contrairement aux attentes théoriques et au comportement classique des composés semi-conducteurs classiques, les modes de phonon ne montrent pas ou peu de dispersion, ce qui suggère un comportement anharmonique très fort et des effets de localisation. Ce comportement remet en question la validité de l'image de quasi-particule pour décrire les phonons utilisée dans l'interaction des porteurs de charges avec le réseau. Nos résultats mettent également en évidence le rôle du fort couplage anharmonique acousto-optique (responsable de la faible élasticité) dans la conductivité thermique faible, comme dans des phases vitreuses (glassy like) et l'effet de goulet d'étranglement des phonons dans les HOP.

Acknowledgments

First and foremost, I would like to thank both my supervisors Jacky Even and Philippe Bourges, for giving me the opportunity to participate in this project and do research in such an interesting field. Thank you for not only your scientific guidance and knowledge, but also patience over the course of my PhD. It was a pleasure to work with you.

Thank you to Serge for the great crystal samples, to Claude for the Brillouin expertise, to Antoine and Claudine for the overall input and to Benoit and Bernard for all the Raman measurements and having me in Montpellier. A thank-you note also to my matlab sensei, Jaehong Jeong, for the lunch conversations, the occasional after-work rides and for helping me every time I got stuck with my data processing.

To everybody from the Maison du Portugal. To the late night evenings in the kitchen, to the conversations about all the big questions in life, to the city excursions (and the drinking excursions) and of course to my ramen buddies. Even though the age gap grew larger with every generation that came and went, I've made friendships with amazing people with whom I've shared a lot of experiences. You have made my time here that much more memorable and meaningful.

I also have to show my gratitude to Paris. It has been a constant feature in these formative years. It is where I developed an interest in art and where I rediscovered my love for reading. It is a city that provides an endless stream of cultural experiences and, despite its inherent chaotic nature, presents the perfect place to immerse oneself and indulge in the little and fine things in life. All the exhibitions, the concerts, the lights, the cafés, the great wine, the sunsets at the canal, the late night walks, ... *If you are lucky enough to have lived in Paris as a young man, then wherever you go for the rest of your life, it stays with you, for Paris is a moveable feast.* I know its sort of an expected and cliché quote but, nevertheless, it is true. Merci Paris, et à bientôt!

Thank you to all my friends back in Portugal. Ao meu "gang" de Queijas (e arredores) e aos Basolhenses que me adoptaram (çim). Estamos todos a entrar numa fase diferente das nossas vidas, cheia de incertezas, e onde talvez já não nos veremos tanto como outrora. No entanto tenho a certeza que estas amizades perdurarão e que continuaremos cá todos por muitas mais temporadas, partilhando as coisas boas e más da vida.

And of course, last but most importantly, an unmeasurable thank you to my entire family. Sem o vosso apoio incondicional, e às vezes sofrido, nunca poderia ter vivenciado todas as experiências e aventuras (incluindo crises existenciais) que, em parte, fazem de mim quem eu sou hoje. Serão sempre o meu ponto de referência. Obrigado por tudo e espero um dia ser capaz de vos retribuir ♡

Abreviations

V_{oc}	open-circuit voltage
BLS	brillouin light scattering
BZ	Brillouin zone
CB	conduction band
DHO	damped harmonic oscillator
EPI	electron-phonon interactions
ETL	electron transporting layer
FA	formamidinium
FF	fill-factor
HOP	halide organolead perovskites
HTL	hole transporting layer
INS	inelastic neutron scattering
LA	longitudinal acoustic
LO	longitudinal optical
MA	methylammonium
PCE	power conversion efficiency
PL	photoluminescence
PV	photovoltaic
QE	quasi-elastic
RT	room temperature
TA	transverse acoustic
TAS	triple-axis spectrometer
TO	transverse optical

ToF	time-of-flight
VB	valence band
ZB	zone-boundary
ZC	zone-center

Nomenclature

κ	thermal conductivity, W/m·K
λ	wavelength, Å
μ	mobility, cm^2/V·s
ω	frequency, cm^{-1}
ρ	mass density, Kg/cm^3
υ	phonon velocity, m/s
$b_{coh} \mid b_{inc}$	scattering length, fm
C_v	specific heat, J/mol·K
D	diffusion coefficient, cm^2/s
$h \mid \hbar$	Planck constant | reduced Planck constant, J·s or eV·s
L_D	diffusion length, nm
M_d	molecular weight, g/mol
T_c	transition temperature, K

Contents

List of Figure

List of Tables

Chapter 1

Hybrid halide perovskites and photovoltaics

In this initial chapter, we will cover the implementation of hybrid halide perovskites in photovoltaic (PV) devices and their rapid evolution since then, up to the current state-of-the-art. Moreover, we introduce the general structural and optoelectronic properties of halide perovksites systems (e.g. lattice dynamics, charge and thermal transport, phase transitions) and how they correlate with each other and device performance.

1.1 History of perovskites

The origin of perovskite solar cells can be traced back to 1839, when a German scientist, Gustav Rose, during a trip to Russia, discovered a new calcium titanate-based mineral in the Ural Mountains, which was named "perovskite" after the Russian mineralogist Lev von Perovski [11]. Nowadays it applies as a description of the class of compounds sharing the same general stoichiometry and connectivity found in the mineral $CaTiO_3$, being that the terms "perovskite" and "perovskite structure" are often used interchangeably. This structure was first described by Victor Goldschmidt in 1926, in his work on tolerance factors [12], where the rules that govern the formation of such crystals were formulated.

Approximately half a century later, in 1893, the first series of synthetic perovskites, based on caesium and lead, was reported [13]. Unlike the naturally occurring mineral, these were prepared by a simple reaction of PbX_2 and CsX salts in aqueous solutions, and in which Wells *et al.* introduced halides in the X sites. Their RT tetragonal/orthorhombic and high-temperature cubic perovskite phases were later confirmed by X-ray diffraction [14, 15].

Meanwhile, in the start of the 1940s, barium titanate $BaTiO_3$, an oxide perovskite, had been discovered from doping studies of TiO_2 with BaO [16–20] and soon after the first detailed observation of its crystal structure was reported from Helen Megaw [21]. Research and development related to oxide perovskites flourished, leading to the introduction of these materials in the fabrication of various products, such as fuel cells, glass-ceramic articles, catalysts, gas sensors, heating elements, lasers and superconducting devices, in addition to increasingly popular multilayer capacitors [22–26].

In 1978, D. Weber at the University of Stuttgart in Germany developed the first organic-inorganic halide perovskite, in which methylammonium ions (MA) replaced the caesium cations (Cs) in the original metal halide compound synthesized by Wells [27, 28]. However, only in the early nineties, did the transition to perovskite optoelectronics happened. In a series of high profile papers, Mitzi and co-workers thoroughly described the optoelectronic properties of hybrid halide perovskites, emphasizing the opportunity of tuning the electrical properties by inserting an organic modulation layer [29, 30]. As the unique optical and electronic properties of perovskites became increasingly apparent, researchers began finding applications for halide perovskites as active layer in light emitting diodes (LED) and as semiconducting channels in thin film field-effect transistors (TFTs) [31–36].

As of today, it is their recent success as low-cost, tunable light absorbers in next-

generation PVs that is propelling interest in halide organolead perovskitess (HOPs). Their three-dimensional (3D) structures enabled the first low-cost PV components to be fabricated with power conversion efficiencys (PCEs) that have started to rival with the previous established technologies.

1.1.1 Perovskite based photovoltaics

Despite the long history of general research in perovskite materials, applying the materials for PV usage only took place very recently, having took off ever since. From the NREL efficiency chart in Figure 1.1, it is obvious the dramatic rise in efficiency that perovskite based solar cells have seen, and in such a relatively short period of time.

It is widely recognized that the first peer-reviewed perovskite solar cell (wwwwww) paper was produced by Tsutomu Miyasaka and his co-workers in 2009 [37]. The device based on a dye-sensitized solar cell (DSSC) architecture using liquid electrolyte, consisted of $MAPbBr_3$ and $MAPbI_3$ nanocrystalline self-assembled on mesoporous TiO_2 films, and yielded a conversion efficiency of 3.8% ($MAPbI_3/TiO_2$) (Fig. 1.2, left side). However, the redox-active liquid electrolyte used in the titania scaffold caused rapid perovskite degradation. With some adjustments in perovskite coating

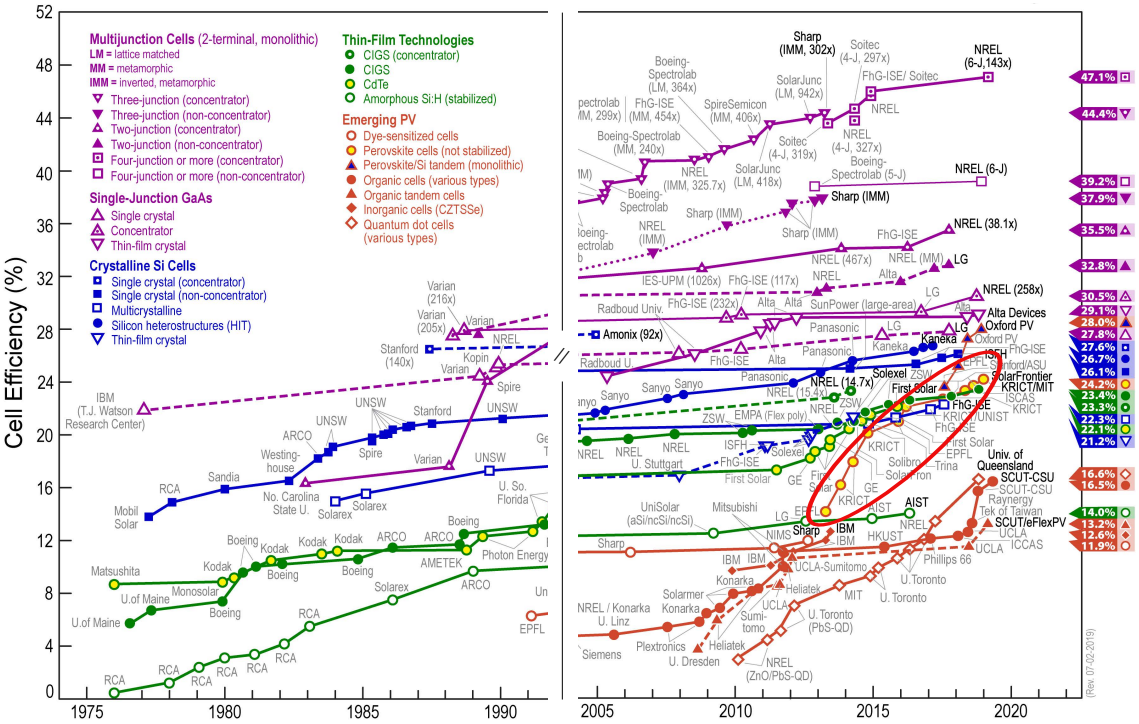

Figure 1.1: NREL solar cell efficiency chart (October 2019). The most recent world record for each technology is highlighted along the right edge in a flag that contains the efficiency and the symbol of the technology.

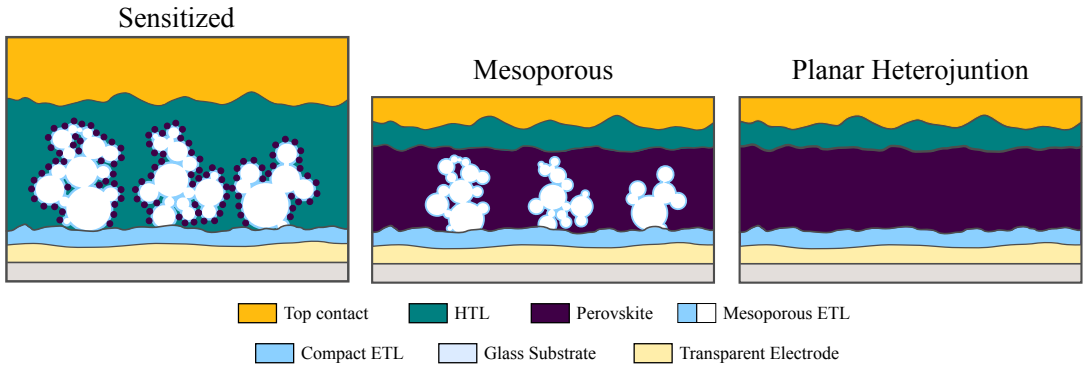

Figure 1.2: Different PSC architectures adopted since the first published report in 2009.

solution concentration, post-annealing conditions and TiO_2 surface modification, in 2011 Park *et al.* were able to improve efficiency to 6.5% PCE [38], although still using the same dye-sensitized concept.

A breakthrough came in 2012, with the first solid-state perovskite solar cell devices [39, 40], whence it was realized that the perovskite did not require the mesoporous TiO_2 layer in order to transport electrons. By introducing a stabilizing hole conductor spiro-OMeTAD, Nam-Gyn Park, Michael Gratzel *et al.* reported a 9.7% PCE [40], but slightly higher efficiencies (10.9%) were attained by Henry Snaith and his co-workers by additionally replacing the mesoporous TiO_2 with an inert Al_2O_3 scaffold [39] (Figure 1.2, center). This also led to the hypothesis that a scaffold is not needed for electron extraction, which was later proved correct. The realisation was then closely followed by a demonstration that the perovskite itself could also transport holes, as well as electrons [41]. Simple planar heterojunction solar cells, with no mesoporous scaffold (Fig. 1.2, right side), yielding PCEs above 10% were achieved soon after [42–44]. It should be noted that, nowadays, the line between planar and mesoscopic cell architectures is often difficult to draw. On one hand, the porous scaffolds in mesoscopic devices are much thinner than in initial designs. On the other hand, planar embodiments frequently employ nanocrystalline oxide films as an electron capture layer and the transparent electrodes are themselves highly corrugated. Despite the simpler structure of planar PSCs, designs that incorporate a mesoscopic scaffold still yield slightly higher efficiencies, mostly due to the improved charge collection.

The barrier of 20% was eventually surpassed in 2015, by a South Korea team [45]. Yang et al. achieved an efficiency of 20.2% using $FAPbI_3$, mostly due to its broader optical absorption as compared to $MAPbI_3$. Thereafter, a few others reported PCEs of >20% [46–52], which were achieved by tailoring the proportions of MA, FA, I, and Br to improve electronic properties. Since then, a lot of perovskite

solar cell research has been carried out all over the world, especially in Japan, South Korea, England, Switzerland, China, Spain and U.S., and as of today, the record stands at 25.2% for all-perosvkite based devices [53].
Currently, the state of the art of HOP solar cells is mainly based on alloys where methylammonium (MA) and formamidinium (FA) are both present in the same structure and ca. 10% are replaced by rubidium (Rb) and caesium (Cs) atoms, together with concomitant alloying of iodide (I)/bromide (Br) halogens [49]. Most planar PSCs are based on a transparent conducting oxide/ETL/perovskite/HTL/metal structure, where ETL and HTL refer to electron-transport and hole-transport layers respectively. In the so-called 'inverted' architecture, ETL and HTL layers positions are inverted. These HOP solar cell architectures exhibit somewhat lower efficiencies [54] but are less prone to hysteresis and may be a good alternative for monolithic HOP/Si tandem solar cells [55]. Typical hole-transport layers include Spiro-OMeTAD or PEDOT:PSS, and typical electron-transport layers include TiO_2 or SnO_2. In the case of mesoscopic architectures, a TiO_2 or Al_2O_3 scaffold is incorporated in the ETL layer (e.g. glass/fluorine-doped ITO/compact TiO_2/mesoporous TiO_2/perovskite/spiro-OMeTAD/Au). These architectures are exemplified in Fig. 1.2.

1.2 Structure Overview

Perovskite lends its name to the class of compounds that adopts the same ABO_3 three-dimensional (3D) structural framework as $CaTiO_3$. As illustrated in Fig. 1.3, the basic ABX_3 HOP structure is rather simple, consisting of a corner-sharing network of BX_6 octahedra (*i.e.*, BX_3), with the "A" cations occupying 12-fold coordinated voids within the cubo-octahedral cavity. In an ideal cubic unit cell, ion A sits at cube corner positions (0, 0, 0); ion "B" sits at body center position (1/2, 1/2, 1/2) and ion "X" sits at face centered positions (1/2, 1/2, 0). However, deviations from cubic symmetry can result from several factors, the first being size effects.

The Goldschmidt tolerance factor t [12], can be used to predict the stability of 3D perovskite structures given the ionic radii of components A(R_A), B (R_B), and X (R_X):

$$t = \frac{R_A + R_X}{\sqrt{2}(R_B + R_X)} \tag{1.1}$$

Empirically, the majority of 3D HOPs form in the approximate range $0.81 \leqslant t \leqslant 1.0$. A tolerance coefficient of 1.0 indicates the formation of an ideal ABX_3-type perovskite having a cubic crystal structure. If the tolerance coefficient is between 0.9

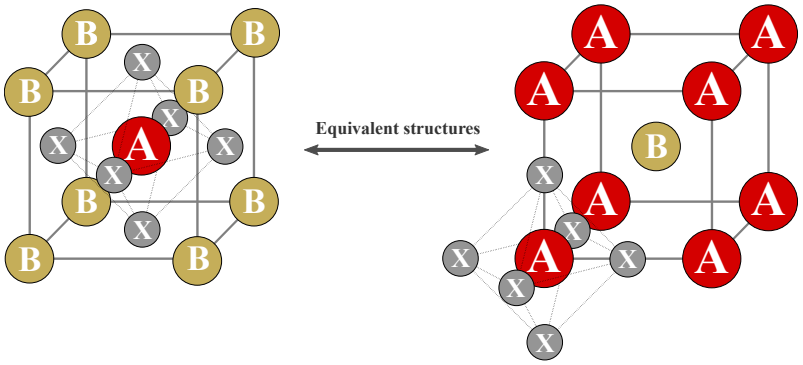

Figure 1.3: A generic perovskite crystal structure of the form ABX_3. Note that the two structures are equivalent – the left-hand structure is drawn so that atom B is at the (0, 0, 0) position while the right-hand structure is drawn so that atom (or molecule) A is at the (0, 0, 0) position. Also note that the lines are a guide to represent crystal orientation rather than bonding patterns.

and 1.0, the perovskite will form a cubic crystal structure. In the case of a t between 0.80 and 0.89, a distorted perovskite structure with an orthorhombic, tetragonal, or rhombohedral crystal structure is most likely to be formed. Whereas, if the value of t is less than 0.8, then the A cation is too small and a non-perovskite structure will form. A second constraint known as the octahedral factor, given by $\mu = R_B/R_X$ and can be used to estimate the stability of the BX_6 octahedra. For a value in the range of $0.44 \leqslant \mu \leqslant 0.9$, the metal halide perovskite has been found to be stable.

Cubic symmetry provides optimum electronic properties due to a high degree of ionic bonding. However, on a number of occasions, the perovskites end up as distorted variants of the ideal structure. In fact, even the $CaTiO_3$ mineral, is pseudo-cubic due to tilting of the octahedra caused by the mismatch of crystal components outside of the ideal tolerance range. This is one of the factors involved in a defining characteristic of general perovskite structure: phase transitions. HOPs have a propensity to undergo a series of crystallographic phase transitions [56–58], that can be modulated by temperature, pressure, and/or chemistry, the first evidence of which came from the X-ray investigations from Moller above mentioned, on $CsPbCl_3$ and $CsPbBr_3$ [14, 15]. The phase transitions are thermodynamically favoured, *i.e.* the symmetry of perovskites decreases with temperature, starting with the highest symmetry cubic phase ($Pm\bar{3}m$), with sequential transitions lowering this symmetry through octahedral rotations, typically passing by a tetragonal phase down to the low temperature orthorhombic phase[1].

Using $t = 1$ in equation 1.1, and essentially the largest values for R_B and R_X (*i.e.*, Shannon ionic radii $R_{Pb} = 1.19$ Å and $R_I = 2.20$ Å) [59], the limit on R_A is found to be approximately 2.6 Å for traditional BX_3 - frameworks with B = diva-

[1]More on phase transitions in section 1.3.2

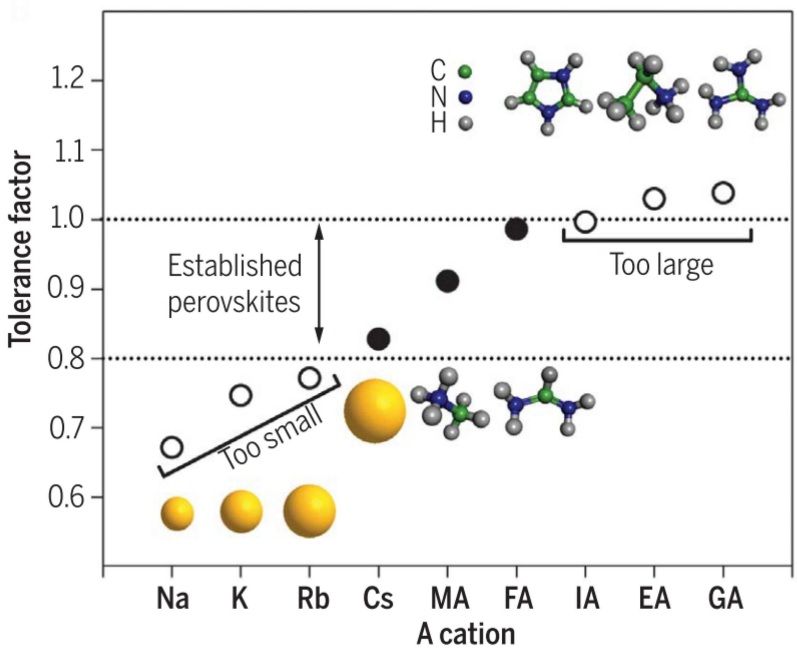

Figure 1.4: Tolerance factor of $APbI_3$ perovskite with A cations that are too small (Na, K, Rb), established (Cs, MA, FA), or too large [imidazolium (IA), ethylamine (EA), guanidinium (GA)]. The inset images depict the cation structures. Empirically, perovskites with a tolerance factor between 0.8 and 1.0 (dotted lines) show a photoactive black phase (solid circles) as opposed to nonphotoactive phases (open circles). Reprinted from [1].

lent metal and X = halogen. Besides ionic radii constraints, charge balance must also be achieved; that is, if the "A" cation is monovalent, then the "B" cation must be divalent if "X" is a halogen and all sites are fully occupied. So in fact, only three A cations known to date are able to stabilize the perovskite structure with heavy halides, namely caesium (Cs^+), methylammonium (MA^+) and formamidinium (FA^+) (Fig. 1.4). Therefore, typical organic-inorganic halide perovkites will be composed of a combination of the following elements:

- **A** = An organic cation - MA^+ or FA^+
- **B** = A big inorganic cation - usually lead (Pb_2^+)
- $\mathbf{X_3}$ = A slightly smaller halogen anion - usually chloride (Cl^-), bromide (Br^-) or iodide (I^-)

Aside from a clear difference in A species, inorganic versus organic, there is also a change in symmetry of the A site component from spherical (inorganic) to non-spherical (organic), which is particularly important in terms of orientational disorder and polarization.

Many researchers have used such conditional parameters to determine whether a combination of several ions can form a stable perovskite structure. Different types of perovkites alloys, *i.e.* mixed A-site($A_{1-x}A'_xBX_3$), B-site ($AB_{1-x}B'_xX_3$) and halide X ($ABX_{3-x}X'_x$), and combinations of those have all been explored to improve not only

material stability but also optical and electronic properties. The ability to modify the various components, that comprise the three lattice positions A, B and X, in a vast number of permutations, provides a useful parameter not only for space for engineering structure-property relationships, but also for facilitating development of multifunctional compounds with tunable physical, chemical, optical, and electronic properties. As a result, the range of electrical properties of perovskites is probably the widest physical property exhibited by a single class of material[2].

1.3 Structural stability and phase transitions

1.3.1 Born's criteria for stability

The fundamental understanding of the conditions of mechanical stability of unstressed crystalline structures were first tackled thoroughly by Max Born and his co-authors. In his 1954 book [60], the generic requirements for elastic stability of crystal lattices have been laid down and nowadays the corresponding equations are often called the "Born stability criteria".

The elastic behaviour of a lattice are described by its matrix of second-order elastic constants

$$C_{ij} = \frac{1}{V_0}\left(\frac{\partial^2 E}{\partial \epsilon_i \partial \epsilon_j}\right) \tag{1.2}$$

where E is the energy of the crystal, V_0 its equilibrium volume and ϵ denotes strain. This elastic matrix (also called stiffness matrix) has a 6×6 size, is symmetric and it is composed of 21 independent components. The crystal class of the material considered yields additional symmetry constraints, further reducing the number of independent elastic constants.

For a lattice to be stable (i) all its phonon modes need to have positive frequencies for all wave vectors (dynamical stability), and (ii) the free energy must be represented by a positive defined quadratic form (elastic stability criterion). From these set of prerequisites, one can deduce some necessary and sufficient elastic stability conditions for the three more relevant crystallographic systems for the present work.

Cubic system

The cubic crystal system has the simplest form of elastic matrix, with only 3 independent constants: C_{11}, C_{12} and C_{44}. The three Born stability criteria for the cubic

[2]These will be discussed in section 1.4

system are then the following

$$C_{11} - C_{12} > 0 \ ; \ C_{11} + 2C_{12} > 0 \ ; \ C_{44} > 0 \tag{1.3}$$

The first condition can be also equivalently stated as $C_{11} > |C_{12}|$.

Tetragonal system

Crystals of the tetragonal (I) class ($4/mmm$) have 6 independent elastic constants. One derives the four necessary and sufficient conditions for elastic stability

$$\begin{cases} C_{11} > |C_{12}| \ ; \ 2C_{13}^2 < C_{33}(C_{11} + C_{12}) \\ C_{44} > 0 \ ; C_{66} > 0 \end{cases} \tag{1.4}$$

The tetragonal (II) class ($4/m$) features an extra elastic constant, C_{16}, bringing the total of independent C_{ij}'s to 7 and consequently, the necessary and sufficient Born stability criteria for tetragonal (II) class slightly change to

$$\begin{cases} C_{11} > |C_{12}| \ ; 2C_{13}^2 < C_{33}(C_{11} + C_{12}) \\ C_{44} > 0 \ ; 2C_{16}^2 < C_{66}(C_{11} - C_{12}) \end{cases} \tag{1.5}$$

Orthorhombic system

Finally, the stiffness matrix for an orthorhombic crystal has 9 constants and no relationships between them. The necessary and sufficient Born criteria for an orthorhombic system are

$$\begin{cases} C_{11} > 0 \ ; \ C_{11}C_{22} > C_{12}^2 \\ C_{11}C_{22}C_{33} + 2C_{12}C_{13}C_{23} \\ \qquad -C_{11}C_{23}^2 - C_{22}C_{13}^2 - C_{33}C_{12}^2 > 0 \\ C_{44} > 0 \ ; C_{55} > 0 \ ; \ C_{66} > 0 \end{cases} \tag{1.6}$$

The conditions obtained are not all linear, but polynomial functions of the elastic constants (because the largest non-diagonal block in the stiffness matrix has a 3 x 3 size and all coefficients are independent).

1.3.2 Structural phase transitions

A phase transition can be driven by many parameters - temperature, pressure, chemical composition, magnetic or electric field, etc. If the driving parameter is tempera-

ture, the high-temperature phase is almost always more disordered, *i.e.* has a higher symmetry than the low-temperature phase. In such cases, phase transitions entail a change in the entropy of the system. That change can be either continuous or discontinuous. In the first case, the phase transition is continuous across the transition temperature (or other transition parameter). The thermodynamic quantities are continuous, but their first derivatives are discontinuous. In particular, the specific heat has a pronounced anomaly and the thermal expansion coefficient has a step at the transition. In the latter case, the phase transition is accompanied by release of heat (latent heat), and all the other thermodynamic quantities (internal energy, entropy, enthalpy, volume, etc.) are discontinuous as well. Such a phase transition is known as first-order transition.

Symmetry classification

The term distortive covers all the cases where the phases of a crystal are regarded as derived from a certain super-group symmetry called the prototype [61], which is the highest conceivable crystallographic symmetry from which a given phase can result by a small distortion. Phase transitions in this classification are therefore not always between two consecutive phases, but between the prototype and the phase under consideration. All phase transitions in crystals can be divided into two categories: isomorphous phase transtitions and non-isomorphous phase transtitions. In the former, there is no change in the space-group symmetry of the crystal. In a non-isomorphous phase transition the change of space-group symmetry can be either nonferroic or ferroic. In a non-ferroic phase transition there is a change in only the translational symmetry, but no change in the point-group symmetry [62]. Ferroic phase transitions involve a change of the point-group symmetry with or without a change of the translational symmetry. If there is a change of the point-group symmetry but no change of the crystal system the phase transition is defined as non-ferroelastic. A change of crystal system becomes a necessary as well as a sufficient condition for a phase transition to be called ferroelastic [63].

Order-disorder phase transitions

In the simplest case, an order-disorder phase transition occurs when the low temperature phase of a system shows a regular (alternating) pattern of atoms with long-range correlations, but the high-temperature phase has atoms arranged randomly with no long-range correlation. As a measure of long-range correlation one defines the order parameter η. This is usually normalised such that it is unity for a maximally ordered state and zero for a totally disordered state. This can be under-

stood most easily in the case of an AB alloy, for example, in which the structure can be divided into two sub-lattices α and β. In such a framework all A atoms reside on α sites and all B atoms reside on β sites, in the ordered ground state. As the temperature increases, the phase becomes progressively disordered, with more and more A atoms moving to the B sub-lattice and vice versa until, at the transition temperature (T_c), the disordering becomes complete, with the A and B atoms distributed equally over both sub-lattices. At this point, the two sub-lattices become indistinguishable, the long range order disappears, and the structure becomes a new one.

Displacive phase transitions

Displacive phase transitions are, as the name suggests, transitions driven by the continuous displacements of atoms or ions. Naturally, the relevant phonon modes will be displacive, *i.e.* in displacive phase transitions the modes that drive the transitions are the same phonon modes driving the lattice dynamics. However, we are discussing very different timescales: phase transitions typically occur in a matter of seconds, whereas typical phonon frequencies are in the THz range. Nevertheless, most displacive phase transitions have a dynamical character, and are caused by softening and "freezing" of a particular phonon. This means that the frequency of a particular phonon - either an optical zone-center (ZC) phonon or an acoustic zone-boundary (ZB) phonon - starts to decrease as the phase transition is approached (the phonon "softens"), until the frequency reaches zero at the phase transition. At this point, the phonon is "frozen", *i.e.*, it is no longer dynamical. It has, in fact, transformed into a static displacement pattern - exactly the mode we need to describe a symmetry lowering through the phase transition. Close to the phase transition, the phonons become highly anharmonic at the critical point Brillouin zone, but the crystal as a whole remains rather harmonic, and the thermal expansion anomalies are typically small. Below the phase transition, the quasi-harmonic character of all lattice vibrations is restored through one the following ways:

- ZC phonons: in this case, the optical ZC phonon softens completely at the phase transition, and then hardens again below it, as the system finds a new dynamical equilibrium around the distorted structure. The periodicity of the structure is unchanged through the phase transition.
- ZB phonons: When the distortion is driven by a ZB phonon, the distorted structure will have a larger unit cell (the translational symmetry is broken). The ZB point will then "fold" to the new ZC, and the soft phonon will harden below the phase transition to become a new ZC phonon.

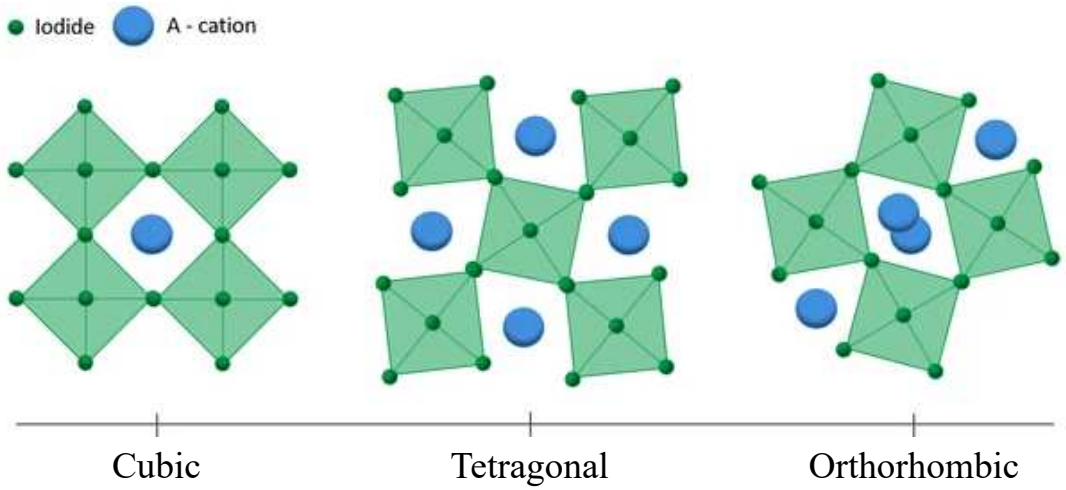

Figure 1.5: Illustration of the possible crystal structures of HOPs.

1.3.3 Phase transitions in HOPs

HOPs typically assume one of three lattice structures: cubic, tetragonal and orthorhombic. These are illustrated in Fig. 1.5. The displacements of the A- and B-sites, and the tilting of the BX_6 octahedral units are the primary factors that cause structural distortions [64, 65]. As the octahedral tilting usually has a much greater effect on lattice parameters, it has been used to classify the allowed symmetry changes of perovskites [66]. For HOPs in which the X-sites are halides, it is apparent that their octahedral tiltings are similar to those in pure inorganic perovskites. Inevitably, the much larger X-sites in HOPs offer additional space for the octahedra to distort. In some cases, adjacent octahedra can even distort along the same orientation, adding new tilting possibilities that are inaccessible in perovskite oxides [67, 68]. In addition to the octahedral tilting of the B-sites, the displacements of the A-sites and the dynamic motions of the A-sites and/or X-sites need to be taken into account for the symmetry description of HOPs. The displacements usually involve off-centre motions, although the situation is complicated by the presence of organic cations rather than single atoms on the A-sites. The dynamic motion of the organic A-site (occasionally also occurring on the X-site) is defined as stochastic, and switching from dynamic disorder to frozen orientations can induce symmetry changes, as we explained. Free MA and FA cations do not have the symmetry required for the cubic and tetragonal phases and, hence, often have to be orientationally disordered to stabilize those particular symmetries [69, 70]. The rotation of the A-site organic amine cations is more restricted in the lowest temperature phases of each compound, rotating only around the C–N axis, if at all [71]. In contrast to their oxide counterparts, the MA and FA cations interact with the

perovskite framework through N–H$\cdots$I hydrogen bonding, in addition to the electrostatic force, which consequently affects their phase transitions, octahedral tilting and disorder.

Transition sequences

A general view of the temperature-dependent structures is given in Fig. 1.6. $MAPbI_3$ and $MAPbBr_3$ have been reported to undergo a phase transition from an orthorhombic (Pnma) to a tetragonal structure (I4/mcm) between 140 and 165 K. A further phase transition to the cubic phase ($Pm\bar{3}m$) follows at higher temperatures at ∼330 K for $MAPbI_3$ and ∼240 K for $MAPbBr_3$ [56, 57, 72]. In fact, $MAPbBr_3$ shows an additional intermediate tetragonal (P4/mmm) phase between 145-155 K. $FAPbBr_3$ undergoes the same sequence of phase transitions but these occur between 275-250 K (cubic to tetragonal) and 150-125 K (tetragonal to orthorhombic) [73]. Now, $FAPbI_3$ is a more complicated case where there is still some debate about its structural phases. $FAPbI_3$ crystallizes in a black α phase at high temperatures, which then tends to spontaneously transform, with time, to a more stable, non-perovskite, yellow δ-phase structure (hexagonal)[3] [74, 75]. There seems to be an agreement that FAPI undergoes a α-β transition (2nd order) at around 150 K [70, 76–78]. Here, the α and β phases are either cubic (Pm3m) [74, 77, 79] and trigonal (possibly P4/mbm [77]), or trigonal (P3m1) and trigonal (P3) [70, 76, 78]. Nevertheless, for experimental purposes, we have assumed a pseudo-cubic phase structure. At lower temperatures it has been further postulated that a further γ phase exists, although as of today, no structure has been determined [70, 78].

In general, the high-temperature phase transitions are of second-order, and the

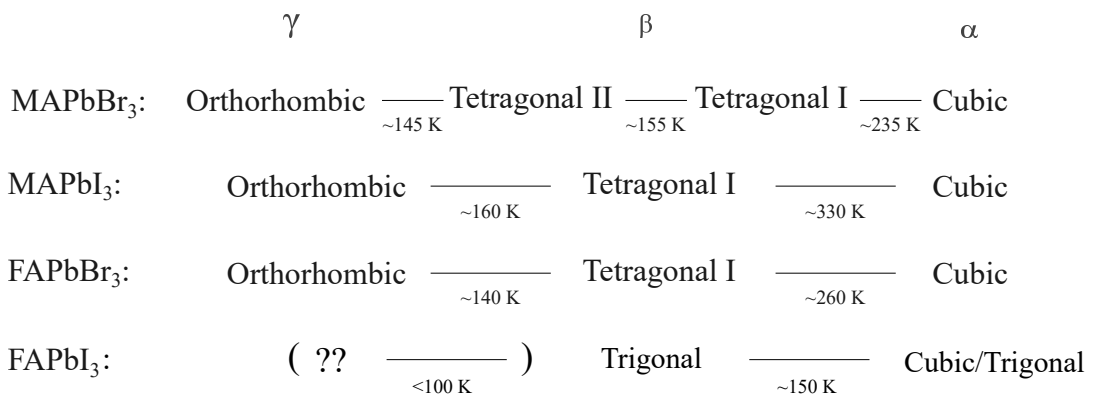

Figure 1.6: Simplified overview of the structural phases adopted at different temperatures by $MAPbBr_3$, $MAPbI_3$, $FAPbBr_3$ and $FAPbI_3$.

[3] This will pose some complications for the measurements (see section 2.6 in chapter 2)

low-temperature transition to the orthorhombic phase below 140–160 K, more so for MA- than FA-based compounds, is typically associated with larger energetic shifts as it marks a strong reduction in the extent of rotational freedom of the organic cation [66, 80–84].

The exact mechanisms of the above mentioned phase transitions are an extensive topic and their correlations with the optoelectronic properties of HOPs is still a subject of debate. The temperature behaviour and phase transitions of the compounds in question are addressed in chapter 5, where temperature-dependent measurements from both neutron and Raman spectroscopy are presented.

1.3.4 Lattice vibrations

In a lattice structure, atoms can oscillate around their equilibrium positions as a result of thermal energy. This leads to lattice vibrations. The position of the moving ion r(R) deviates from its average value R and we may write at any given time: r(R) = R + u(R), where u(R) is the displacement from equilibrium of the ion. For the description of the vibratory motions, a set of coordinates can therefore be introduced, which are are linear functions of the displacements of the particles and vary independently of one another, each as a sinusoidal function of time. Such coordinates are known as the normal coordinates of the system and the corresponding motions the normal vibrations (or modes).

In many ways, the vibratory system is completely equivalent to a collection of independent simple harmonic oscillators with respective frequencies. Three major approximations are made:

- It is assumed that displacements of atoms are small, *i.e.* $u \ll a$, where a is a lattice parameter.
- Forces acting on atoms are assumed to be harmonic, *i.e.* proportional to the displacements: $F = -Cu$. This is the same approximation which is used to describe a harmonic oscillator.
- It is assumed that the adiabatic approximation is valid – electrons follow atoms, so that the nature of bond is not affected by vibrations.

One-dimensional lattice

Consider, first, a monoatomic one-dimensional crystal lattice within the harmonic approximation (Fig. 1.7.a). One might think about the atoms in the lattice as interconnected by elastic springs. Therefore, the force exerted on n-th atom in the lattice is given by

$$F_n = C(u_{n+1} - u_n) + C(u_{n-1} - u_n) \tag{1.7}$$

where C is the interatomic force constant between nearest-neighbour planes which will differ for longitudinal and transverse waves. The equation of motion of the n-th atom is

$$M\frac{d^2u_n}{dt^2} = C(u_{n+1} + u_{n-1} - 2u_n) \tag{1.8}$$

where M is the mass of the atom. A solution of the type

$$u_n = Ae^{i(qx_n - \omega t)} \tag{1.9}$$

will lead us to the dispersion relation for the frequency $\omega(q)$

$$\omega = \sqrt{\frac{4C}{M}}\left|sin\frac{1}{2}qa\right| \tag{1.10}$$

The solutions describing the actual ion displacements are given by the real or imaginary parts of Eq. 1.9, *i.e.*

$$u_n \propto \begin{cases} cos(qn - \omega t) \\ sin(qn - \omega t) \end{cases} \tag{1.11}$$

The solutions of Eq. 1.11 describe waves propagating along the lattice chain with group velocity

$$v_g = \frac{d\omega}{dq} \tag{1.12}$$

and the phase velocity. i.e., propagation velocity of the plane wave, is defined by

$$v_p = \frac{w}{q} \tag{1.13}$$

In other words, the group velocity of a wave is the velocity with which the overall envelope shape of the wave's amplitudes (known as the modulation or envelope of the wave) propagates through space, while the phase velocity is the velocity at which the phase of any one frequency component within the envelope travels. In Fig. 1.7.c we show a schematic of a wave packet and the envelope of the wave packet[4]. The frequency ω is plotted against the wave vector q yielding the so-called dispersion curve, illustrated in Fig. 1.8.a. The significant range where q will have independent values is limited to the first Brillouin zone, *i.e.* $-\pi/a \leqslant q \leqslant +\pi/a$. At the boundaries $q_{max} = \pm\pi/a$ of the Brillouin zone the slope of the dispersion curve is zero, meaning the solution does not represent a travelling wave but a standing one. This situation is equivalent to Bragg reflection of x-rays: when the Bragg

[4]Here is a good animation illustrating this relationship well, where the red square moves with the phase velocity, and the green circles propagate with the group velocity.

condition is satisfied a travelling wave cannot propagate in a lattice, but through successive reflections back and forth, a standing wave is set up[5]. The critical value $q_{max} = \pm\pi/a$ satisfies the Bragg condition.

One-dimensional lattice with a basis

Considering now a one-dimensional lattice with two non-equivalent atoms in a unit cell (Fig. 1.7.b), while treating the atom motions in an similar way, we obtain two couple dynamical equations, *i.e.*

$$\begin{aligned} M_1 \frac{d^2 u_n}{dt^2} &= C(u_{n+1} + u_{n-1} - 2u_n) \\ M_2 \frac{d^2 u_n}{dt^2} &= C(u_{n+2} + u_n - 2u_{n+1}) \end{aligned} \tag{1.14}$$

Searching again for solutions, now for the two atoms, of the form

$$\begin{bmatrix} u_n \\ u_{n+1} \end{bmatrix} = \begin{bmatrix} A_1 e^{iqna} \\ A_2 e^{iq(n+1)a} \end{bmatrix} e^{-i\omega t} \tag{1.15}$$

we get

$$\omega^2 = C\left(\frac{1}{M_1} + \frac{1}{M_2}\right) \pm C\sqrt{\left(\frac{1}{M_1} + \frac{1}{M_2}\right)^2 - \frac{4sin^2 qa}{M_1 M_2}} \tag{1.16}$$

which yields two different solutions corresponding to two different dispersion curves, shown in Fig. 1.8.b. The lower curve is called the acoustic branch, while the upper curve is called the optical branch. The acoustic branch corresponds to $\omega = 0$ at the Brillouin ZC, *i.e.* $q = 0$. Then with increasing q the frequency increases in a linear fashion. This branch is called acoustic: it corresponds to elastic waves and

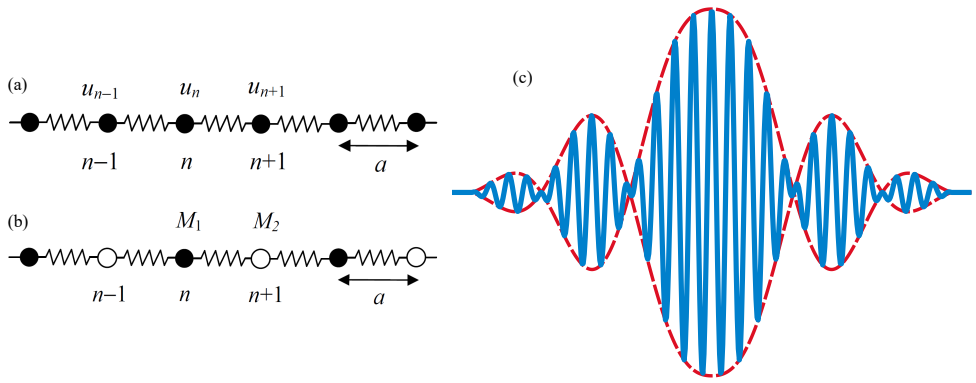

Figure 1.7: One dimension (a) monoatomic and (b) diatomic crystal lattices. The atoms are shown in their undisplaced positions, connected by a force constant C and their displacements are denoted by u_{n-1}, u_n, u_{n+1}. The lattice constant is a. (c) Schematic illustration of a wave packet (blue line) and the envelope of the wave packet (red dotted line). The envelope moves at the group velocity.

[5]The animated example of a standing wave.

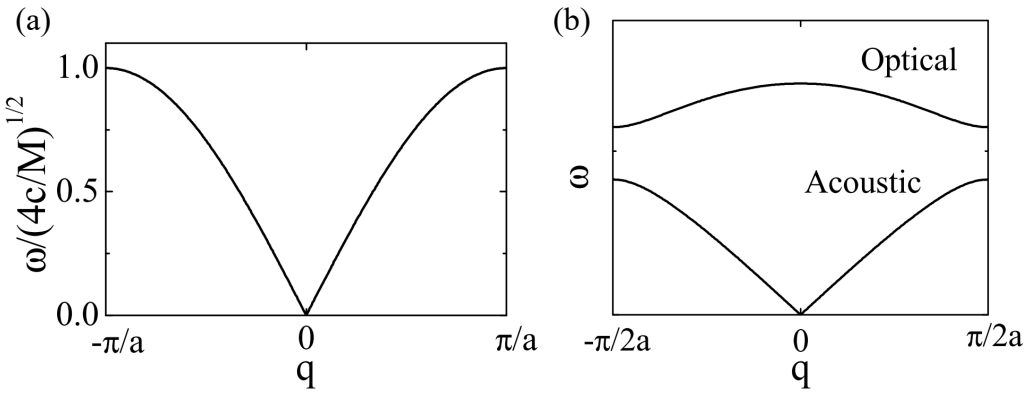

Figure 1.8: Illustration of a typical dispersion relation for a (a) monoatomic and (b) diatomic linear chains. The lower branch in (b) is the acoustic branch (same as in (a) and the upper one is the optical branch.

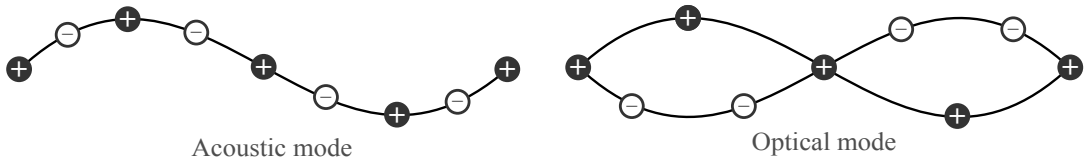

Figure 1.9: Optical and acoustic waves in a diatomic linear lattice, illustrated by the particle displacements for the two modes at the same wavelength.

sound propagation. Eventually this curve saturates at the edge of the BZ. On the other hand, the optical branch has a non-zero frequency at zero q and it does not change much with q. The distinction between the acoustic and optical branches of lattice vibrations can be seen most clearly by comparing them at $q = 0$ (*i.e.* infinite wavelength). In the acoustic mode, the two atoms in the cell have the same amplitude and the phase, therefore, the molecule oscillates as a rigid body. For optical modes, the centre of mass of the cell remains static and the two atoms move out of phase, as shown in Fig. 1.9. Their vibrational frequency is such that they can interact with infra-red radiation, hence the name optical.

Three-dimensional lattice

These considerations can be extrapolated to the three-dimensional lattice. Here is convenient to adopt a matrix notation, writing the equation of motion as

$$M\frac{d^2u_n}{dt^2}(R) = -\sum_{R'} D(R-R')u(R') \tag{1.17}$$

where $D(R-R')$ is the second derivative of the associated harmonic potential energy U, with respect to the displacement of ions at R and R' at equilibrium. Once again,

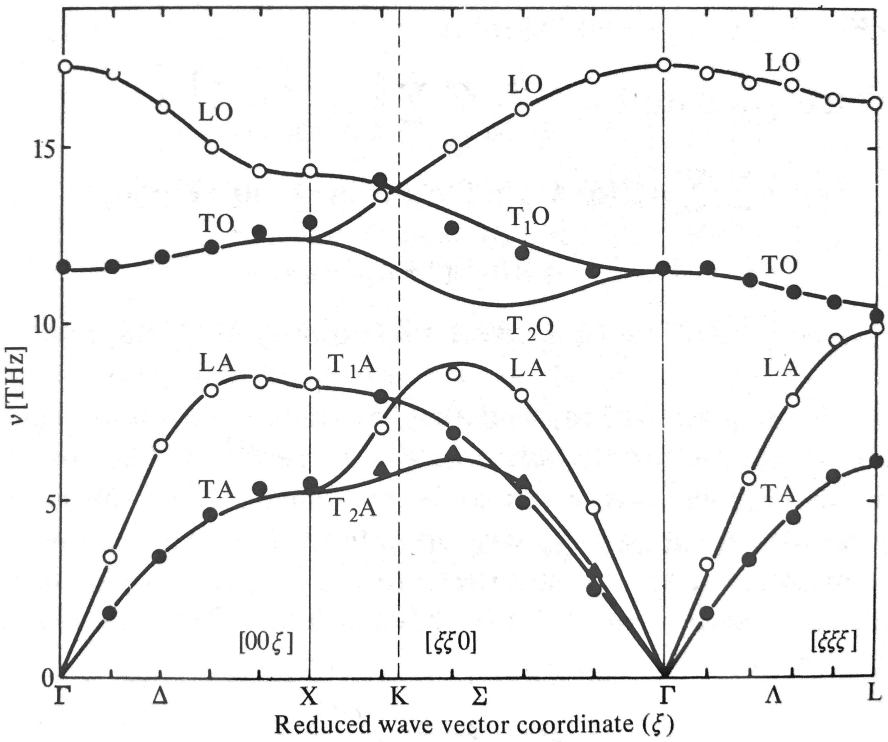

Figure 1.10: Dispersion curves for the NiO compound [2]. Note that the two transverse branches are degenerate in the [100] and [111] directions.

we are seeking solutions to the equations of motion in the form of simple plane waves

$$u(R) = \boldsymbol{\epsilon} e^{i(q \cdot R - \omega t)} \tag{1.18}$$

Here, $\boldsymbol{\epsilon}$ is the *polarization vector* of the normal mode and which describes the direction in which the ion (or wave) moves. If we substitute Eq. 1.18 into Eq. 1.17 we find a solution whenever $\boldsymbol{\epsilon}$ is an eigenvector of

$$M\omega^2 \boldsymbol{\epsilon} = D(q)\boldsymbol{\epsilon} \tag{1.19}$$

where $D(q)$ is know as the dynamical matrix and is given by

$$D(q) = \sum_R D(R) e^{iq \cdot R} \tag{1.20}$$

For each value of q there are 3N normal modes, where N is the number of ions in the unit cell, and the frequencies $\omega_s(q)(s = 1, ..., 3N)$ are all functions of q. The indexing of the branches follows from the number of degrees of freedom of the atoms. With N atoms in the primitive cell and p primitive cells, there are Np atoms. Each atom has three degrees of freedom, one for each of the x, y, z directions, making a

total of 3Np degrees of freedom for the crystal. The number of allowed q values in a single branch is just p for one Brillouin zone. Acoustic branches account for $3p$ modes and the remaining (3N – 3)p degrees of freedom are accommodated by the optical branches. The acoustic branches may be classified, by their polarizations as transverse acoustic (TA_1 and TA_2), and longitudinal acoustic (LA). The optical branches can also be classified as longitudinal or transverse when q lies along a high symmetry direction, and one speaks of LO and TO branches. A representative example of such dispersion curves is shown in Fig. 1.10.

Phonons

It is known that the energy levels of the harmonic oscillator are quantized. Similarly, the energy levels of lattice vibrations are also quantized. A quantum of vibrational energy associated with a particular normal mode is known as a phonon, which has energy $\hbar\omega$ and wave vector q. Phonons can interact with other particles such as photons, neutrons and electrons. The reason is that the center of mass of the crystal does not change its position under vibrations (except at $q = 0$).

In crystals there exist selection rules for allowed transitions between quantum states. The elastic scattering of an x-ray photon by a crystal is governed by the wavevector selection rule $\mathbf{k}_f = \mathbf{k}_i + \mathbf{G}$, where $\mathbf{G}$ is a vector in the reciprocal lattice, $\mathbf{k}_i$ is the wavevector of the incident photon and $\mathbf{k}_f$ is the wavevector of the scattered photon. This equation can be considered as condition for the conservation of the momentum of the whole system, in which the lattice acquires a momentum $-\hbar\mathbf{G}$. If the scattering of photon is inelastic and is accompanied by the excitation or absorption of a phonon the selection rule becomes

$$\mathbf{k}_f = \mathbf{k}_i \pm q + \mathbf{G} \tag{1.21}$$

where the sign (+) corresponds to creation of phonon and sign (-) corresponds to absorption of phonon. The dispersion relation is periodic in the reciprocal lattice, as $\omega(q)$ is unchanged when a reciprocal lattice vector is added to q. All possible solutions are then obtained if q is restricted to a unit cell of the reciprocal lattice, *i.e.* the first Brillouin zone.

The kinematics of the scattering of a neutron beam by a crystal lattice are described by the same general wavevector selection rule. As we will see in the next chapter (chapter 2), phonon dispersion relations $\omega(q)$ can, and are often, determined by the inelastic scattering of neutrons with emission or absorption of phonons.

1.4 Optoelectronic properties

As we said in section 1.2, with respect to PV and other optoelectronic applications, HOPs benefit from various attractive optical and electronic properties (such as optimal optical band-gap, low exciton binding energies and long charge-carrier diffusion lengths). These properties are highly dependent on their structure and chemical composition, which in this case, are highly flexible.

1.4.1 Photogeneration

Absorption

One of these advantages is the tunability of the crystal lattice and the ensuing band-gap. The organic A cation does not play a direct role in determining the band structure close to the band-gap (W_g) and acts to fulfil charge neutrality within the lattice. Nevertheless, its size is important. A larger or smaller A cation can cause the whole lattice to expand or contract, changing the B-X bond length and consequently affecting the band-gap. In Fig. 1.11, different HOPs are shown, highlighting both their versatility and their wide absorption range. An important feature of 3D HOPs is their relatively large absorption coefficient, which in part enables high photocurrents using sub-micron (*e.g.* 500 nm) films of perokvskite compounds like $MAPbI_3$ and $FAPbI_3$. The absorption coefficient of perovskites is even higher than that of GaAs, which effectively reduces the required absorber layer thickness down to 500 nm [15,18,76]. The absorption peak such materials are sharp and most have a direct band-gap [6,7,15,18,27,56]. $MAPbI_3$-based devices typically show absorption up to the tail end of the red region of the spectrum, approximately 800 nm, whereas $MAPbI_{3-x}Br_x$ yields absorption onsets at increased energies, close to 700 nm. The theoretical band-gap of $MAPbI_3$ is predicted as ∼1.7 eV by many-body perturbation theory, which is slight different from the value obtained from experimental optical band-gap value of ∼1.6 eV. A very small Urbach energy[6] of 15 meV for $MAPbI_3$ is also obtained from the particularly sharp absorption onset, which suggests that perovskite is a very pure semiconductor without deep trap states [18]. $FAPbI_3$ has reduced band-gap (1.48 eV) with absorption onsets near 850 nm. Based on the prediction of Shockley-Queisser efficiency limit model [85], 1.48 eV is closer to the "ideal" band-gap values (1.4 eV) for a single junction solar cell under AM1.5G solar

[6]Urbach energy E_U characterizes the degree of the absorption edge smearing due to the crystalline lattice disordering caused by structural peculiarities, as well as induced by external factors. The absorption coefficient at the photon energy below the optical gap (tail absorption) depends exponentially on the photon energy: $\alpha(\hbar\omega) \sim exp(^{\hbar\omega}/_{E_u})$.

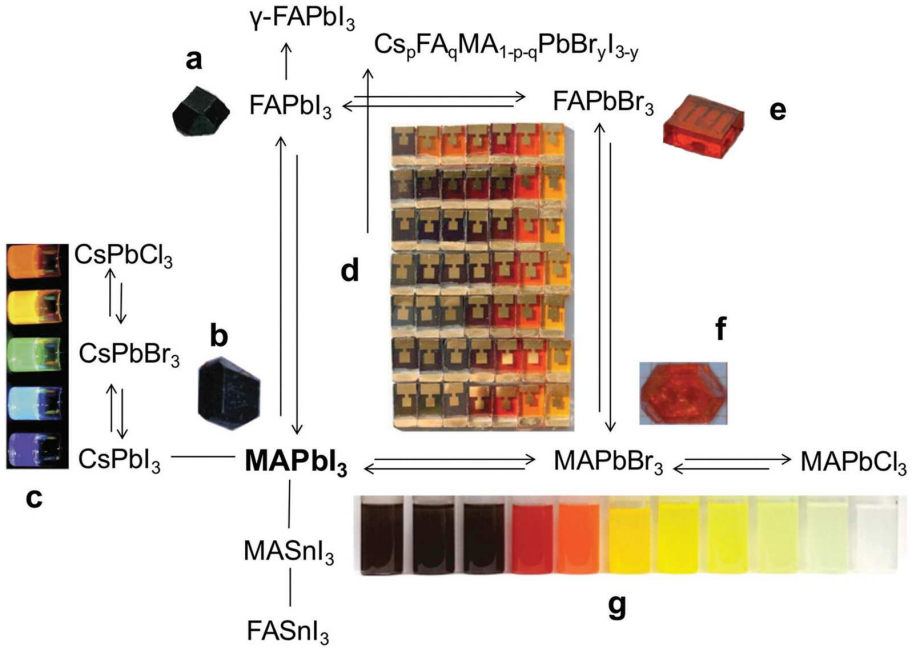

Figure 1.11: Schematics of some perovskites highlighting their absorption tunability. The insets show: (a) single crystal of $FAPbI_3$ [3]; (b) single crystal of $MAPbI_3$ [4]; (c) colloidal solutions of $CsPbX_3$ (X = Cl, Br, I) perovskites [5]; (d) solar cells of 49 different compositions in the MA/FA-Pb-Br/I compositional space [6]; (e) single crystal of $FAPbBr_3$ [3]; (f) single crystal of $MAPbBr_3$ [4], and (g) colloidal nanocrystals of $MAPbX_3$ (X = Cl, Br, I) perovskites [7]. Reprinted from [1].

illumination. Incorporation of Br in $FAPbI_{3-x}Br_x$, can be used to tune the band-gap, increasing up to 2.23 eV for x = 3 (*i.e.* 100% Br content) corresponding to an absorption onset of approximately 550 nm. This illustrates the high level of tunability of the band-gap in HOPs.

Excitons vs. free carriers

In Fig. 1.12.a,b the basic working principle of photogeneration in an perovskite based solar cell is illustrated. Let us first consider the interaction of irradiation with a semiconductor. For photon energy $h\nu < W_g$, the photon can be absorbed by lattice or free carriers only, and absorption coefficient is low for wavelengths longer than hc/W_g. If the photon energy $h\nu > W_g$, the band-to-band (interband) absorption takes place and the absorption coefficient α increases rapidly with photon energy. The difference in energy $(h\nu - W_g)$ is dissipated in the form of heat as the excited electron relaxes to the bottom of the conduction band (CB) by losing energy to lattice collisions (thermodynamic loss). In some materials (*e.g.* organic semiconductors), after photon absorption an exciton can be generated, that is, an excited electron/hole pair that is still in a bound state due to the Coulomb forces between the particles. An exciton can slowly diffuse in material and it can dissociate in an electron–hole pair after obtaining an additional energy higher than its

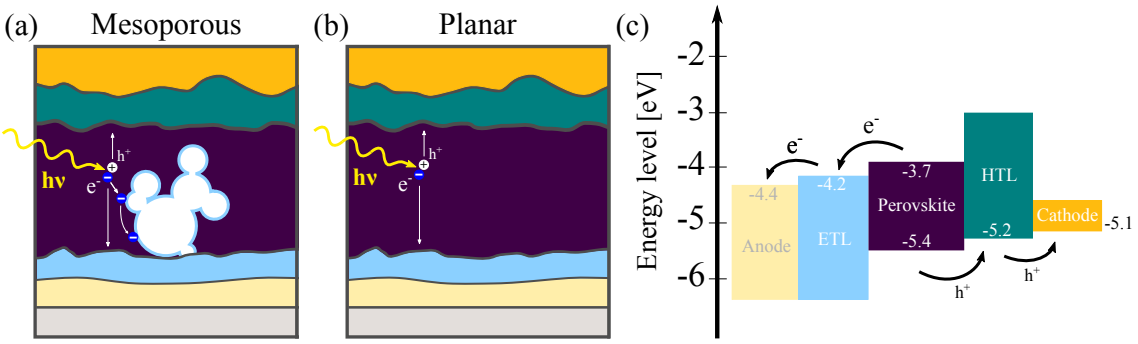

Figure 1.12: Schematic representation of the charge generation and extraction processes in a (a) mesoporous and (b) planar perovskite solar cell. Light is absorbed in the bulk of the film leading to generation of free charges, which diffuse throughout the film to the electron transporting layer (ETL) and hole transporting layer (HTL) and are then selectively collected by the respective electrodes. (c) Illustration of a typical energy level relationship between materials used in PSCs.

binding energy, or recombine radiatively before carrier collection. Here, dielectric constant ε is key in determining exciton binding energy. Depending on whether the low ($\varepsilon = 25.7$) or high ($\varepsilon = 5.6$) frequency dielectric constant is used [86, 87], the conventional Wannier–Mott hydrogenic model gives values for the excitonic binding energy ($R^\star = m^\star e^4 \ / \ 2\hbar^2\varepsilon^2$, $m^\star$ is effective mass) anywhere from 2 to 50 meV. After an initial period of debate, Even *et al.* [88], based on the theoretical analysis of previously measured absorption spectra in $MAPbI_3$, predicted $R^\star$ to be 15 meV at low temperature. This was soon confirmed by a direct experimental measurement also in $MAPbI_3$ [89], which reports a value of 16 $\pm$ 2 meV, contradicting in this way the earlier values of 37-50 meV [90, 91], and suggesting therefore, a dielectric constant of $\varepsilon \approx 9$. From such theoretical work, together with the aforementioned report of Miyata *et al.* [89] and another experimental study of temperature-dependent photoelectronic responses, it was concluded that the exciton-binding energy decreases continuously to 5-6 meV at RT. This is much lower than thermal energy kT at RT (∼25 meV), confirming that HOPs are predominantly non-excitonic at this temperature range. Such spontaneous generation of free electrons and holes following photoabsorption helps minimize the losses due to exciton migration and exciton recombination.

As previously stressed, organic-inorganic perovskites provide ambipolar transport. Also, as will be further discussed below (section 1.4.2), they show both electron and hole diffusion lengths exceeding 1 μm [92] and sufficiently high mobilities of electrons and holes [3, 74]. These properties guarantee efficient carrier collection for micrometer thick layers. Together with the non-excitonic nature, this is what enables the high internal quantum efficiencies seen in PSCs. However, it is crucial to select the electron transporting layer (ETL) and hole transporting layer (HTL) with

favourable energy level alignment to the CB and valence band (VB), respectively, in order to extract carriers from perovskite solar cells without loss (Fig. 1.12.c). The open-circuit voltage (V_{OC}) of a perovskite solar cell is mainly determined by two effects, the radiative recombination of the perovskite and the energetics of the transporting interface layers.

Recombination

Recombination is the process during which two charge carriers of opposite type annihilate each other. Energy is released in the form of photons (radiative recombination) or heat (non-radiative recombination) during this process. Since in perovskites photoexcitation results mainly in free charges at RT, the overall recombination rate is the results of three different processes. There are schematically shown in Fig. 1.13 and consist in band-to-band, trap-assisted and Auger recombination. In band-to-band recombination, an electron in the conduction band directly recombines with a hole in the valance band (Fig. 1.13.a). Band-to-band recombination is typically radiative, *i.e.* the energy difference is released in the form of a photon. Trap-assisted recombination, *i.e.* Schockley-Read-Hall (SRH) recombination, is a two-step process where a trap state captures an electron and a hole which recombine (Fig. 1.13.b). Trapped carriers can recombine both radiatively and/or through phonon-assisted nonradiative processes, although the latter is most commonly considered. Auger is a non-radiative recombination process involving three bodies (carriers). In this case, the energy released from recombination is transferred to another carrier, which is excited into a higher state and then relaxes to the bottom of conduction band through thermalization (Fig. 1.13.c). However in nowadays growth of halide perovskite thin films, such detrimental phenomena only result from shallow traps.

In general, the recombination processes can be considered to occur independently and the resulting recombination rate is simply the sum of the individual rates. From that it follows that the resulting carrier lifetime, τ, defines the time window in which the charges can be extracted to the contacts before they recombine, can be given by Matthiessen's rule

$$\frac{1}{\tau} = \frac{1}{\tau_B} + \frac{1}{\tau_T} + \frac{1}{\tau_A} \tag{1.22}$$

where τ_B, τ_T and τ_A are the lifetimes associated with the band-to-band, trap-assisted and Auger recombination processes, respectively.

The external radiative efficiency (ERE) of a PV cell - which is the fraction of total dark recombination current that results in the emission of light - is a good indicator of how close to perfection the cell is [93]. At present, the best perovskite

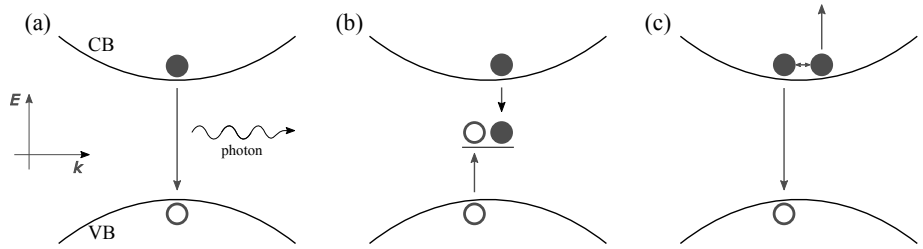

Figure 1.13: Schematic diagram of the (a) band-to-band, (b) trap-assisted and (c) Auger recombination mechanisms.

solar cells have an ERE of 1–4%, while for isolated perovskite films ERE is as high as 70% [94]. This indicates that when the perovskite active layer is integrated in a solar cell device, recombination losses are introduced. In a real device, bulk defects, surfaces, and interfaces introduce recombination centers that lead to fast nonradiative losses. This is reflected in the V_{OC}, currently approaching the radiative limit, but there remains more than 100 mV to be gained, by minimizing these losses. Efforts should be made in molecular passivation of the perovskite surface and improvement of interfacial engineering. The latter implies more refined energetic alignment and good lattice matching and/or continuous interfaces at the atomic level between perovskite and carrier collectors.

1.4.2 Charge-carrier and thermal conductivity

Free charge-carrier transport in semiconductors involves two mechanisms: diffusion and drift [95]. Carrier diffusion transport mechanism, occurs in any semiconductor with the carriers moving from high carrier density regions to low carrier density regions, even when no electric field is present due to thermal energy, k_bT. The diffusion length of a charge is simply the average distance that charge is able to travel because of diffusion before recombination occurs. Carrier drift transport mechanism relates to the carrier motion caused by an external electric field, with the characterized parameter of mobility (μ). The field-free diffusion coefficient D and the charge-carrier mobility μ can be correlated with each other via the Einstein relation [96]:

$$\mu = \frac{e}{k_bT}D \tag{1.23}$$

where e is the electronic charge. Diffusion length, L_D, can be calculated from the diffusion coefficient and charge carrier lifetime, τ, using

$$L_D = \sqrt{D\tau} \tag{1.24}$$

L_D is a critical parameter for solar cell operation because it directly influences the efficiency of charge collection in a solar cell film. At present, it is commonly accepted that the extremely efficient charge collection in lead-based perovskite solar cells strongly relies on the long charge-carrier diffusion lengths (in the micrometer range) that normally result from the sufficient long carrier lifetimes in perovskites [92, 97–100]. Carrier diffusion lengths up to 100 nm for both electrons and holes in $MAPbI_3$ and exceeding 1 μm in the mixed halide $MAPbI_{3-x}Cl_x$ have been reported via transient photo-luminescence (PL) measurements [92, 97]. However, it has been demonstrated that holes are much more efficiently extracted than electrons in $MAPbI_3$ [101], thus explaining the necessity of a mesoporous ETM for $MAPbI_3$-based devices, whereas in $MAPbI_{3-x}Cl_x$, both electrons and holes have diffusion lengths exceeding 1 μm and do not require a mesoporous ETM. Even more recently, Dong *et al.* have demonstrated diffusion lengths over 175 μm in single crystals of $MAPbI_3$ under 1 sun illumination, owed to enhanced carrier mobility, lifetime and reduced number of defects [98]. Moreover, FA-based devices have shown diffusion lengths intermediate to those of $MAPbI_3$ and $MAPbI_{3-x}Cl_x$.

On the other hand, the charge-carrier mobility in perovskites are not on par with other PV relevant inorganic semiconductors. While the mobility of $MAPbI_3$ is high, as it relates to other solution-processed materials, such as organic semiconductors [102, 103], it has a relatively modest mobility compared to other PV-relevant inorganic semiconductors which display similar effective masses. In fact, the mobility of other PV relevant semiconductors is typically 1 to 2 orders of magnitude higher than has been observed in the two most widely used PSC materials, $MAPbX_3$ and $FAPbX_3$ [104]. Moreover, even though one of the remarkable aspects of HOPs is their ability to form high-quality semiconductor films from solution, morphological effects hinder transport in these films. Not only that but, even within single crystal samples of identical composition, a wide range of reported mobility values have been reported. Such wide differences imply the strong influence of both the material morphology and the applied measurement technique, on charge carrier mobility. Regardless, reported values are mostly between 1-100 $cm^2V^{-1}s^{-1}$, with some as high as 600 $cm^2V^{-1}s^{-1}$ [8, 70, 74, 75, 97, 98, 105–117]. Table 1.1 summarizes the charge carrier mobility values experimentally determined by various methods for our four relevant perovskites at RT.

It is known that scattering and recombination processes present the main hindrances to charge mobility. In the absence of extrinsic scattering by impurities or interfaces, phonon scattering sets the fundamental intrinsic limit to charge-carrier mobility. Therefore, in the rather defect tolerant HOPs, electron-phonon interac-

Table 1.1: Experimentally determined charge-carrier-mobility values at RT for various HOPs.

Compound	Architecture	Carrier type	Mobility $cm^2V^{-1}s^{-1}$	Technique	Ref.
$MAPbI_3$	Thin film	Electron (hole)	1.4 (0.9)	PLQ	[97]
	Thin film	Electron/hole)	2–3	TAM	[108]
	Thin film	Electron + hole	35	TRTS	[8]
	Thin film	Electron + hole	20	TRTS	[112]
	Thin film	Electron + hole	11	TRTS	[111]
	Thin film	Electron + hole	30	TRMC	[113]
	Thin film	Electron + hole	71	TRMC	[117]
	Mesoporous matrix	Electron (hole)	8	TRTS	[105]
	Mesoporous matrix	Electron (hole)	9	TRMC	[113]
	Polycrystal	Electron	66	Hall	[70]
	Single crystal	Hole	105	Hall	[109]
	Single crystal	Electron + hole	600	TRTS	[109]
	Single crystal	Electron + hole	130	TRMC	[116]
	Single crystal	Hole	67	SCLC	[114]
	Single crystal	Hole	2.5	SCLC	[107]
	Single crystal	Hole	24	TOF	[98]
$MAPbBr_3$	Thin film	Electron (hole)	8.6 (9.0)	PLQ	[115]
	Single crystal	Hole	24	SCLC	[114]
	Single crystal	Hole	38	SCLC	[107]
	Single crystal	Hole	40	Hall	[107]
	Single crystal	Hole	115	TOF	[107]
$FAPbI_3$	Thin film	Electron (hole)	0.2 (3.5)	PLQ	[106]
	Thin film	Electron + hole	27	TRTS	[110]
	Single crystal	Hole	35	SCLC	[74]
	Single crystal		4.4	SCLC	[75]
$FAPbBr_3$	Thin film	Electron + hole	14	TRTS	[110]
	Single crystal	Hole	62	SCLC	[74]

tionss (EPIs) play the primary role. However, despite the importance of EPIs to the optoelectronic properties of these materials, there is still no consensus on which exact mechanisms are active. A number of studies [8, 118, 119] have observed an acoustic-like temperature dependence of the mobility, *i.e.* $\mu \propto T^{-3/2}$ (see Fig 1.14). On the other hand, it has been shown that carrier scattering is dominated by Fröhlich coupling[7] between charge-carriers and LO phonon modes, rather than with acoustic ones, at RT [120, 121]. The interaction with acoustic phonons is indeed expected to be limited to deformation potentials thanks to the absence of piezoelectricity.

[7]In polar semiconductor materials, LO phonons produce a macroscopic electric field, which interacts with the electrons. This coupling of long range is known as Fröhlich interaction. Due to the interaction of an electron with LO phonons, a quasi-particle is formed known as polaron. The strength of this coupling is expressed by a dimensionless Fröhlich coupling constant.

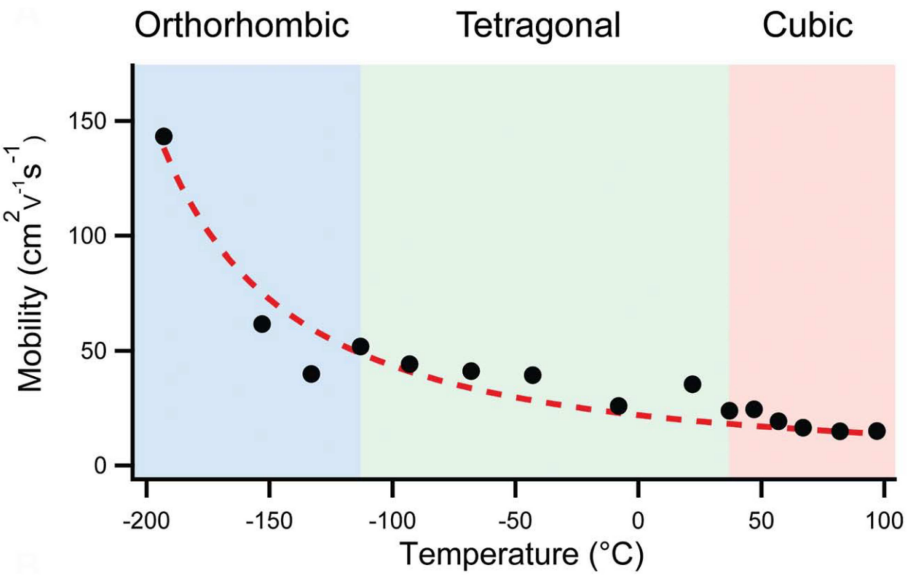

Figure 1.14: Mobility in $MAPbI_3$ as a function of temperature, determined from optical-pump–THz probe measurements. The black dots represent data, and the dashed line is the theoretical $T^{-3/2}$ dependence predicted for band-like transport. Reprinted from [8].

Furthermore, slow charge-carrier cooling following above band-gap photon absorption, is also governed by the interactions between charges and phonons [9, 99]. This effect is enhanced by the low thermal conductivities that HOPs are known for, a result of slow propagation speed of acoustic phonons due to anharmonic phonon–phonon scatterings.

Crystal-liquid duality

The coexistence of a crystalline-like response in coherent band transport of charge carriers and a liquid-like response in phonon dynamics has prompted Zhu *et al.* [122] to call HOPs "crystalline liquids" for the cubic and tetragonal phases. We can view the sub-lattice of organic cations as a confined liquid, with each polar molecular cation confined in a nanoscopic pore; thus, an HOP in the high-temperature cubic phase is similar to a plastic crystal [121], which refers to a crystalline lattice with long-range translational order but local rotational disorder [123]. More precisely, the liquid-like behavior may generally represent the highly disordered and anharmonic motions of the strongly coupled vibrational modes of both PbX_3^- and A^+ sublattices [124]. The contrasting phonon and electron dynamics mean that HOPs belong to the family of solids called phonon glass electron crystals (PGEC).

Phonon glass electron crystal refers to composite materials or multilayers where the materials/components that contribute electrical conductivity are different from the materials/components that are poor thermal conductors. The former metallic

regions are prevented from causing a large thermal conductivity by keeping them small. Skutterudites and clathrates, for example, are two types of crystal structures that have "cages" that can host various guest atoms. The rattling in the nanocages introduces efficient scattering for the phonons, particularly acoustic phonons that are mainly responsible for thermal transport, diminishing then thermal conductivity. Halide organolead perovskites crystals belong to the PGEC material family. Here, the PbX_3^- sublattice forms the crystalline framework, whereas the A^+ cations "rattle" and/or "rotate" in the cuboctahedral cages.

In the upcoming chapters 3 and 4, we explore the correlation between low elastic stiffness, low thermal conductivity and the so called *hot-phonon bottleneck* effect in carrier thermalization.

Chapter 2

Neutron Scattering and experimental methods

Neutron scattering is a well establish technique and, naturally, its theory has already been extensively covered in detail in textbooks [125, 126]. Therefore, the following sections will focus on the main concepts and results that will be used within the thesis. We also summarize all the synthesis of the perovskite single crystal samples as well as the experimental conditions of the characterization techniques used (neutron, Brillouin and Raman spectroscopy).

2.1 Introduction

Neutron scattering is one of the most powerful and versatile experimental methods to study the structure and dynamics of materials on the atomic and nanometer scale. Quoting the Nobel committee, when awarding the prize to C. Shull and B. Brockhouse in 1994 for their extensive contributions in the field of neutron scattering, these pioneers have "helped answer the question of where atoms are and (...) what atoms do" [127]. As of today it is firmly established as an invaluable complement to x-ray scattering for the characterization in many areas of materials science, chemistry and biology.

Although neutron scattering is a great technique, historically, its main limitations in experimental practice is that neutrons are produced at low fluxes and high costs. Neutron scattering experiments last from hours to days and are performed only at a few handfuls of large international facilities. This makes the technique time-consuming and rare. Hence, neutron scattering should be used only where more accessible methods are inadequate. As an alternative, X-rays scattering is usually the go to option: x-ray sources are by far more abundant and are, especially for synchrotron x-ray sources, much stronger than neutron sources (*i.e.* fluxes of 10^{18} photon per $s^{-1}mm^{-2}$ versus 10^4 neutron per $s^{-1}mm^{-2}$). However, as we will see, neutrons have a number of properties that make them extremely useful for purposes where X-rays are not sufficient. The most relevant such properties are presented in Table 2.1 [128].

As all other matter, neutrons have both particle- and wave-like nature and can be described via the "de Broglie" relationship

$$\lambda = \frac{h}{p} = \frac{h}{mv} \tag{2.1}$$

where h is the Planck constant and λ, p, m and v are the neutron wavelength, momentum, mass and velocity respectively. The energy E of a neutron with a wave

Table 2.1: Properties of the neutron.

Quantity	Value
Rest mass, m_n	1.675 x 10^{-24} g
Charge	0
Magnetic moment, μ_n	1.913 nuclear magnetons, μ_N
Spin	1/2

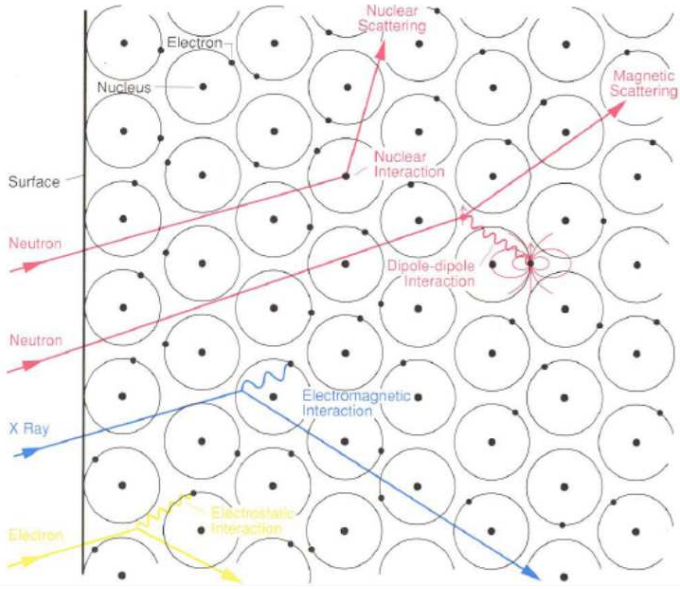

Figure 2.1: Different scattering interaction of neutrons, x-rays and electrons with matter.

vector k written through the Planck-Einstein relation is

$$\lambda = \frac{h^2 p^2}{2m} \tag{2.2}$$

Alternatively, equation 2.2 can be rewritten in terms of neutron wavelength

$$\lambda = \left(\frac{h^2}{2mE} \right)^{1/2} \tag{2.3}$$

If one consider the mass of the neutron, m = 1.675 x 10^{-24} g, it is easy to see that a neutron with an energy E = 25 meV has a wavelength λ = 1.81 Å, which is compatible with inter-atomic spacings of crystal structures and their vibrations. Neutron energies depend obviously on the neutron beam/source but, in scattering experiments, are typically in the range of a few meV. It is their neutrality, however, that makes neutrons uniquely useful in probing, from the standpoint of scattering interactions. The zero net charge of the neutron means that it interacts very weakly with matter and it also easily transmits through sample enclosures used to control the environment. This is a very important experimental convenience. Even more important is the fact that with zero charge there is no Coulomb barrier to overcome, so that the neutrons are oblivious to the electronic charge cloud and interact directly with the nuclei of atoms.

Fig. 2.1 illustrates the different scattering interactions of incident x-rays, electrons and neutrons with matter. X-rays and electrons interact with electrons in the material: with x-rays the interaction is electromagnetic while with an electron beam

it is electrostatic. Both of this interactions are strong and neither type of beam penetrates matter very deeply. Neutrons on the other hand, interact with atoms via nuclear forces, which are very short range – on the order of a few femtometers. Therefore, as far as the neutron is concerned, solid matter is not very dense since the size of a scattering center (*i.e.* a nucleus) is typically 10^5 times smaller than the distance between centers. Thus, neutrons generally penetrate different materials much deeper than x-rays or electrons. If there are unpaired electrons in the system, neutrons may also interact via a second mechanism: a dipole-dipole interaction between the magnetic moments of the neutron and the unpaired electron. Knowing now that x-rays are scattered by electrons we can see how with the former it is easier to see elements that have higher atomic number. Hydrogen, for example, which has only one electron is hardly detectable with x-rays. With neutrons, however, since they are scattered by nuclei, nearly all elements are visible. In scattering, this effective area presented by the nucleus to an incident neutron is defined as the scattering cross section[1]. If the neutron hits this area it will be scattered with equal probability in any direction. Fig. 2.2 illustrates the comparison of varying cross section of some materials for x-rays and neutrons. As compared with x-ray scattering cross sections, which is directly proportional with the atomic number Z^2, neutron scattering cross sections show little systematic relationship with Z^2. Neutron scattering gives us then the possibility to probe different element isotopes, however, on the other hand, this can bring some experimental hurdles such as unwanted incoherent signal background, especially when dealing with organic samples.

Although the neutron carries no net charge, its internal structure an up quark and two down quarks gives the neutron a magnetic moment. In fact the scattered intensity associated with magnetic effects is comparable to the scattering from the nuclei. With a spin angular momentum of $\pm 1/2$ per neutron, neutron beams can be prepared which contain a single angular momentum state, either spin up (+1/2) or spin down (-1/2). These spin-polarized neutrons have unique applications in determining magnetic structures, separating magnetic from nuclear scattering, and isolating incoherent scattering from the total scattering. This makes neutron scattering the only technique that allows direct observation of magnetic excitations in materials.

A summary of the advantages of neutron scattering are as follows:

- **Energy and wavelength.** Thermal neutrons have a wavelength (around 1.8 Å) similar to inter-atomic distances, and an energy (around 25 meV) similar to elementary excitations in solids. One can thus obtain simultaneous information

[1] More on neutron cross section in section 2.2.2

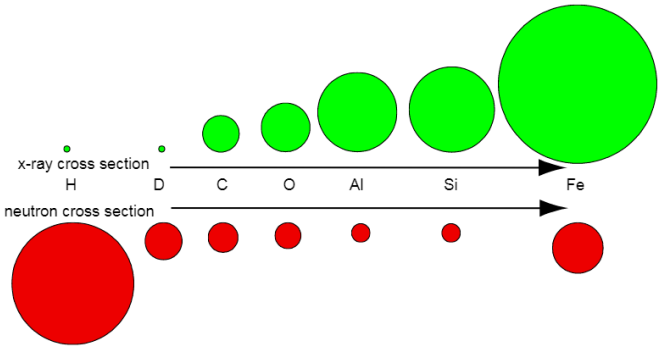

Figure 2.2: Schematic comparison between neutron and x-ray cross sections.

on the structure and dynamics of materials and *e.g* measure dispersion relations (energy-wavelength dependence) of excitations in crystalline solids.

- **Isotopes and light elements.** The neutron scattering cross section varies in a seemingly random fashion between elements and even between different isotopes of the same element. One can thus use neutrons to study light isotopes. In particular, this is important for hydrogen, which is almost invisible to x-rays. With neutrons, the large difference in scattering between usual hydrogen (H) and deuterium (D) can be used in biological and soft matter sciences to change the contrast in the scattering or even to "highlight" selected groups within large molecules or aggregates.
- **Quantitative experiments.** The interaction between neutrons and (most) matter is rather weak, implying that neutrons can probe the bulk of the sample, and not only its surface. The weak interaction also diminishes higher order effects. Hence, quantitative comparisons between neutron scattering data and theoretical models can be performed to a high precision.
- **Transparency.** Since neutrons penetrate matter easily, neutron scattering can be performed with samples stored in all sorts of sample environment: Cryostats, magnets, furnaces, pressure cells, etc. Furthermore, very bulky samples can be studied, up to tens of cm thickness, depending on their elemental composition. The sample is left relatively unharmed by the neutron experiment, although beam experiments should certainly not be performed on living organisms.
- **Magnetism.** The neutron magnetic moment makes neutrons scatter from magnetic structures or magnetic field gradients. Unpolarized neutrons are used to learn about the periodicity and magnitude of the magnetic order, while scattering of spin-polarized neutrons can reveal the direction of the atomic magnetic moments. Also, the dynamics of the magnetic moments can be revealed.

2.2 Neutron scattering theory

2.2.1 Scattering diagram

As mentioned, neutrons have dual properties and behave as matter waves through the de Broglie relationship. In neutron scattering experiments, we work in terms of neutron plane wave propagation, described by the advancement of a wave front. Perpendicular to this wave front, the neutron wavevector $\mathbf{k}$ has a vector of magnitude $2\pi/\lambda$ that defines the propagation direction. In the diffraction of a wave, an incoming neutron with an initial wavevector $\mathbf{k}_i$ will be scattered by the sample into a state with a final wavevector $\mathbf{k}_f$. The difference in direction between the incoming and the scattered neutron is defined by the angle 2θ. This leads us to the well known conservation laws of momentum and energy

$$\mathbf{Q} = \mathbf{k}_i - \mathbf{k}_f \ (momentum\ conservation) \tag{2.4}$$

$$\hbar\omega = \mathrm{E}_i - \mathrm{E}_f \ (energy\ conservation) \tag{2.5}$$

where E_i and E_f are the initial and final energies of the neutron and $\hbar\omega$ the energy transferred to the sample. The three vectors $\mathbf{k}_i$, $\mathbf{k}_f$ *and* $\mathbf{Q}$ form the scattering triangle, as shown in Fig. 2.3. It is important to note the sign convention used for the scattering vector $\mathbf{Q}$, since it will have implications in the resolution function (section 2.2.4). Applying some trigonometry to the scattering triangle, one obtains

$$|\mathbf{Q}| = \mathbf{k}_i^2 + \mathbf{k}_f^2 - 2\mathbf{k}_i\mathbf{k}_f\cos\theta \tag{2.6}$$

and the energy conservation law can be written as

$$\hbar\omega = \frac{\hbar^2}{2m_n}(\mathbf{k}_i^2 - \mathbf{k}_f^2) \tag{2.7}$$

We can then see that, in a scattering experiment, knowing the neutron scattering angle and the wavelength of the incident/final beam, one can easily deduce the momentum and energy transferred to the sample via equations 2.4 and 2.7. Now, in the event that energy is transferred between the neutron and the sample matter, *i.e.* the neutron loses or gains energy during the process, then we are in the inelastic scattering condition (Fig. 2.3.b). On the other hand, in elastic scattering the kinetic energy of the neutron is conserved (Fig. 2.3.a). One can then obtain information about the equilibrium structure (elastic scattering) and the collective motions of the atoms (inelastic scattering), such as those that produce phonons or vibrational

waves in a crystalline lattice.

Elastic scattering

Supposing the scattering is elastic then $|\mathbf{k}_i| = |\mathbf{k}_f| = |\mathbf{k}| = \mathrm{k}$. In Fig. 2.3.c a reciprocal lattice is represented, where each point corresponds to a reciprocal lattice point. From a vector $\mathbf{k}_i$ originating in some point A, a sphere with centre A and radius $|\mathbf{k}_i| = |\mathbf{k}_f| = \mathrm{k}$ can be extrapolated. In other words, since $\mathbf{k}_i$ and $\mathbf{k}_f$ have the same length, the scattering vector must lie on the surface of a sphere of radius $2\pi/\lambda$. This sphere is called the Ewald sphere. For certain configurations of the sample orientation and/or the incident beam $\mathbf{k}_i$, the sphere will be such that it passes through two points, one of which is the origin of the reciprocal space. The reciprocal lattice points are the values of momentum transfer where the Bragg diffraction condition is then satisfied. We find that

$$\mathbf{Q} = \mathbf{G} = \mathbf{k}_i - \mathbf{k}_f \tag{2.8}$$

or

$$|\mathbf{Q}| = |\mathbf{G}| = 2|\mathbf{k}|sin\theta = \frac{4\pi sin\theta}{\lambda} \tag{2.9}$$

To show that 2.9 corresponds to the Bragg Law we note that each reciprocal vector G is perpendicular to a set of planes in the original lattice and has a magnitude that is an integral multiple of 2π times the inverse of the the plane spacing, $d = 2\pi/|\mathbf{G}|$. Thus, using the relationship between $\mathbf{Q}$, θ and λ obtained from Fig. 2.3 the condition

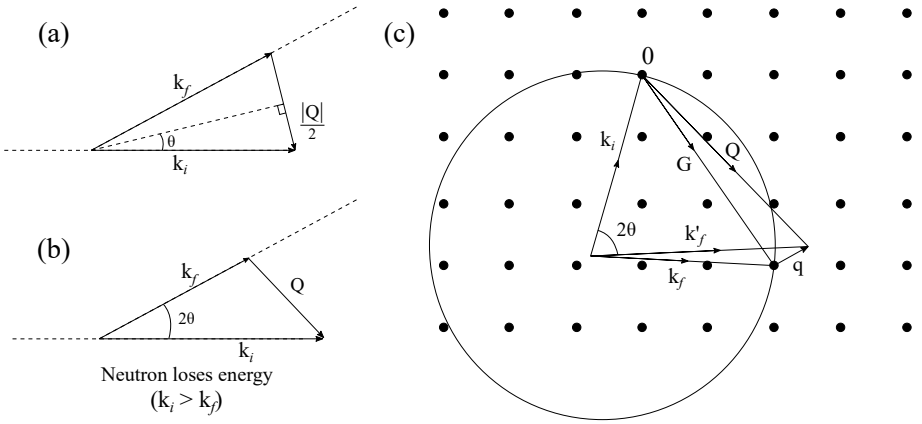

Figure 2.3: Scattering triangles are depicted here for both (a) elastic scattering in which the neutron is deflected but does not gain or lose energy ($|\mathbf{k}_i| = |\mathbf{k}_f|$) and (b) inelastic scattering in which the neutron exchanges energy with the scattering sample ($|\mathbf{k}_i| \neq |\mathbf{k}_f|$). (c) Two-dimensional representation of reciprocal space showing the Ewald circle and the vector representation for elastic and inelastic scattering. Here G is a reciprocal-lattice vector and q the momentum transfer within the first Brillouin zone.

above is easily rewritten as

$$n\lambda = 2d\sin\theta \tag{2.10}$$

which is the more familiar form of the Bragg's Law.

We now see how the magnitude of $\mathbf{Q}$ is simply controlled by adjusting the angle 2θ between $\mathbf{k}_i$ and $\mathbf{k}_f$. Hence, as mentioned, Bragg scattering may occur for any set of planes in a crystal, provided the neutron wavelength λ and the angle 2θ satisfy Eq. 2.10. In practical terms, any point in reciprocal space can be measured by an appropriate choice of $\mathbf{k}_i$, 2θ and the orientation of the sample relative to $\mathbf{k}_i$.

Inelastic scattering

Atoms are not actually frozen in fixed positions inside a crystal structure, as is assumed in the description of elastic scattering.. Thermal energy causes them to oscillate about their lattice sites, thereby reducing the elastic contribution. As a result, there is a transfer of energy and momentum between the incident neutron and the sample, and a change of both the direction and magnitude of the neutron wavevector. In other words, $|\mathbf{k}_i| \neq |\mathbf{k}_f|$ is observed for inelastic neutron scattering (INS).

Atomic and molecular motions in a crystal lattice behave in a wave-like manner, leading to a superposition of waves with different frequencies and wavelengths and which propagate in different directions. The quantum quasiparticles related to lattices waves are known as phonons. Each phonon has an energy $h\nu$, where ν is the frequency of the motion which depends on the wavelength of the distortion, the masses of the atoms and the binding forces that connect them. Basically then, the variation of energy that is being measured in inelastic scattering corresponds to the phonon energy. To represent the dispersion of phonon energies in the first Brillouin zone, the relative momentum transfer $\hbar\mathbf{q}$ to Eq. 2.9 is defined

$$\mathbf{Q} = \mathbf{G} + \mathbf{q} \tag{2.11}$$

as also illustrated in Fig. 2.3. Experimentally, to determine the phonon energy, a sequence of measurements is made where one can either hold constant the momentum transfer or the energy transfer. The resulting peak obtained from the constant-$\mathbf{Q}$ and/or constant-$\mathbf{E}$ scans yields the amplitude of the phonon[2].

[2]For more on phonon measurement please refer to section 2.2.3.

2.2.2 Neutron cross section

The neutron fluence rate (Φ), or flux of a neutron beam, is the number of neutrons that pass through a specified area per unit time.

$$\Phi = \frac{\text{number of incident neutrons on a surface per second}}{\text{surface area perpendicular to the neutron beam direction}} \tag{2.12}$$

Commonly employed units for this quantity are $mm^{-2}s^{-1}$ or $cm^{-2}s^{-1}$, being the direction here irrelevant. The neutron scattering cross section, σ, of a system is defined by its ability to scatter neutrons

$$\sigma = \frac{1}{\Phi} \cdot \text{number of neutrons scattered per second} \tag{2.13}$$

which as units of area. For a single nucleus, σ can now be seen as the effective area of the nucleus perpendicular to the neutron beam. The scattering cross section used here is the total cross section, which depends on the sample volume, V. For thin samples, σ can be described by the volume specific cross section, Σ, through

$$\sigma = V\Sigma \tag{2.14}$$

For thicker samples, beam attenuation must be taken into account.

The angular dependence of the scattered neutrons is a most important aspect of all neutron scattering. This dependence is described by the differential cross-section

$$\frac{\mathrm{d}\sigma}{\mathrm{d}\Omega} = \frac{\begin{pmatrix}\text{number of neutrons scattered per second into} \\ \text{the solid angle } \mathrm{d}\Omega \text{ in the direction } \theta, \phi\end{pmatrix}}{\Phi \mathrm{d}\Omega} \tag{2.15}$$

where $\mathrm{d}\Omega$ is the unit of solid angle and (θ, ϕ) are polar coordinates defining the direction of the scattered beam. The geometry of the event is illustrated in Fig. 2.4. The total number of scattered neutrons is then the integral of neutrons per solid angle over all of the 4π solid angle

$$\sigma = \int \frac{\mathrm{d}\sigma}{\mathrm{d}\Omega} \mathrm{d}\Omega \tag{2.16}$$

However, for describing inelastic scattering, one needs to take into account the energy dependence of the scattered neutrons. This is described by the partial differential cross-section, which is the basic quantity measured during a neutron scattering experiment and one that represents the fraction of neutron of incident energy E_i scattered into an element of solid angle $\mathrm{d}\Omega$ with a final energy between E_f and E_f

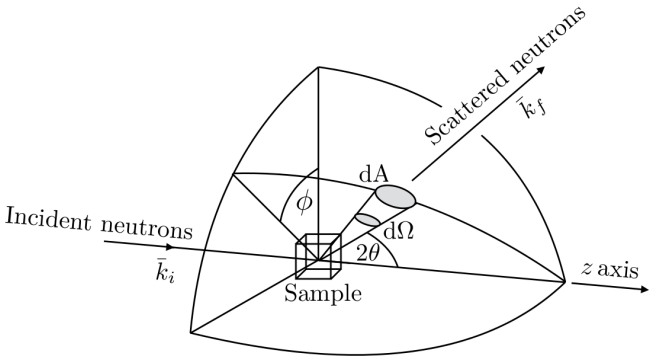

Figure 2.4: An illustration of the scattering geometry.

$+ \mathrm{dE}_f$. The partial differential cross-section is then defined as

$$\frac{\mathrm{d}^2\sigma}{\mathrm{d}\Omega\mathrm{dE}_f} = \frac{\left(\begin{array}{c}\text{number of neutrons scattered per second into the solid angle d}\Omega \\ \text{in the direction } \theta, \phi \text{ with final energy between E}_f \text{ and E}_f + \mathrm{dE}_f\end{array}\right)}{\Phi \mathrm{d}\Omega\mathrm{dE}_f} \tag{2.17}$$

Analogously to Eq. 2.16, the total neutron cross section comes from the following double integration

$$\sigma = \iint \frac{\mathrm{d}\sigma}{\mathrm{d}\Omega\mathrm{dE}_f}\mathrm{d}\Omega\mathrm{dE}_f \tag{2.18}$$

When a neutron scatters, it can cause a transition of the sample from one quantum state to another, but it does not modify the nature of the states themselves. Therefore, we consider the probability of a transition of the neutron-target system from an initial state λ_i to a final one λ_f. One can then use Fermi's Golden Rule to calculate the transition probability and obtain an expression to the partial differential scattering cross section. Furthermore, because the effective interaction in neutron scattering is weak, the Born approximation can be applied which assumes that both the incoming and scattered beam are plane waves

$$\left(\frac{\mathrm{d}^2\sigma}{\mathrm{d}\Omega\mathrm{dE}_f}\right)_{\lambda_f}^{\lambda_i} = \frac{k_f}{k_i}\left(\frac{m_n}{2\pi\hbar^2}\right)^2 |\langle k_f\lambda_f|\hat{V}|k_i\lambda_i\rangle|^2\delta(E_i - E_f + \hbar\omega) \tag{2.19}$$

Here $\hat{V}$ is the interaction potential that causes the transition. The only form of $\hat{V}(\mathrm{r})$ that, using the Born approximation, gives isotropic scattering is a delta function. Considering a rigid array of N nuclei, where the jth nucleus is denoted by r_j, the Fermi pseudo-potential is then defined as

$$\hat{V}(r) = \frac{2\pi\hbar^2}{m_n}\, b\, \delta(r - r_j) \tag{2.20}$$

where $\delta(r)$ is a Dirac delta function which takes the value unit at position r, and b is the nuclear scattering length. There are different scattering lengths depending on both atomic type and isotope. It can be complex and the real part may be either positive or negative depending on the energy of the incident neutron and the particular nucleus involved in the scattering. The imaginary part of b represents absorption and in most cases is small.

Coherent vs. incoherent

The scattering cross section can be subdivided into coherent and incoherent scattering, which is caused by the spin dependence of the scattering cross-section and, as mentioned in section 2.1, the different isotopes in the sample. For unpolarized neutrons, it is then convenient to express the partial differential cross section (2.17) as a sum of its coherent and incoherent parts

$$\frac{\mathrm{d}^2\sigma}{\mathrm{d}\Omega\mathrm{d}\mathrm{E}_f} = \left.\frac{\mathrm{d}^2\sigma}{\mathrm{d}\Omega\mathrm{d}\mathrm{E}_f}\right|_{coh} + \left.\frac{\mathrm{d}^2\sigma}{\mathrm{d}\Omega\mathrm{d}\mathrm{E}_f}\right|_{inc} \tag{2.21}$$

Coherent scattering results from interference effects between the nuclei and provides information about the cooperative effects among different atoms, such as elastic Bragg scattering or inelastic scattering by phonons or magnons. Incoherent elastic scattering is the same in all directions, so it usually appears as unwanted isotropic background in neutron scattering experiments, so we neglect this term. Incoherent inelastic scattering, on the other hand, results from the interaction of a neutron with the same atom at different positions and different times, thus providing information about atomic diffusion.

If in Eq. 2.20 the position $r_j = 0$, we find that the total cross section is

$$\sigma = 4\pi|b|^2 \tag{2.22}$$

In a real lattice however, *i.e.* a lattice where the nuclei is not strictly bound, the neutron does not see a crystal of uniform scattering potential but one in which the scattering varies from one point to another. If there are no correlations between nuclear position and scattering length, then only the average scattering potential can give interference effects, and thus coherent scattering. This average potential is proportional to $\bar{b}$, which is given by

$$\bar{b} = \sum_r c_r \, b_r \tag{2.23}$$

with c_r as the fractional concentration of r amount of isotopes. On the other hand, incoherent scattering will be proportional to the mean-square deviation, $\overline{|b-\bar{b}|^2} = \overline{|b|^2} - |\bar{b}|^2$. Eq. 2.18 is then rewritten as

$$\sigma = 4\pi\ \overline{|b|^2} \tag{2.24}$$

and the average coherent cross section per atom is

$$\sigma_{coh} = 4\pi|\bar{b}|^2 \tag{2.25}$$

Therefore, for the incoherent cross section per atom, being $\sigma = \sigma_{coh} + \sigma_{inc}$, we arrive at the following expression

$$\sigma_{inc} = 4\pi\overline{|b-\bar{b}|^2} \tag{2.26}$$

There are a few examples for which the incoherent scattering is dominant. A typical strong source of incoherent scattering is hydrogen, where the incoherence is due to a strong spin dependence of the interaction between the neutron and the proton, and which in fact presents the main source of background signal in neutron spectra presented throughout the thesis[3].

2.2.3 Response Function S(Q, ω)

As mentioned before, in a neutron scattering experiment, one is essentially measuring the scattered intensity (per incident neutron) as a function of **Q** or **E**. Such intensity is typically referred to as the response function and is defined

$$S(\mathbf{Q},\omega) = \frac{1}{2\pi\hbar N}\sum_{i,j}\int_{-\infty}^{\infty} dt\ \langle e^{-iQ\cdot r_i(0)}\ e^{iQ\cdot r_j(t)}\rangle\ e^{-i\omega t} \tag{2.27}$$

where N is the number of nuclei, with the nucleus labelled i at position r_i at time zero, while the nucleus labelled j is at position r_j at time t. The response function is also often called the scattering law or dynamic structure factor. S(**Q**, ω) depends only on the momentum and energy transferred from a neutron to the sample, and not on the absolute values of $\mathbf{k}_i$ and $\mathbf{k}_f$. It contains information on both the positions and motions of the atoms comprising the sample. In 1954, Van Hove [129] showed that the response function can be written in terms of time-dependent correlations between the positions of pairs of atoms in the sample. Van Hove's result implies that S(**Q**, ω) is proportional to the Fourier transform of a function that gives the

[3] A table of the coherent and incoherent scattering lengths and cross sections for different elements can be found in the NIST Center for Neutron Research

probability of finding two atoms a certain distance apart.

For coherent, elastic nuclear scattering, in the more typical case where the lattice has more than one atom per unit cell, the differential cross section generalizes to

$$\left.\frac{d\sigma}{d\Omega}\right|_{\text{coh}}^{\text{el}} = N\frac{(2\pi)^3}{\upsilon_0}\sum_{\mathbf{G}}\delta\left(\mathbf{Q}-\mathbf{G}\right)\left|F_{\text{N}}(\mathbf{G})\right|^2 \tag{2.28}$$

where υ_0 is the unit cell volume and

$$F_{\text{N}}(G) = \sum_j \bar{b}_j\ e^{iG\cdot d_j}\ e^{-W_j} \tag{2.29}$$

is the nuclear structure factor that contains information over all nuclei at positions d_j within one unit cell. The exponent component W is an additional pre-factor that arises from the thermal motion of atoms about their nominal positions. Since an atom can contribute to the constructive interference of Bragg scattering only when it is located exactly at its official position at a lattice site, this scattering becomes weaker the more the atoms vibrate. The factor W by which Bragg scattering is attenuated due to thermal motion is called the Debye-Waller factor. For small displacements

$$W = e^{-\mathbf{Q}^2\langle u^2\rangle\frac{1}{2}} \tag{2.30}$$

where $\langle u^2\rangle$ is the mean square displacement and $\mathbf{Q}$ the scattering vector. This means that the intensity of the Bragg peaks decreases for increasing $\mathbf{Q}$.

Phonons

In section 2.1.2, we discussed phonon dispersion curves, where it was said that if we have a lattice with N atoms per cell, there will be a total of 3N distinct phonon branches with frequencies $\omega_j(\mathbf{q})$, the index of j having three values. Well, to each $\omega_j(\mathbf{q})$ there corresponds a polarization vector $\xi_j(\mathbf{q})$, two components of which are perpendicular and another one is parallel to $\mathbf{q}$. The typical way to measure a phonon is to work at a fixed wave vector $\mathbf{Q} = \mathbf{G}+\mathbf{q}$ and vary the frequency through a branch at $+\omega_j(\mathbf{q})$ or $-\omega_j(\mathbf{q})$. In a neutron scattering measurement, if one creates or destroys a phonon, the one-phonon inelastic coherent cross section will be given by

$$\left.\frac{\mathrm{d}^2\sigma}{\mathrm{d}\Omega\mathrm{d}\mathrm{E}_f}\right|_{\text{coh}}^{\text{inel}} = \frac{\mathbf{k}_f}{\mathbf{k}_i}\frac{(2\pi)^3}{\upsilon_0}\sum_G\sum_{j\mathrm{q}}\delta\left(\mathbf{Q}+\mathbf{q}-\mathbf{G}\right)\left|H^j_{\mathbf{q}}(\mathbf{Q})\right|^2\times S_j(\mathbf{q},\omega) \tag{2.31}$$

Here we define the dynamic structure factor H($\mathbf{Q}$) with the polarization vectors

$$\mathrm{H}^{j}_{\mathbf{q}}(\mathbf{Q}) = \sum_{j} \bar{b}_j \; e^{[-W_j(\mathbf{Q})+i\mathbf{Q}\cdot d_j]} \left[\mathbf{Q}\cdot\xi^{j}_{d}(\mathbf{q})\right] \; M_j^{-1/2} \tag{2.32}$$

where M_j and d_j are the mass and position of the jth atom, respectively. Embedded in the dynamic structure factor is also the so called form factor

$$\mathrm{F}_{\mathbf{q}}(\mathbf{Q}) = \bar{b}_j \; e^{[-W_d(\mathbf{Q})+i\mathbf{Q}\cdot d_j]} \tag{2.33}$$

which by itself gives us information about the scattering amplitude of a wave by an isolated atom. In the last term of the one-phonon inelastic coherent cross section, we have the response function for each individual nucleus inside a unit cell

$$S_j(\mathbf{q},\omega) = \frac{1}{2\omega_j(\mathbf{q})}\left[n_j(\mathbf{q})\;\delta\{\omega+\omega_j(\mathbf{q})\} + \{1+n_j(\mathbf{q})\}\delta\{\omega-\omega_j(\mathbf{q})\}\right] \tag{2.34}$$

where n_j is the Bose factor. The two expressions containing the delta functions correspond to the creation and annihilation of phonons. In the limit $T \to 0$ only the first process occurs, since at absolute zero there are obviously no phonons to be annihilated.
Within the same harmonic approximation, the incoherent cross section for phonon scattering can be written as

$$\left.\frac{\mathrm{d}^2\sigma}{\mathrm{d}\Omega\mathrm{d}\mathrm{E}_f}\right|^{\mathrm{inel}}_{\mathrm{incoh}} = \frac{\mathbf{k}_f}{\mathbf{k}_i}\sum_{d}(b^{d}_{inc})^2\frac{1}{M_d}e^{-2W_d(\mathbf{Q})}\sum_{j\mathbf{q}}|\mathbf{Q}\cdot\xi^{j}_{d}(\mathbf{q})|^2 S_j(\mathbf{Q},\omega) \tag{2.35}$$

During a standard triple-axis experiment, the measured integrated intensity of the phonon scattering basically amounts to Eq. 2.31.

2.2.4 Resolution Function

While probing a sample with a computer-controlled spectrometer, one can easily opt between either scan the energy transfer while sitting at a specific point in reciprocal space, or scan along a particular direction in reciprocal space while maintaining a constant energy transfer. However, the energy and momentum transfers of the neutrons are distributed within some small region about the average values ($\mathbf{Q}_0$, ω_0). Therefore, the spectrometer is characterized by a resolution function $R(\mathbf{Q}-\mathbf{Q}_0$, $\omega-\omega_0)$, which peaks at $(\mathbf{Q}_0,\omega_0)$ and decreases for deviations ($\Delta\mathbf{Q}$, $\Delta\omega$). As a result, to properly describe the measured signal, a convolution of the spectrometer resolution function and the scattering function $S(\mathbf{Q},\omega)$ is required. The resolution

function is defined by [130]

$$R(\mathbf{Q},\omega) = \frac{\hbar^2}{m_n}\int d\mathbf{k}_i d\mathbf{k}_f P_i(\mathbf{k}_i)P_f(\mathbf{k}_f)\delta\left(\mathbf{Q}-\mathbf{k}_f+\mathbf{k}_i\right)\times\delta\left[\omega-\left(\frac{\hbar^2}{m_n}\right)\left(\mathbf{k}_i^2-\mathbf{k}_f^2\right)\right] \quad (2.36)$$

where P_i and P_f are distribution functions of the neutron wavevectors $\mathbf{k}_i$ and $\mathbf{k}_f$ transmitted by the collimators. The constant-amplitude contours for the resolution function form a set of nested ellipsoids in $(\mathbf{Q},\omega)$ space, with a certain inclination. Note that, up until now we have set $\mathbf{Q}$ equal to $k_i - k_f$. Changing from one convention to the other has an important consequence for the orientation of the resolution ellipsoid in ($\mathbf{Q}$, ω) space: it results in a reflection about $\omega = 0$. The effective measured signal becomes

$$I(\mathbf{Q}_0,\omega_0) = \int_{-\infty}^{\infty} d^3\mathbf{Q}d\omega\ S(\mathbf{Q},\omega)\bullet R(\mathbf{Q}-\mathbf{Q}_0,\omega-\omega_0) \quad (2.37)$$

meaning that what one actually measures is not $S(\mathbf{Q},\omega)$ but rather a 4-dimensional convolution of $S(\mathbf{Q},\omega)$ with the resolution function.

2.2.5 Damped harmonic oscillator model

In real systems, phonon–phonon and electron-phonon interactions tend to give single phonons a finite lifetime. A way to incorporate this dissipation is through the damped harmonic oscillator (DHO) model, in which the effect of phonon damping is accommodated by the replacement of the delta functions with lorentzians ones, along with re-normalization of the phonon frequencies.

The experimental neutron spectra can be described by a sum of phonon terms on top of a flat background (Bg). Each phonon is typically accounted for by a DHO [131]. The spectra can then be described by the following expression

$$I(\mathbf{Q},\omega) = Bg + \left[1-exp(-\frac{\hbar\omega}{k_bT})\right]^{-1}\sum_j |F_j(\mathbf{Q})|^2\frac{\omega\Gamma_j}{(\omega^2-{\omega_j}^2)^2+(\omega\Gamma_j)^2} \quad (2.38)$$

where ω_j represents the energy, Γ_j the damping and $F_j(\mathbf{Q})$ is the dynamical structure factor of the j-th phonon. The number of mode depends on how many peaks are visible. The prefactor of DHOs is the phonon population factor. For acoustic phonons, the dynamical structure factor can be written $F(\mathbf{Q}) = \mathbf{Q}.\epsilon$ where ϵ represents the phonon polarization.

In all cases, the full scattering function, $I(\mathbf{Q},\omega)$, is next convoluted by the 4D spectrometer resolution function of the instrument (Eq. 2.36), and used to fit the experimental data. The presence of several phonon lines in a given phonon bundle

would have the effect to increase the damping when fitted by a DHO due to the energy resolution function.

2.3 Neutron sources

Neutrons can be produced in a number of ways, *e.g.* as by-products of cosmic radiation or radioactive decay of heavy nuclei. The intensity of a neutron source, which depends on the type of process employed, is usually described by the fluence rate and presents an important factor for research purposes. Currently, neutron sources created for the purpose of materials investigation by scattering are either based upon chain reaction in a nuclear reactor or upon accelerator-driven spallation processes. Nuclear research reactors, as opposed to power reactors, incorporate beam ports that allow neutrons to escape the reactor core. These ports also permit samples to be inserted into the core. In such reactors, neutrons arise from the spontaneous fission of ^{235}U

$$^{235}U + n(th) \rightarrow 2{-}3 \text{ neutrons} + \text{fission products} + \Delta E \tag{2.39}$$

where the released energy ΔE is of the order of 200 MeV. During operation, there is an in-growth of plutonium that will also fission. In the case of a spallation source, a pulsed production of neutrons is obtained by bombarding a target of heavy elements with high-energy particles, typically accelerated protons.

At the Laboratoire Léon Brillouin (LLB, spectrometers are located around the reactor Orphée, which is a "pool" type 14 MW reactor operated by the Commissariat a l'Energie Atomique et aux Energies Alternatives (CEA) (see Fig. 2.5.a). The compact, light-water moderated core provides up to 3 x 10^{14} $cm^{-2}s^{-1}$ thermal flux in the surrounding heavy water reflector tank. The heavy water tank is equipped with

Figure 2.5: Pictures of (a) the Orphée at LLB and (b) the High-Flux reactor at ILL.

Table 2.2: Terminology and kinetic energy of free neutrons moderated in different mediums.

	Energy range [meV]
Cold neutrons	$\leqslant 10$
Thermal neutrons	10 - 100
Hot neutrons	100 - 500
Epithermal neutrons	$\geqslant 500$

three local moderators: two cold sources (liquid hydrogen at 20 K) and one hot source (graphite at 1400 K). The experimental areas are located either in the reactor building or along the neutron guides of a guide hall in an adjacent section of the building.

Similarly to Orphée, the high-flux reactor (HFR) at the Institut Laue-Langevin (ILL) is also a pool type reactor, cooled and moderated by heavy water (see Fig. 2.5.b). The reactor block houses two cold sources and one hot source, thus guaranteeing a wide range of neutron energies. However, the HFR provides the most intense continuous neutron flux in the world in the moderator region with 1.5 x 10^{15} neutrons per $cm^{-2}s^{-1}$, producing a power output of 58.3 MW. Fifteen horizontal beam tubes and four vertical beam tubes direct the neutrons towards the experimental areas and equipments.

The produced free neutrons can be classified according to their kinetic energy, which is typically given in electron volts (eV) or milielectron volts (meV). Neutrons produced in nuclear reactions typically have energies in the MeV regime, so, to be useful in materials research, they must have their energies reduced. This is done via the so called "moderation process" which is performed by a large number of successive collisions with a material that scatters strongly, but absorbs weakly. Because of this moderation process, the energy of the free neutrons is also called neutron temperature, in relation to the temperature of the medium in which they are moderated. There are wide number of classifications of free neutrons according to their kinetic energies. However, for practical purposes in neutron based experiments conducted in reactors such as the ones above mentioned, neutrons are roughly divided into four energy ranges. In Table 2.2 we present the typical classifications used and the terminology employed in this work, noting that different ranges with different names can be used.

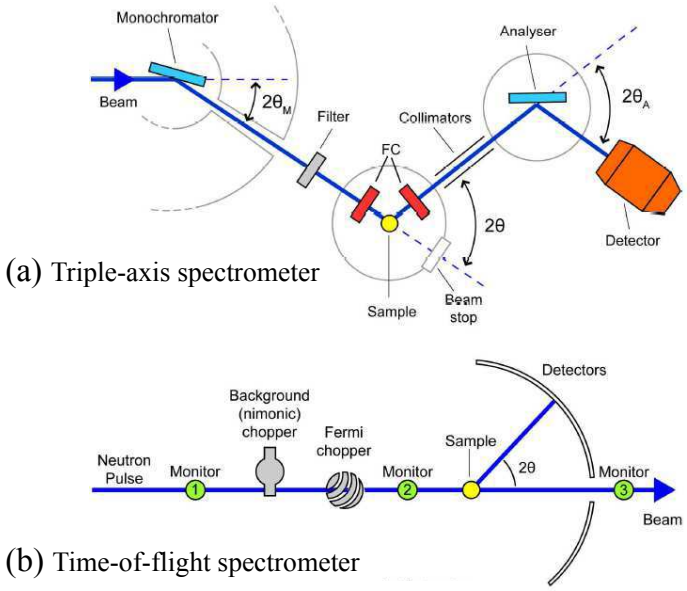

Figure 2.6: Schematic diagrams the two types of spectrometers employed: (a) triple-axis spectrometer (TAS) and (b) time-of-flight (ToF) chopper spectrometer.

2.4 Neutron instrumentation and experimental setup

A wide range of instrumentation has been developed to apply produced neutrons to various different research purposes. Some instruments deal with the study of the crystal structure of materials, others with excitations in materials, others again with the structure of biomolecular aggregates, with properties of thin films, and so forth.

Inelastic neutron scattering spectroscopy measurements were conducted using both Triple-axis spectrometer (TAS) and Time-of-flight (TOF), at two different neutron sources: the LLB and the ILL, both of which are reactor sources. Here I briefly describe the instruments utilized at such locations, namely the TAS and ToF spectrometers. Further information on the instruments used here can be found on the LLB and ILL websites [132, 133], and a more comprehensive discussion of neutron scattering using TAS can be found in the textbook by Shirane *et al.* [134]. The particular experimental setups for the measurements performed are covered below, in the sections regarding the relevant technique.

2.4.1 Inelastic Neutron Scattering Spectroscopy

2.4.2 Triple-axis spectrometer (TAS)

Developed by Bertram Brockhouse [135], the TAS is arguably the most versatile and useful instrument for both elastic and inelastic scattering since it allows for a

controlled measurement of the scattering function S($\mathbf{Q}$,ω) at essentially any point in momentum ($\hbar\mathbf{Q}$) and energy space ($\hbar\omega$).

The name "triple-axis" refers to the three axes of the monochromator, sample and analyser. The monochromator and analyser axes house single crystals (dummy samples) with well known structures. Each crystal can be rotated so that when used in conjunction with Bragg law, these crystals enable selection of a particular neutron wavelength for transmission to the sample or to a detector as appropriate. In other words, the monochromator controls incident energy of neutrons on the sample and the analyser controls the final energy of neutrons that reach a detector. The path of the neutron beam is kept in the same horizontal plane, also denoted the scattering plane. This way, the monochromator and analyser enable complete control over both Q and the incident final energies of neutrons used to study a sample. The instruments are large, mainly because of the necessary shielding which keeps the radiation levels low in the neighbourhood of the instrument and keeps the background measured by the detector at the lowest possible level.

A schematic diagram of a TAS is shown in Fig. 2.6.a, and the individual components are highlighted below:

- **Source**. TheTAS uses a beam of cold or thermal neutrons. Most usually, a neutron guide is used to transport the beam to areas far from the source where the stray background is lower.
- **Monochromator**. The beam is diffracted by a monochromator, which selects the neutron energy, E_i, typically in the range 14-100 meV at a thermal moderator, or 2.5-14 meV for a cold moderator.
- **Filter**. The monochromatised beam is almost always polluted with higher order scattering, from $n > 1$ in Bragg's law. Filters are typically placed in the beam after the monochromator to remove higher order harmonics which also satisfy the Bragg condition of the monochromator, but which would contaminate the measurements.
- **Collimator**. Control of the beam divergence within the horizontal scattering plane is typically achieved through the use of Soller collimators, positioned typically between the monochromators. Collimators may also be inserted before the monochromator (rarely) and after the analyser (sometimes).

Experimental conditions

On all TAS instruments, monochromators and analysers were made from the 002 reflection of Pyrolithic graphite (PG). Cold (below $\sim$ 15 meV) and thermal TAS have been used to cover the full energy range of the phonon spectrum in the four

hybrid lead halide perovskites, MAPI, MAPB, FAPB and FAPI.

On 4F1/4F2 and IN12 TAS located (on cold-neutron sources), respectively, at LLB and at the ILL, a constant final neutron wave vector of $k_f = 1.55\text{Å}^{-1}$ was utilized with a beryllium (Be) filter to remove high-order neutrons in the beam. In addition for the measurement on IN12, a velocity selector was used to remove neutrons with high order harmonics from the incident beam. For the particular case of the measurement of acoustic phonons at the (220) Bragg reflection in α-$FAPbI_3$, the neutron wave vector was changed to $k_f = 1.70\text{Å}^{-1}$ and the Be filter was removed. At the thermal TAS 1T at LLB, a constant final neutron wave vector of $k_f = 2.662\text{Å}^{-1}$ was used with a PG filter to remove neutrons with high order harmonics. The energy resolution of cold TAS goes from ~ 0.25 to 0.5 meV for an incident energy ranging from 5 to 16 meV, while for the thermal TAS (1T) it goes from ~ 1 to 3 meV for an incident energy ranging from 15 to 50 meV.

For the study of elastic constants (chapter 3), all samples have been analysed in their cubic phase, corresponding to RT, except for $MAPbI_3$ which has been warmed up to 340 K, above its tetragonal-cubic phase transition. Samples were mounted in a scattering plane such that the high symmetry reciprocal directions [100] and [011] were within the horizontal plane. Throughout the present manuscript, the indices refer to the high temperature cubic phase of the HOP lattice.

For the temperature-dependent measurements, all samples have been attached to the cold head of cryogenerator at LLB or a cryostat at ILL. In specific, for the low temperature measurements, temperatures of 5 K were reached where all these hybrid organolead perovskites (HOP) are in the orthorhombic phase. However, throughout the present manuscript, the indices refer to the high temperature cubic phase of the HOP lattice. Samples were mounted in a scattering plane such that the high symmetry reciprocal directions [100] and [011] were within the horizontal plane. When necessary, goniometers were used to reach out-of-plane momentum position, such as M=(5/2,1/2,0). It should be stressed that MA and FA molecules were not deuterated giving rise to a large incoherent neutron scattering from the various hydrogen atoms from the organic part of the compounds. The samples are also fixed to a vanadium sheet (see below, Fig. 2.8) which results in additional incoherent elastic scattering.

2.4.3 Time-of-flight (ToF)

While TAS's measure one point in Q-E space at a time, ToF spectrometers allow a large coverage of Q-E space to be studied in a single measurement. This is because in neutron ToF spectroscopy the determination of $S(\mathbf{Q}, \omega)$ is achieved through

measuring the neutron energy by way of its flight time over a known distance. The interaction between the neutron and sample causes a change in the flight time of the neutron and this is used to infer the energy exchanged with the sample. To achieve this it is necessary to have a pulsed beam, which, in order to be adjustable and controllable, is preferably obtained by the use of choppers. A disk chopper is a rotating disk of some neutron absorbing material with a window that is transparent to neutrons. By changing the phase and the rotation speed of the chopper it is possible to tailor the neutron pulse to the experiment. Mathematically speaking, substituting E_f from Eq. 2.5, leads to the following expression:

$$E = E_i - \frac{m_n D^2}{2t^2} \tag{2.40}$$

where E_i is chosen by the chopper frequency and phase, D is the distance from sample to detector and t is the time-of-flight of the neutrons from the same sample and detector. It is clear from Eq. 2.40 how the scattering vector is dependent on the time-of-flight and how the energy transfer is obtained from the latter. Fig. 2.6.b shows a schematic illustration of the IN5 ToF spectrometer at ILL used for this work.

Experimental conditions

Measurements with the ToF instrument IN5 were performed with an incident neutron wavelength of $\lambda = 2$Å ($\equiv 3.14$ Å^{-1}), corresponding to an energy resolution which varies from 1.15 meV at elastic position to 0.8 meV at 15 meV energy transfer. The measured four-dimension $S(\mathbf{q}, \omega)$ data were reduced and visualized using the Horace software suite. Cuts shown in chapters 3 and 4 were made along [hh2] direction, with an integration over -0.1 $< l <$ 0.1 (*i.e.* [002+l]) and -0.1 $< \eta <$ 0.1 in [η,-η, 0].

2.5 Optical spectroscopy techniques

2.5.1 Raman Scattering Spectroscopy

Raman spectroscopy, named after Indian physicist Sir C. V. Raman, is a spectroscopic technique used to observe vibrational, rotational, and other low-frequency modes in a system. Raman scattering relies on inelastic scattering. The laser light interacts with molecular vibrations, *i.e.* phonons or other excitations in the system, resulting in energy loss or gain during the scattering process, and therefore an increase or decrease in wavelength, respectively. If the molecule is promoted from a

ground state to a virtual one and then drops back down to a (higher energy) vibrational state, then the scattered photon has less energy than the incident photon, and therefore a longer wavelength. This is called Stokes scattering. If the molecule is in a vibrational state to begin with and after scattering is in its ground state then the scattered photon has more energy, and therefore a shorter wavelength. This is called anti-Stokes scattering. This process is illustrated in Fig. 2.7.a. The shift due to the Raman effect is determined by the spacing between the vibrational states and the ground states *i.e.* by the phonons of the system. The Stokes and anti-Stokes scattered light will be shifted an equal distance on opposite sides of the Rayleigh scattered light. Therefore the spectrum is symmetrical about the wavelength of light used, apart from the difference in intensities. Typically one uses the Stokes half of the spectrum due to its greater intensity.

Experimental conditions

Raman scattering in MAPB has been performed under an optical microscope and a T64000 Jobin-Yvon double pass diffractometer working with 18000 trts/mm gratings. The radiation of a krypton laser emitting at 647 nm was tightly focused into the sample with a $\times 100$ objective. In order to avoid photo-induced effects, the incident power was always kept lower than 2 mW. The spectra have been obtained in the backscattering geometry with the incident light parallel to the [001]-cubic crystallographic direction of the sample. The incident polarization was parallel to the [110] direction and the results shown in the main text correspond to the polarized spectra (*i.e.* scattered light // $[1\bar{1}0]$).

All the spectra have been fitted using slightly modified version the DHO used in INS (Eq. 2.38). The model accounts for ω_1, ω_2, ω_3, whose scattering spectral function for a given mode i reads

$$I(\omega) = S_{QE}(\omega) I_{QE} + \sum_i I_i S_i \omega + Bg \tag{2.41}$$

where Bg is the background. Here $S_i\omega$ represents the response function of the mode i which is can be described as

$$S_i\omega = \frac{\mathrm{n}(\omega) + 1}{1/(\omega_{0i}^2 - \omega^2 - i\Gamma_i\omega)} \tag{2.42}$$

$\mathrm{n}(\omega)$ is the Bose-Einstein population factor while ω_{0i} and Γ_i are the DHO frequency and damping of the mode submitted to a driving force (the incident electric field),

respectively. The analysis also required a central component (in black in Fig. 5.3) of spectral form

$$S_{QE}(\omega) = \frac{\mathrm{n}(\omega) + 1}{\omega/(\Gamma_{QE} - i\omega)} \tag{2.43}$$

where Γ_{QE} is the half width at half maximum of the quasi-elastic (QE) peak.

2.5.2 Brillouin light scattering (BLS)

Brillouin light scattering, named after Léon Brillouin, refers to the interaction of light with the material waves in a medium. Brillouin spectroscopy is similar to Raman spectroscopy in many ways; in fact the physical scattering processes involved are identical. However, the type of information gained is significantly different. While Raman scattering, involves interactions with high frequency molecular rotational and vibrational modes, in BLS on the other hand, photons are scattered by interactions with low-frequency phonons, providing information regarding elastic properties. As a result, BLS spectroscopy is typically used to measure the elastic behaviour of a sample using an interferometer and Raman spectroscopy to determine the chemical composition and molecular structure of a material using either an interferometer or, for example, a dispersive (grating) spectrometer. Fig. 2.7.b shows a typical spectrum of spontaneous scattering from solid state matter, as measured by different light spectroscopy techniques.

Experimental conditions

Brillouin light scattering spectroscopy experiments have also been used to study the angular dispersion of acoustic phonons in $MAPbBr_3$ and $FAPbBr_3$ (measurements in the iodide-based samples were not possible with the current set-up as they are not transparent to the laser light). Spectra were recorded at 647.1 nm by using a krypton ion laser and a tandem of Fabry-Perot interferometers where each interferometer is triple passed giving a contrast larger than 10^{-12}.

2.6 Sample Preparation

Single crystals of four different hybrid lead halide perovskites have been studied by INS and Raman spectroscopies: $MAPbBr_3$, $FAPbBr_3$, $MAPbI_3$, and α-$FAPbI_3$. MA and FA stand for methylammonium and formamidinium molecules, respectively. All single crystals, of typical size of 200 mm^3 for all compounds (except for FAPI where only a volume of $\sim$50 mm^3 could be achieved), were synthesized at the Institut des Sciences Chimiques de Rennes (ISCR) and the King Abdullah University of Science

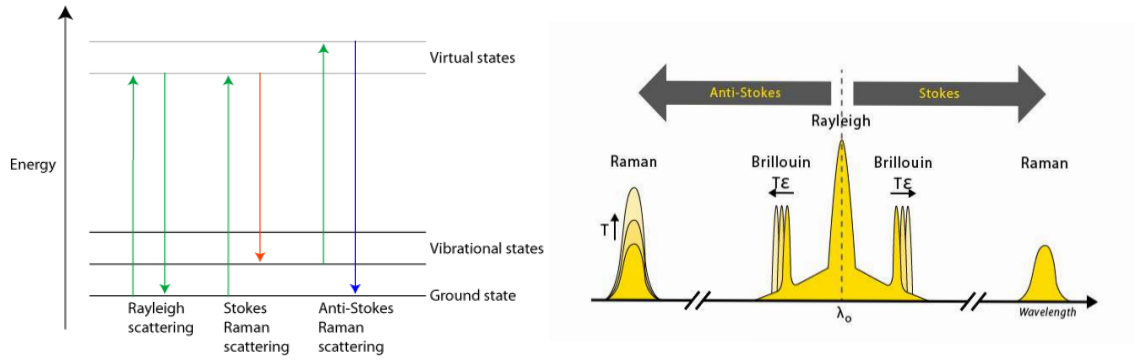

Figure 2.7: (a) Energy-level diagram showing the states involved in Raman spectra. (b) Illustrative comparison of the typical wavelength, *i.e.* energy, shifts involved for each technique.

and Technology (KAUST) Solar Center. These can be seen in Fig. 2.8.

Methylammonium Lead Bromide

$MAPbBr_3$ single crystals were grown by ITC [114]. A solution of $MAPbBr_3$ was prepared in DMF with 1 M concentration and was filtered with a 0.2 μm pore size PTFE filters. 3 ml of the obtained solution were then placed into a 5 ml beaker which was introduced in an oven at 80 °C and kept for 3 h. To increase their size, the formed crystals were extracted from the first beaker and place into another beaker containing fresh filtered solution at the same temperature overnight.

Methylammonium Lead Iodide

$MAPbI_3$ single crystals were grown by ITC [74]. A solution with 1 M concentration of $MAPbI_3$ was prepared in GBL and was filtered with a 0.2 μm pore size PTFE filters. Then 3 ml of the obtained solution were placed into a 5 ml vial which was placed in an oven at 60 °C. The temperature was gradually increased to 110 °C and kept for 1 days to further increase the size of the crystals.

Formamidinium Lead Bromide

$FAPbBr_3$ single crystals were grown by ITC [114]. After the filtration using PTFE filters with a 0.2 μm pore size, 3 ml of 1 M solution of $FAPbBr_3$ in DMF:GBL (1:1 v/v) were placed into a 5 ml beaker which was introduced in an oven at 40 ° C. The temperature was then gradually increased to 52 °C and kept for 5 h and at 60 °C for 3 h. The size of the crystal can be further increased through the gradual increase of temperature.

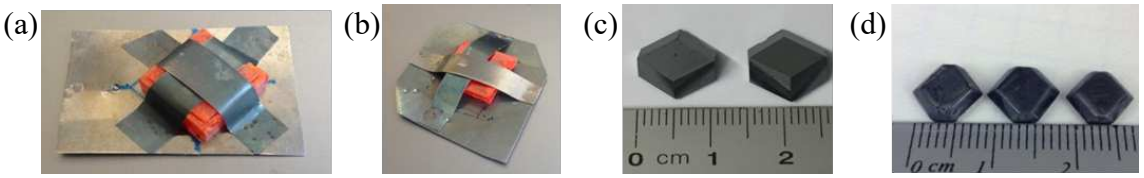

Figure 2.8: Photos of the HOP crystal samples used in the experiments: (a) MAPB, (b) FAPB, (c) MAPI and (d) FAPI. In the case of the Br-containing compounds, we also show the vanadium support sheets where the crystals were attached for the neutron scattering experiments.

Formamidinium Lead Iodide

$FAPbI_3$ single crystals were grown by ITC [74]. A solution of $FAPbI_3$ was prepared in GBL with 1 M concentration and was filtered with a 0.2 μm pore size PTFE filter. Then 3 ml of the obtained solution were placed into a 5 ml vial which was immersed in an oil bath at 80 °C. The temperature was slowly increased to 105 °C. Subsequently a fresh filtered solution can be added on one formed crystal in a vial to increase the size through the gradual increase of temperature.

Metastable nature of $FAPbI_3$

The α-phase of $FAPbI_3$, *i.e.* the photoactive phase, is metastable and only lasts a maximmum of 7 days at RT. In this work we were able to measure optical phonons on a fresh sample within that first period of 7 days, mainly due to the low temperature (5 K) working conditions. Only once we started heating up the sample, for the temperature dependent measurements, did it start showing signs of degradation into the yellow phase (δ-phase), which presents no particular physical interest. The α-phase can, however, be restored back into the black α-phase upon heating/annealing, which was indeed demonstrated in small single crystals [74]. However, on large single crystals such as ours, only part of the sample is restored to a single grain and most of the sample remains as a powder.

Chapter 3

Elastic softness of hybrid lead halide perovskites

Here we investigate by coherent inelastic neutron scattering spectroscopy and Brillouin light scattering, low frequency acoustic phonons in four different hybrid perovskite single crystals: $MAPbBr_3$, $FAPbBr_3$, $MAPbI_3$ and α-$FAPbI_3$. We report a complete set of elastic constants characterized by a very soft shear modulus C_{44}. We observe a systematic lower sound group velocity in the technologically important iodide-based compounds compared to the bromide-based ones. The findings suggest that low thermal conductivity and hot phonon bottleneck phenomena are expected to be enhanced by low elastic stiffness, particularly in the case of the ultrasoft α-$FAPbI_3$.

3.1 Introduction

In this chapter, we have investigated low frequency structural excitations in the cubic phases of the most relevant compounds implemented in HOPs, namely $MAPbBr_3$, $FAPbBr_3$, $MAPbI_3$ and α-$FAPbI_3$, in their single crystal form; from now on referred to as MAPB, FAPB, MAPI and FAPI, respectively. We report a complete set of elastic constants, via the corresponding sound velocities, and we relate the results to the lower thermal conductivity found in HOP compounds and the hot phonon bottleneck hypothesis proposed for such systems. For that purpose, dispersions of the acoustic phonons have been measured around main Bragg reflections using INS. Complementary BLS experiments have also been used to determine sound velocities in the bromide-based compounds. The experimental conditions and procedure of both techniques are detailed in sections 2.4.2 (INS) and 2.5.2 (BLS).

3.2 Results

Fig. 3.1 show the low energy INS spectra of acoustic phonons in MAPB, FAPB, MAPI and FAPI, at around main Bragg reflections, where both constant energy and Q scans were performed. Using the (200) position as an example, longitudinal acoustic (LA) and transverse acoustic (TA) acoustic modes were measured at different reciprocal space positions $Q = (200) + q$ in HKL units, with q along (LA) and perpendicular (TA) to [200] (for TA q is parallel to [011])[1]. Clear acoustic phonon modes are observed on top of a strong background. As shown by constant Q-scans, the background results from large QE signals, likely coming from incoherent scattering of hydrogen atom excitations present in the MA/FA molecules, as it has been previously studied on powder samples in MAPB [136]. Energy scans performed at various momentum vectors around the Bragg positions revealed that the QE signal occurring in the energy window of the acoustic phonons is almost independent of the sample orientation and weakly dependent of the longitudinal momentum. In constant-energy scans (*e.g.* Fig. 3.1.j), this incoherent QE corresponds to a flat contribution, whereas acoustic phonons show up as a double peak structure at symmetric positions of the Bragg reflection. As a result, even though the background is relatively large, one can easily separate it from the dispersing and symmetric phonon modes. The reason for opting with either energy or Q scans is mostly connected to the signal to noise ratio, which in this case can be thought of as a structure factor/QE ratio. The dynamic structure factor (see Eq. 2.32), varies for

[1] At any time, the reader is welcome to refer to Appendix A for a quick refresher on crystal lattices and reciprocal spaces.

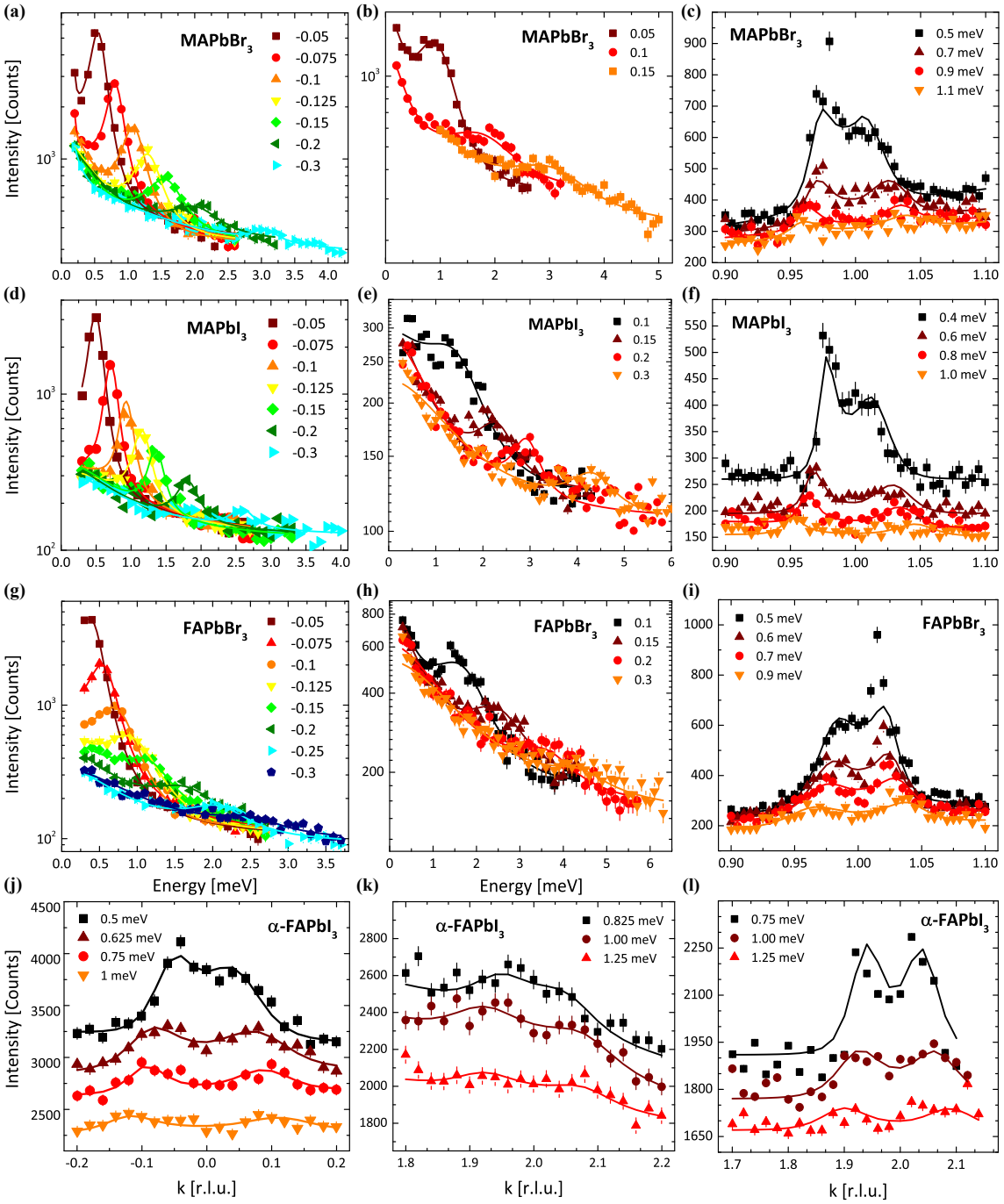

Figure 3.1: TA phonon spectra measured by INS TAS spectra measured in the cubic phase of the four HOPs. With the exception of MAPI (340 K), all other compounds were studied at RT. transverse acoustic (TA) phonons in (a) MAPB, (d) MAPI and (g) FAPB for different Q positions going away from the (002)≡(200) Bragg peak (*i.e.* Q = (k k 2)); and of (j) FAPI for different energy values. longitudinal acoustic (LA) phonons in (b) MAPB, (e) MAPI and (h) FAPB for different Q positions going away from the (002) Bragg peak (*i.e.* Q = (0 0 2+k)), and (k) FAPI for different energy values. transverse acoustic (TA) phonons in (c) MAPB, (f) MAPI and (i) FAPB for different energy values around the the (111) Bragg peak and (l) longitudinal acoustic (LA) phonons for FAPI different energy values at the (220) Bragg reflection.

different reciprocal points. Therefore, when we have a favourable form factor for a specific Bragg point (*i.e.* (002)), its best to perform constant Q scans. Conversely, for (111) we find it necessary to perform constant energy scans to improve the signal to noise ratio. This becomes even more relevant in the case of FAPI, since due to its unstable nature (see section 2.6), we were loosing scattering intensity by the hour as the sample gradually degraded.

All neutron spectra has been fitted with the DHO model described in section 2.2.5 (Eq. 2.38), from which the phonon energy can be extracted. Some constraints were imposed during the refinements of the data so to avoid correlations between parameters. In particular, within each dispersing phonon branch group, the dynamical structure factor and the damping Γ_j have been constrained in order to have a consistency within each branch. This way the error bars of the fitted phonon positions are noticeably reduced since the only remaining free parameter is then the phonon energy in constant Q-scans or its position in momentum in constant energy scans. In the constant Q-scans, a QE centered at zero energy was also necessary to include to achieve a proper fit, while for constant energy scans a constant background was used.

By varying the distance q to the nearest Bragg peak, Γ point (not to be confused with the phonon damping Γ_j), one can draw the dispersion curves, which are reported in Fig. 3.2. Each sub-figure represents measurements at a different Bragg position or propagation direction. We derive the phonon sound velocity v from linear regressions along most directions and then, with simple rules of elasticity in cubic systems [137], readily determine the corresponding elastic constants for the four perovskite compounds.

The elastic constant tensor C relates the strain and stress tensors in a linear fashion, so that

$$\sigma_{ij} = \sum_{kl} C_{ijkl}\varepsilon_{kl} \tag{3.1}$$

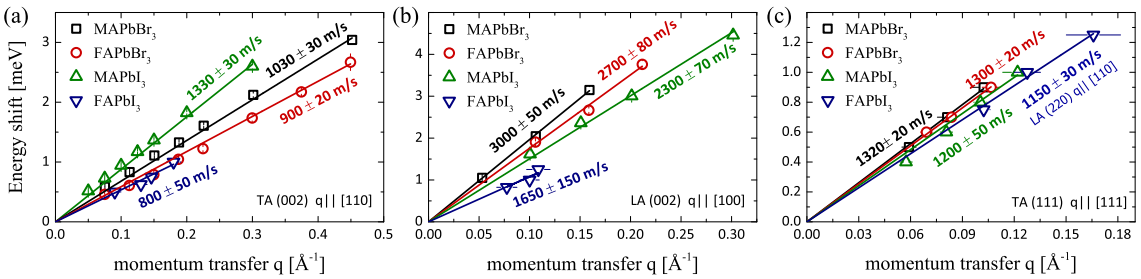

Figure 3.2: Acoustic phonon dispersion curves for the four HOPs, as measured by INS. (a) TA and (b) LA phonons at (002); (c) TA phonons at (111) in MAPB, MAPI and FAPB and LA phonons at (220) in FAPI.

Table 3.1: Sound velocities of the four different compounds, measured by INS and BLS, along various directions. For purposes of comparison, we also present sound velocities obtained by Ultrasonic Scattering (US), from other recent studies [10].

		$\mathbf{V}_{\mathrm{TA1}}$ q‖[110]	$\mathbf{V}_{\mathrm{TA2}}$ q‖[110]	$\mathbf{V}_{\mathrm{TA}}$ q‖[111]	$\mathbf{V}_{\mathrm{LA}}$ q‖[100]	$\mathbf{V}_{\mathrm{LA}}$ q‖[110]
MAPB	INS	1030±30		1320±20	3000±50	
	BS	955±15	1742±20		2910±10	
	US				∼3400[2]	
FAPB	INS	900±20	1400±100	1300±20	2700±80	
	BS	620±20	1700±20		2870±30	
MAPI	INS	1330±30		1200±50	2300±70	
	US				∼3650[1]	
FAPI	INS	800±50			1650±150	1150±30

[1] at 330 K.
[2] at RT.

which is a general form of the Hooke's law ($F = -Cu$). The tensor C has $3 \times 3 \times 3 \times 3 = 81$ components. However, due to the symmetrical form of σ_{ij} and ε_{ij}, each of them has 6 independent components and, therefore, we need only 36 elastic constants. In a cubic system, such as our four crystals, there are only three independent elastic constants, namely C_{11}, C_{12} and C_{44}. These correspond to Young's modulus (C_{11}), transverse expansion (C_{12}) and shear modulus (C_{44}), respectively. One can deduce them from the phonon dispersion curves $\omega(q)$, depending on the propagation direction, by using the following expression

$$V = \sqrt{\frac{C_{eff}}{\rho}} \tag{3.2}$$

where C_{eff} is an effective elastic constant, given for cubic crystals as indicated in Table 3.2. Fig. 3.2.a and 3.2.b specifically show the sound velocities of the (002) TA and LA acoustic phonons, respectively, which respectively yield C_{44} and C_{11} in a rather direct way ($C = \rho v^2$). Knowing C_{44} and C_{11}, it is possible to determine C_{12}, by measuring either LA phonons at the (110) position [$\frac{1}{2}(\mathrm{C}_{11} + \mathrm{C}_{12} + 2\mathrm{C}_{44})$] or TA phonons at (111) [$\frac{1}{3}(\mathrm{C}_{11} - \mathrm{C}_{12} + \mathrm{C}_{44})$]. These are shown in Fig. 3.1.c,f,i and 3.1.l, and the corresponding dispersion curves in Fig. 3.2.c. Changing the diffraction plane from [110][001], to *e.g.* [100][010], one can then access the T_2 mode while measuring TA phonons at the (110) Bragg reflection. We have done this only in FAPB (see supplementary Fig. B1, Appendix B). A summary of the determined sound velocities by INS for all four HOP compounds and the extracted elastic constants is given in Tables 3.1 and 3.3, respectively.

Considering the obtained elastic constants, one can also calculate the bulk mod-

Mode	q‖[100]	q‖[110]	q‖[111]
L	C_{11}	$1/2(C_{11}+C_{12}+2C_{44})$	$1/3(C_{11}+2C_{12}+4C_{44})$
T_1	C_{44}	C_{44}	$1/3(C_{11}-C_{12}+C_{44})$
T_2	C_{44}	$1/2(C_{11}-C_{12})$	$1/3(C_{11}-C_{12}+C_{44})$

Table 3.2: Effective elastic constant C_{eff}, given for cubic systems, depending on the propagation direction.

ulus [137]

$$K = \frac{1}{3}(C_{11} + 2C_{12}) \tag{3.3}$$

the Zener anisotropy index [138]

$$A = \frac{2C_{44}}{C_{11} - C_{12}} \tag{3.4}$$

and longitudinal/transverse (L/T) ratio for all systems. In MAPB and MAPI, the sound velocities or bulk modulus recently obtained from high-resolution inelastic X-ray scattering measurements [84, 139], although with less accuracy, agree with our findings.

Immediately we note that C_{12} in FAPI is negative, however this still fulfils the necessary Born elastic stability criteria, mentioned in section 1.3.1, for cubic systems [140, 141]:

$$C_{11} - C_{12} > 0 \ ; \ C_{11} + 2C_{12} > 0 \ ; \ C_{44} > 0 \tag{3.5}$$

A negative C_{12} simply implies that a cubic material, when uniaxially compressed along a [100] direction, will contract in the other two directions ([010] and [001]) and in that way, try to maintain an isotropic structure. However, we originally determined a value of $C_{12} = -5.7 \pm 3.6$ GPa. The problem here was that upon calculating the associated bulk modulus, we had a range of impossible, non-physical values, resulting from the relative standard error. Therefore, we proceeded to eliminate the non-physical range of values to arrive at $C_{12} = -4.3 \pm 2.2$ GPa, by considering extreme values of C_{11} and C_{44} within their error and cross check it with the physically acceptable range of values for C_{12}. Nonetheless, the negative C_{12} together with the very low bulk modulus, confirms the very unstable nature of α-FAPI (whose metastable single crystals last less than a week in the α phase [74]) and why it has actually been paired with MA, Rb and Cs for better performing photovoltaic devices. As shown in Table 3.3, the four perovskite compounds exhibit an overall

sizeable elastic anisotropic nature (A≠1), which can be mostly attributed to the very low shear modulus C_{44}. MAPI stands out with its relatively higher (around double) C_{44} which results in a discrepant, although still anisotropic, Zener index. However, it should be noted that the measurements were performed at 340 K, just above the transition to the cubic phase [72], resulting in an additional anharmonic effect. The remarkably low shear moduli are much more obvious when compared to the ones of classical semiconducting photovoltaic materials such as Si, GaAs or AlAs, where the elastic constants are on the order of 10^2 GPa [142]. It is believed that the rotation/tilts of the corner sharing PbX_6 octahedra [143] could be responsible for the particularly low shear modulus and large anisotropy in HOPs.

As evidenced in Fig. 3.3, C_{11} and K decrease noticeably with increasing lattice constant. These two quantities are, therefore, lower in iodide-based systems compared with bromide ones, especially in FAPI where they are a third of its bromide counterpart. This indicates a structural instability when the lattice parameter exceeds ∼6.4 Å. The relatively higher bulk modulus in MA-based compounds should be related to a steric effect, where the more symmetric and rotating MA molecules lead to more compact structures, which in turn results in larger binding elastic interactions. It is worth emphasizing that, by construction, the acoustic branches are defining the lowest ZB phonons and thus, related to the lowest peaks of the phonon density of states. That also implies that the Debye temperature is very small (*i.e.* about 30 K). Moreover, as a function of lattice constant, this quantity exhibits the same trend as for C_{11} and the bulk modulus. The observation that iodide materials are softer than bromide materials, as well as FA-based compounds versus MA-based ones is consistent with recent static nano-indentation measurements of the Young modulus [144, 145], though FAPI was not explored there (see Table 3.1 for comparison). In contrast, recent pulse-echo ultrasonic measurements at low frequency (10 MHz) and in the 140 - 350 K temperature range [10], show larger sound veloci-

Table 3.3: Summary of the elastic properties at RT for MAPB, FAPB and FAPI and at 340 K for MAPI, as measured INS and BLS.

	MAPB		FAPB		MAPI		FAPI	
Elastic Constant	INS	BS	INS	BS	INS	BS	INS	BS
C_{11}[GPa]	34.5±1.2	32.2±0.2	27.7±1.6	31.2±0.2	21.8±1.3	n/a	11.1±2.0	n/a
C_{44}[GPa]	4.1±0.2	3.4±0.1	3.1±0.1	1.5±0.1	7.3±0.3	n/a	2.7±0.3	n/a
C_{12}[GPa]	18.5±2.0	9.1±0.8	11.5±2.4	9.4±0.5	11.3±3.1	n/a	-4.3±2.2	n/a
Bulk modulus [GPa]	23.9±1.3	16.8±0.1	16.9±1.7	16.7±0.3	14.8±1.7	n/a	0.0±2.4	n/a
Anisotropy, A	0.52±0.005	0.29±0.01	0.38±0.03	0.14±0.01	1.38±0.22	n/a	0.4±0.2	n/a
L/T ratio	8.7±0.5	9.5±0.3	8.9±0.7	20.8±1.4	3.0±0.2	n/a	4.3±0.9	n/a

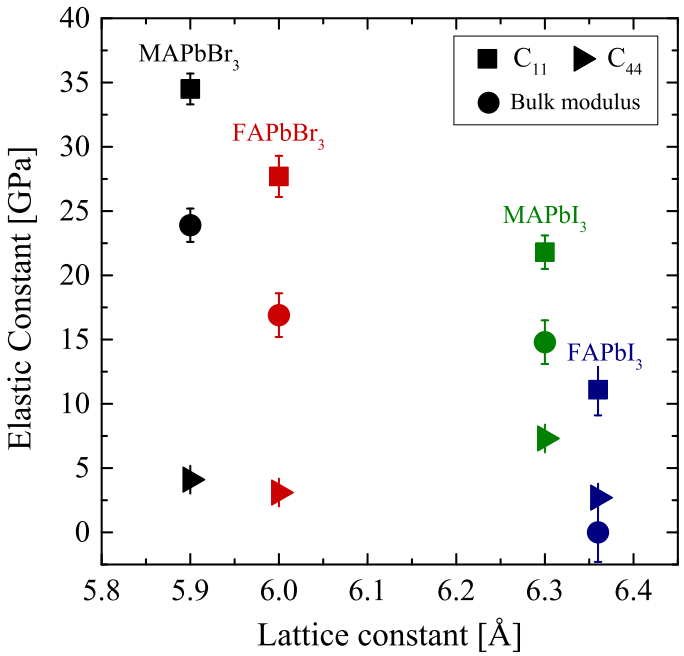

Figure 3.3: Elastic constants C_{11} and C_{44} as well as the bulk modulus K behaviour as a function of the cubic lattice constant of each compound.

ties for MAPI than for MAPB. However, the results of Anusca *et al.* [10] are also in disagreement with other ultrasonic studies [146, 147]. Yet it should be noted that the sound velocity attenuation is very large at 10 MHz and strongly affected by the structural phase transitions.

BLS on the other hand, allows exploring the same properties in the GHz range, intermediate between ultrasonic and neutron scattering measurements. Sound velocities were measured in both bromides compounds at RT using BLS, with a set-up in the [100][010] plane [146]. Five different incidence angles between the normal (0°) and the Brewster angle (25°) are reported in Fig. 3.4.a with the observation of quasi longitudinal and quasi TA modes. A measurement along the cubic diagonal [110] is also shown. For both bromide compounds, a good agreement between INS and BLS longitudinal sound velocities is observed (see Table 3.1). The same applies for the transverse mode in MAPB [146], within a 5% difference. In contrast, a 30% difference is observed for the same mode in FAPB. This is emphasized in Fig. 3.4.b where the sound velocity is presented as a function of q. One can clearly observe the phonon softening of the transverse mode at lower q, in the BLS regime, which indicates a tendency towards a ferroelastic phase transition [148]. Recording that this specific sound velocity is related to the C_{44} elastic constant as $C_{44} = \rho v^2$ (where $\rho = 4087$ kg/cm^3 is the density of FAPB), it means that a 30% softening of the sound velocity corresponds to a 60% re-normalization of C_{44}. Interestingly, the values obtained by laser ultrasonics [147], where a set of elastic constants was

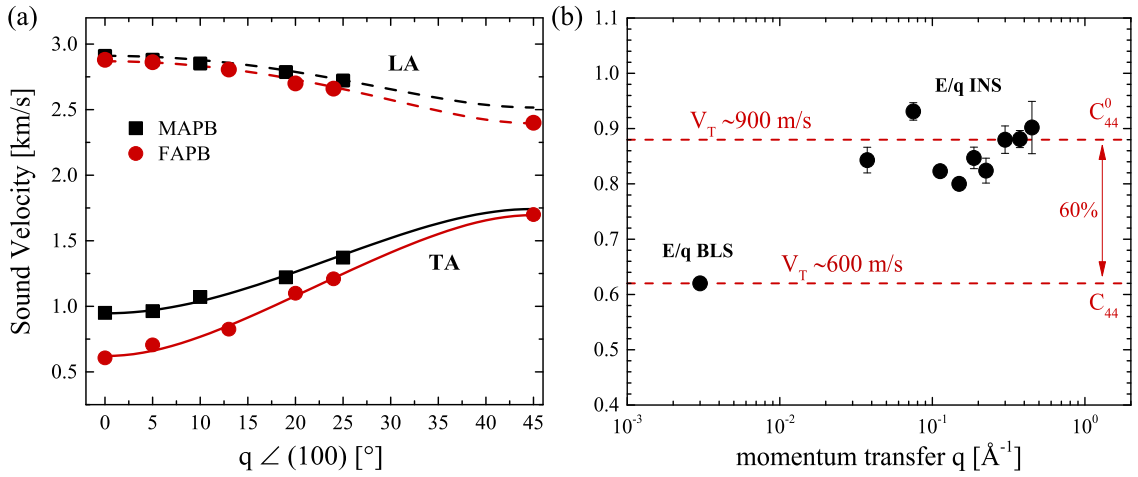

Figure 3.4: (a) Sound velocity diagram for FAPB and MAPB, as determined by BLS. The velocity is given as a function of the angle between the direction of measurement and the [100] direction. (b) Softening of C_{44} in FAPB as function of q, comparing phonon velocity as measured from BS and INS. The bare elastic constant, C^0_{44}, represents the elastic properties without the influence of the (incipient) phase transition. Note that the q scale is logarithmic to underline the broad q-range covered by both experimental techniques.

also given for MAPB, are in good agreement with our BLS results and a similar softening of C_{44} is observed too.

3.3 Discussion

HOPs are characterized by high electron/hole free charge carrier mobility at RT. At high temperature ranges such as RT (10 times the Debye temperature), the electronic mobility, μ, is typically governed by phonon scattering, via electron-phonon coupling (Fröhlich phonon emission). The whole phonon spectrum will then contribute to the electronic scattering rate, $1/\tau$ (μ is proportional to the electronic relaxation time τ). However, for intra-valley electron bands of direct gap semiconductors like the 3D HOP, the scattering rate should also be enhanced by collisions with low energy LA phonons. When the acoustic phonon contribution is considered, the electronic scattering time, τ, is expected to be proportionnal to the average squared longitudinal sound velocities [149], *i.e.* proportional to the average elastic constants such as C_{11} or the bulk modulus K that are shown in Fig. 3.3. The contributions to the carrier mobilities related to interactions with acoustic phonons are thus predicted to be strongly different between iodide- and bromide-based compounds, but such a large difference in carrier mobilities is not experimentally observed [3, 74]. Instead, it rather shows that the carrier mobilities are limited by other processes, namely interactions with optical phonons. Such conclusion is corroborated by emission line broadening results [120, 150], pointing to scattering from longitudinal optical (LO)

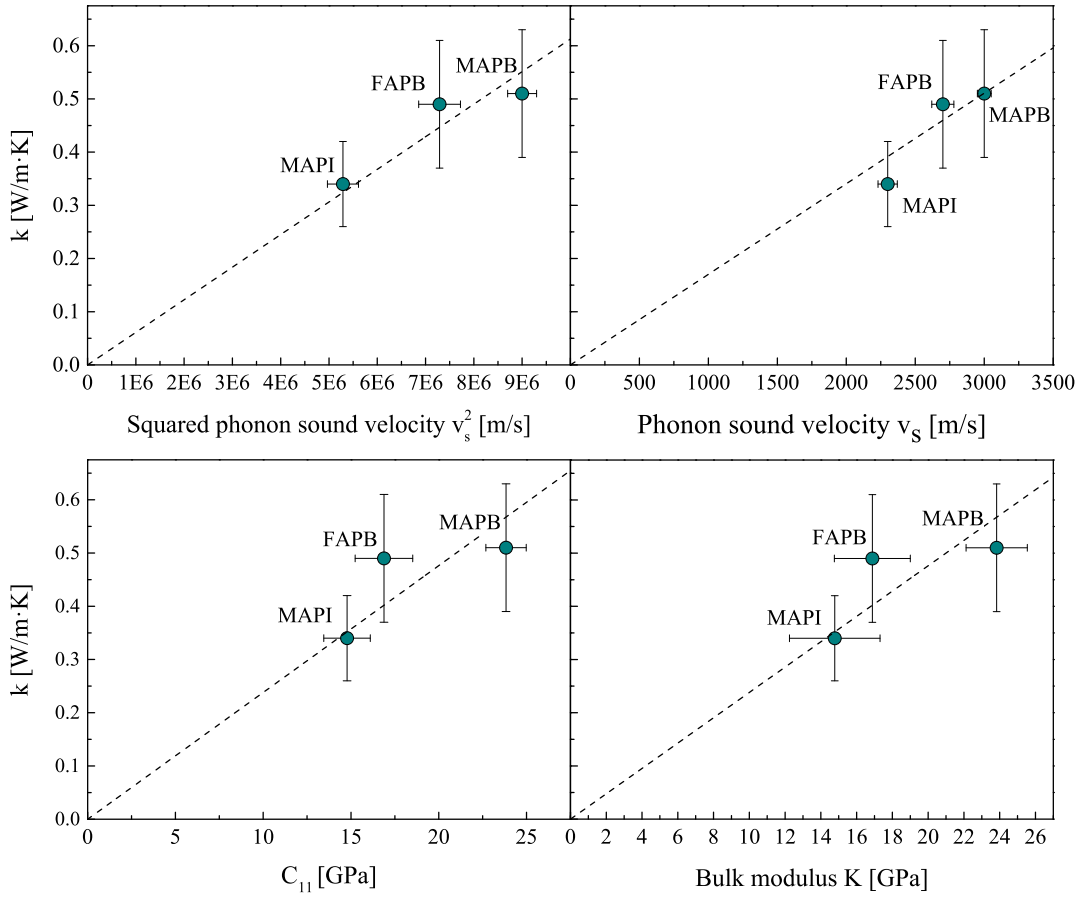

Figure 3.5: Thermal conductivity κ as a function of (a) longitudinal phonon sound speed $\mathbf{v}_{LA}$, (b) $\mathbf{v}_{LA}^2$, (c) C_{11} and (d) bulk modulus K. The dashed line is a linear fit intercepting at $y = 0$.

phonons, as the dominant source of electron-phonon coupling near RT. However, there are other implications to be considered.

Low thermal conductivity

A direct consequence of the lattice softness is the ultralow thermal conductivities reported in perovskites [151–153]. In any electric semiconductive or insulating material, thermal conductivity κ is directly affected by the phonon properties. More specifically, the kinetic theory of phonon transport yields [149, 151]

$$\kappa = \frac{1}{3} C_v v_s^2 \tau \tag{3.6}$$

where C_v, v_s and τ are the phonon specific heat, group velocity and the scattering rate. In fact, we took the κ values from the frequency-domain thermoreflectance (FDTR) data of Elbaz *et al.*[145] and plotted it as a function of the longitudinal sound speed $\mathbf{v}_{LA}$ (Fig. 3.5.a), $\mathbf{v}_{LA}^2$ (Fig. 3.5.b), C_{11}(Fig. 3.5.c) and the bulk modulus K (Fig. 3.5.d), that we measured and calculated. The approximate linear relation-

ship observed in general in Fig. 3.5 signifies that the $APbX_3$ perovskites have similar phonon mean free paths/scattering rates and that the differences in κ result mostly from variations in phonon group velocity (*i.e.* elastic constant). One can then associate lower thermal conductivity to lower elastic stiffness. As a result, although there FAPI is not featured in Fig. 3.5, the thermal conductivity of MAPB is predicted to be higher than FAPI due to the higher elastic moduli, *i.e.* a stronger acoustic phonon localization is expected in FAPI compared with MAPB.

Hot phonon bottleneck

In lead halide perovskites it has also been reported a significant hot-phonon bottleneck effect in carrier thermalization [9, 154]. The effect consists in the up-conversion of acoustic phonons into optical modes, which recycles thermal (vibrational) energy, reheating charge carriers and prolonging the cooling period of the carrier-optical phonon system. This helps maintaining a hot carrier population, something that is vital to achieve hot carrier photovoltaic devices and break the Shockley-Queisser limit [85]. Yang *et al.* [9] proposed phonon bottleneck and up-conversion process is illustrated in Fig. 3.6.a.

1. First, the Fröhlich interaction occurs predominantly between the hot carriers and inorganic sub-lattice, exciting the high-energy lead-halide LO phonons;
2. Decay of LO phonons to acoustic modes (and local lattice heating). During this stage, the co-vibration between organic and inorganic sub-lattices can also be excited via phonon–phonon scattering;
3. Propagation of acoustic phonons is blocked by anharmonic phonon–phonon scatterings;
4. The up-transition probability of phonons is then increased, especially when organic cations appear in the lattice. The organic cation introduces lots of low-energy co-vibrational optical modes, which overlap well with acoustic branches and facilitate the phonon up-transition;
5. The recycled thermal (vibrational) energy reheats charge carriers and prolongs the overall cooling period of carrier-phonon system.

A strong anharmonic phonon–phonon scattering corresponding to a low thermal conductivity in general can localize acoustic phonons by blocking their propagation and increase the probability of an up-transition. In turn, an efficient up-conversion of acoustic phonon can also impede thermal propagation in the lattice [155].

At the same time, ultrafast transient absorption measurements reveal two stages of the carrier cooling process [9]. These have been highlighted in Fig. 3.6. The first one is related to the intrinsic Fröhlich phonon emission mentioned above and does

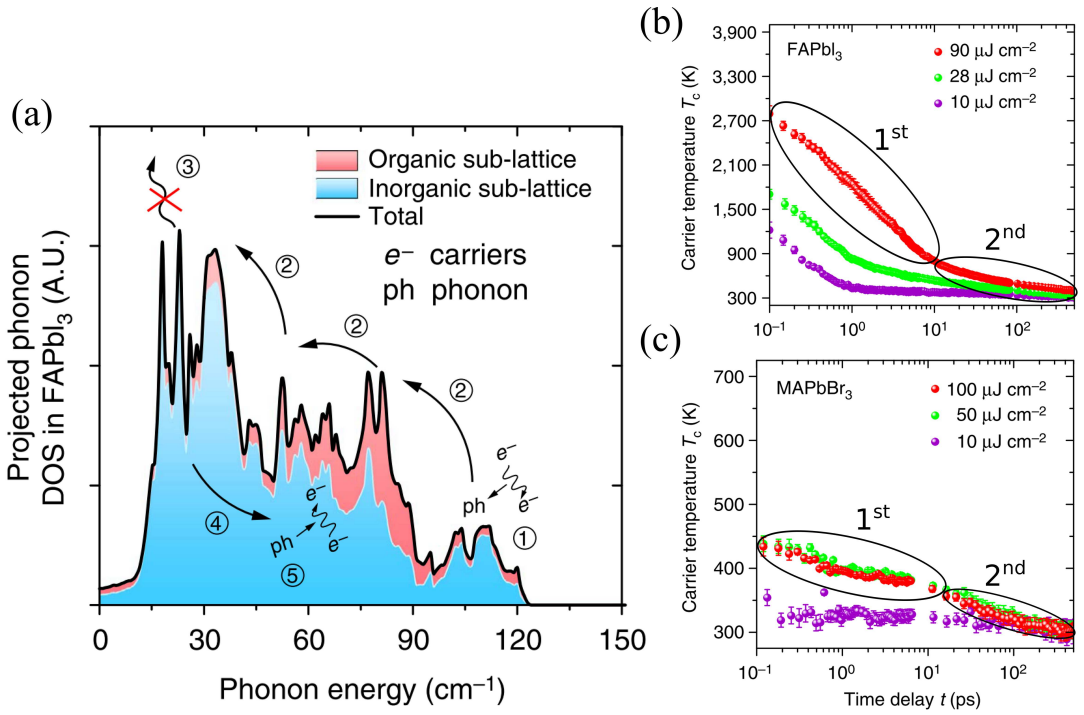

Figure 3.6: (a) Proposed phonon dynamics of the bottleneck effect in FAPI. The solid black line shows the total phonon DOS, in which the contributions from the inorganic and organic sub-lattices are shown by the blue region on the bottom with the pink region stacked on top, respectively. The labelled phonon dynamic process are: (1) Fröhlich interaction of carriers primarily on the lead-halide framework; (2) relaxation of lead-halide LO phonon, organic sub-lattice can be excited by phonon–phonon scattering; (3) propagation of acoustic phonon is blocked due to anharmonic phonon–phonon scatterings; (4) up-conversion of acoustic phonons; and (5) carrier reheating. Time-dependent carrier temperature under different incident fluence, in (b) FAPI and (c) MAPB. We have circled the two cooling stages of the carrier-phonon system mentioned in the text. Reprinted from [9].

not vary significantly among the various different perovskites. On the other hand, in the second cooling stage, hot carrier-phonon dynamics occur, corresponding to the phonon bottleneck effect [9, 154]. The four HOP materials studied in the present work show, in fact, very different acoustic phonon densities of states that might affect hot phonon energy relaxations. At RT, the carrier-phonon relaxation rate of that second cooling stage is typically 3-4 times slower in FAPI, compared with the MAPB system [9]. This is fully consistent with the difference in elastic constants reported in Fig. 3.3. This apparent correlation between C_{11} and carrier relaxation rates, together with the above observations regarding thermal conduction, suggest lower elastic stiffness to be, therefore, an important factor to enhance the hot carrier effect in hybrid perovskites.

In conclusion, our quantitative study of low energy acoustic phonons provides a complete set of elastic constants of four of the more technologically relevant hybrid perovskites, in their cubic phases. We highlight the overall very low shear modulus

C_{44} and the significant variation of elastic bulk modulus among them. This way we give a clear picture of the difference in softness between FA and MA based compounds, as well as Br^- vs. I^-, and how it relates to their structural stability and ultralow thermal conductivities. Moreover, the data presented here strongly supports the hypothesis of the hot phonon bottleneck phenomena, reported by other authors to explain hot carriers relaxations. Both processes are expected to be enhanced by low elastic stiffness, especially in the case of the ultrasoft FAPI.

Chapter 4

Direct evidence of weakly dispersed optical phonons at low temperature

Here, we investigate the low temperature optical phonon spectrum below 40 meV - via inelastic neutron scattering and Raman spectroscopy - in single crystals of four different hybrid lead halide perovskites: $MAPbBr_3$, $FAPbBr_3$, $MAPbI_3$, and α-$FAPbI_3$. The spectra reveal weakly dispersive optical phonons, at energies as low as 2-5 meV, which seem to be the origin of the limit of the charge carrier mobilities in these materials.

4.1 Introduction

We have seen in the previous chapter that, carrier scattering is dominated by Fröhlich coupling between charge-carriers and LO phonon modes, rather than with acoustic phonons at RT [120, 121], which was reinforced by our analysis of elastic constants. It has also been stressed in the introduction (section 1.4.2) that this goes against the apparent acoustic-like temperature dependence of mobilities in HOPs. As a result, the absence of a clear picture remains, with regards to the phonon scattering mechanism setting the limit of charge-carrier mobility. Furthermore, it was also made evident the importance of the coupling between acoustic and optical phonons in the hot-phonon bottleneck effect. However, atomic-level description of these materials is hindered by the hybridized nature of phonon excitations in the organic and inorganic sub-lattices, which interact with each other via hydrogen bonding. Therefore, a direct measurement of optical phonons branches with the same methodology as for the acoustic modes, becomes a necessary step to address carrier-phonon coupling dynamics and to assess the fundamental intrinsic limit to the mobility of charge carriers in these materials.

In this chapter, we then proceed to employ both neutron ToF and TAS techniques to investigate the same four hybrid perovskite single crystals. Complementary Raman scattering spectroscopy is also used. INS allows for direct measurement of the optical phonon spectrum over the reciprocal space that covers the full Brillouin zone (BZ), thus offering the most complete approach. Raman spectroscopy is also a very powerful and precise technique to measure optical phonons and quasielastic contributions, but restricted to the center of the BZ (Γ-point) and limited by specific selection rules.

In our low temperature measurements, we are able to observe well-defined optical phonons. Mode attribution of the latter to the respective structural vibrations has been carefully discussed and a comparison is made between the four compounds. We also find the optical excitations to be non-propagating as they show little to no dispersion in momentum space (particularly in MA-based compounds), suggesting a localized character in real space.

4.2 Results

4.2.1 Lack of dispersion in momentum space

Due to the complicated interplay between organic and inorganic sub-lattices, where molecules perform stochastic motions at ambient temperature [156], it makes more

sense to start with low temperature measurements. At the most ordered structural phase of the HOPs, the orthorhombic one, the organic molecules are frozen in place and overall motions are reduced, presenting a more ideal condition to probe their lattice dynamics.

Indeed, at 5 K, neutron spectra show well-defined energy resolution-limited phonon features (Figures 4.1 and 4.2). With ToF, the dynamic structure factor $S(q, E)$ in MAPI was obtained by varying the incident energy of neutrons in the direction of [ζ,ζ,2] (*i.e.* [$hk0$]). For the scattering conditions, having an incident neutron wavelength of $\lambda = 2$Å ($\equiv 3.14$ Å^{-1}), we were limited to a range of 15 meV. Within this energy range, we observe three different modes. Interestingly, all optical phonon modes (or mode bundles) seem to have little to no dispersion. The observation of dispersionless phonon is opposed to what has been previously predicted using density functional perturbation theory in MA-based HOP [52, 139], where dispersive phonon branches were computed. We then performed TAS measurements also at 5 K, in all four perovskites. These were constant-Q scans along high symmetry directions ($\mathbf{\Gamma} \rightarrow \mathbf{M}$ or $\mathbf{\Gamma} \rightarrow \mathbf{R}$). Likewise, these show no dispersion, within a 0.1 meV error, and only the amplitudes of the modes vary (Fig. 4.2). However, we need to temperate this observation, due to the question of incoherent scattering from hydrogen atoms.

As pointed out in the introduction to neutron theory (section 2.2), the neutron intensities correspond to the sum of coherent and incoherent cross-sections (Eq. 2.21). The coherent cross section corresponds to the correlations of atomic displacements of all nuclei at different times whereas the incoherent cross section represents self-correlations only at different times of the same nucleus. The latter includes interference effects which are absent in the incoherent scattering. All nuclei are characterized by two different neutron scattering lengths, b_{coh} and b_{inc}. The value of b_{coh} of nuclei present in our HOPs is ranging between 9.4 fm for Pb, to 5.28 fm for I. The incoherent scattering length of hydrogen, $b_{inc} = 25.27fm$, is much larger than the ones of all other atoms (Pb, I, Br, C ,N) present here ($b_{inc} \leq 2fm$). Therefore, as it is well-known for organic compounds, the incoherent cross section is mostly controlled by the hydrogen contribution. We also remind that the MA, CH_3NH_3, and FA, $(CH_2)_2NH$, molecules in our samples were protonated, giving rise to a large incoherent neutron scattering from the 6 hydrogen atoms in MA (or 5 in FA), per formula unit of the HOP compounds.

We showed that the coherent cross section can be separated in two terms: a dynamic structure factor, H($\mathbf{Q}$), and an energy dependent spectral weight function, $S_j(\mathbf{q}, \omega)$, corresponding to Equations 2.32 and 2.34, respectively. In the structure

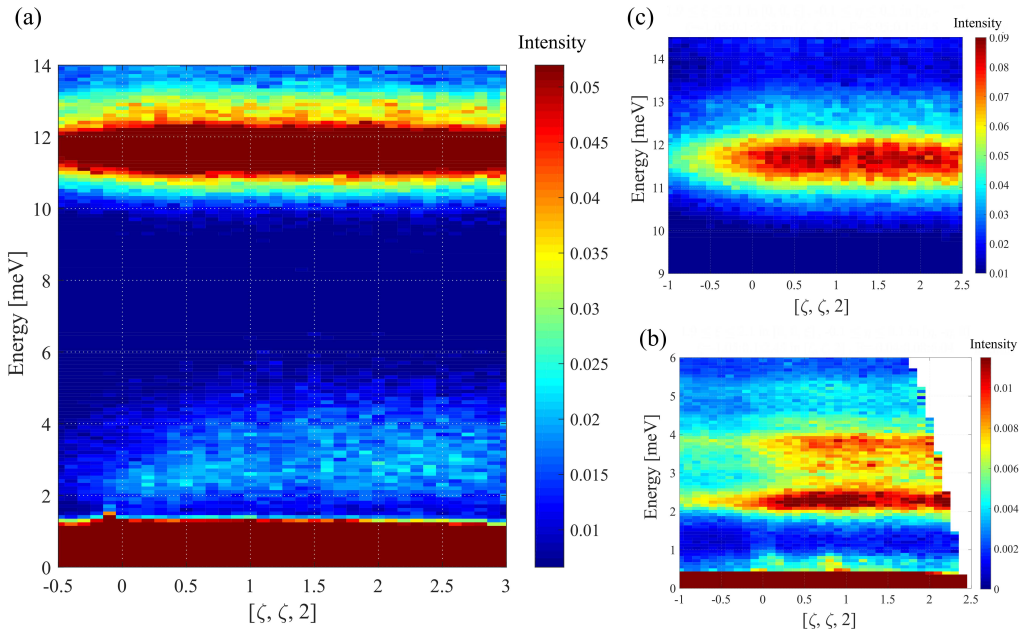

Figure 4.1: **(a)** Full ToF contour plot of $MAPbI_3$, at 5 K, and zoomed in plots at **(b)** low (below 6 meV) and **(c)** high (10-14 meV) energy range.

factor, **d**, b^d_{coh}, M_d and ξ_d are respectively the position of the d-th atom in the unit cell, the scattering length, the molar atomic mass and the polarization vector for the j-th phonon of the atom labelled d within the unit cell. $W_d(\mathbf{Q})$ is the Debye-Waller factor of d-th atom in the unit cell. V_0 is the volume of the unit cell of the crystal. Conversely, though still within the harmonic approximation, the incoherent cross section was defined in Eq. 2.35, where last section corresponds to a phonon density of states (sum in momentum space of phonon modes). In contrast to the coherent cross section, the specific **q** dependence of the j-th atom is lost. In principle, no information can therefore be obtained for the phonon dispersion from the incoherent cross section, which, typically, has the shape of a broad continuum if the optical phonons are dispersive (examples of such situations are multiple in the literature [126]). However, it exhibits sharp features in case of dispersionless optical phonons. We are facing this last situation in our HOPs, especially for the MA-based compounds, where the low temperature phonon spectra show energy resolution-limited peaks.

Therefore, in case of incoherent scattering, the phonon momentum information is lost. Since the hydrogen atom has a large incoherent scattering length b^H_{inc}, the phonon peaks involving hydrogen will basically correspond to the incoherent cross-section. In contrast, the phonon peaks from the PbX_3 cage will correspond to coherent cross-section and those amount to the lowest energy bundle a (as discussed below), showing no dispersion (see *e.g.* the ToF data in MAPI, Fig. 4.3.b).

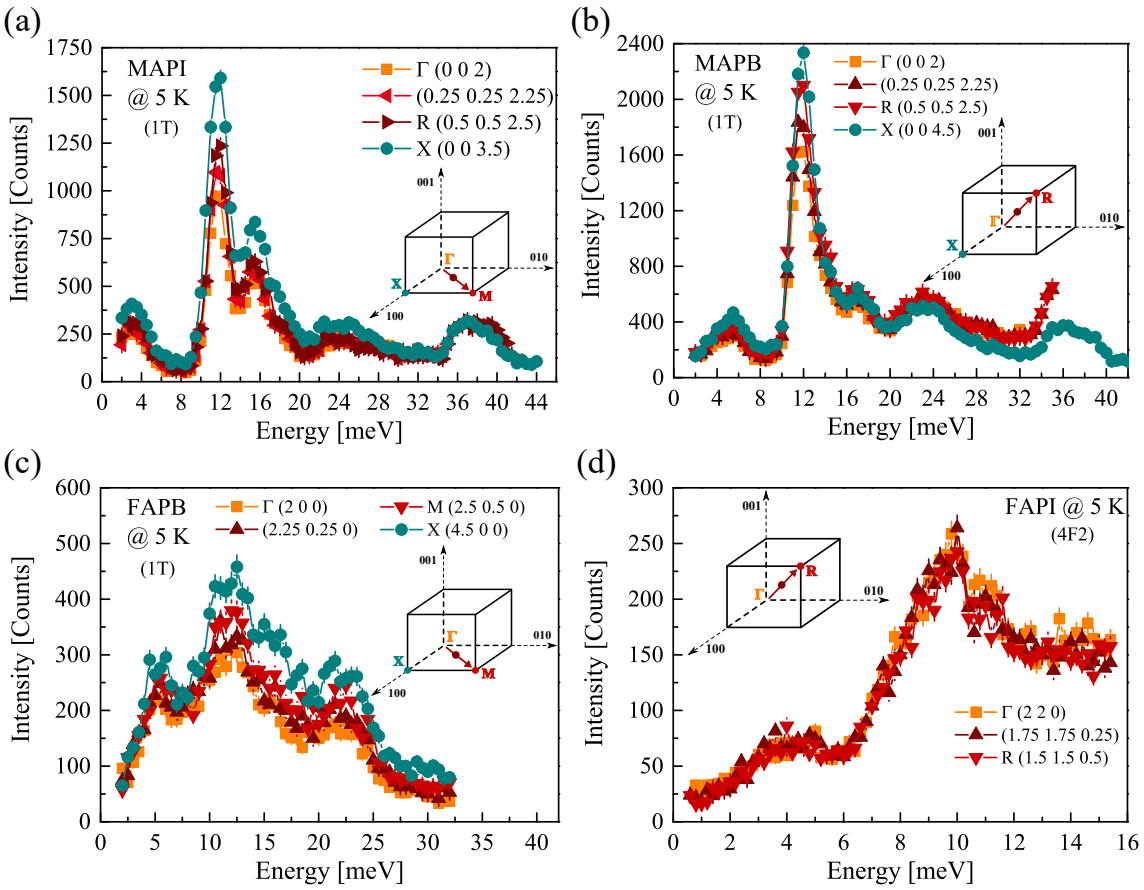

Figure 4.2: At 5 K, TAS measurements along high symmetry directions, going through a BZ, in **(a)** MAPB, (b) MAPI, (c) FAPB and (e) FAPI. The insets of each show the correspondent measurement trajectories in momentum space.

Further, even for incoherent scattering, some information can be obtained from the sharpness of the measured peaks. Energy resolution-limited peaks, as we observed for MA-based HOPs, can only be accounted for by dispersionless phonons even for incoherent scattering. It is interesting to compare our data with the neutron scattering studies of HOP powder samples where the **q** dependence is also lost by averaging over all orientational directions. We notice that the powder sample spectrum of MAPB [136] and MAPI [157] exhibit as well sharp phonon modes at the same energy than ours, suggesting as well the dispersionless nature of these phonon modes. Further, the lowest energy mode at 5 meV in MAPB does not change in position when comparing a deuterated sample to a protonated one [136], showing that it is not related to a molecular vibration. The lowest energy mode is then necessarily associated to the coherent neutron cross section as the incoherent neutron cross section is predominantly dominated by hydrogen vibration. Neutron powder sample spectrum observed in $MAPbCl_3$[157] exhibits no sharp features, which is indicative of phonon dispersion, in clear contrast with MAPI. However, the obser-

vation of broader phonons modes in FA-based HPO (see below) may question the dispersionless nature in FAPB and FAPI (for instance for the modes above ∼7 meV in Fig. 4.3.e-g involving molecular vibrations). The origin of broader phonon peaks can be either due to a larger damping or related to moderately dispersive phonons in FA-based HOPs. It is worth to emphasize that this lack of dispersion concerns both LO and transverse optical (TO) phonons. Finally, Figures 4.1 and 4.2 show as well that each optical phonon mode can be defined by almost the same energy for any Q-point of the BZ.

4.2.2 Low temperature INS spectra

Systematic low temperature INS experiments were performed with medium and high energy resolutions, from, respectively, thermal and cold beams. The difference in neutron energies and experimental conditions will have an impact on the energy resolution of the INS measurements (section 2.4.2).
Being in the orthorhombic phase (possibly trigonal for FAPI), each compound has undergone structural distortions (octahedral tilting and ordering of organic molecules), giving rise to atomic superstructures at either or both the M and R point. For that reason, we have focused on these two Bragg reflections, the spectra of which, as we have just seen, has no noticeable difference[1]. We therefore report the phonon spectrum at the R point $(1/2, 1/2, 3/2)$ for most compounds except for FAPB where it is shown at the M point $(5/2, 1/2, 0)$.

The specific (h, k, l) coordinates of the M and R points are chosen taking into account the scattering intensity of each reciprocal point, which is affected by the dynamical structure factor. As exemplified in the neutron scattering study of CsPbCl of Y. Fuji [158], the structure factor will be essentially zero for R and M points with $h = k = l$ or $h = k$, respectively. On the other hand, they will typically be maximized for $\frac{1}{2}(h, h, h + 2)$ (R point), where $h = 1,\ 3$ and $\frac{1}{2}(h, h - 2, 0)$ (M point), where $h = 3,\ 5$. Besides, it is not possible to access both points, for a single specific scattering plane configuration. We also have to keep in mind the experimental logistics at the spectrometer. There are points in reciprocal space that are problematic to reach due to the physical space constraints of the equipment, meaning that components of the spectrometer could collide with one another depending on the sequence of points to be measured.

The obtained optical phonon spectra for all four compounds are presented in Fig. 4.3. As already stated, a series of prominent optical phonon modes (or "bundles" of modes) are observed at different energy ranges. We utilize here the expres-

[1] Related to the lack of dispersion of the phonon modes; see also supplementary Fig. B2.

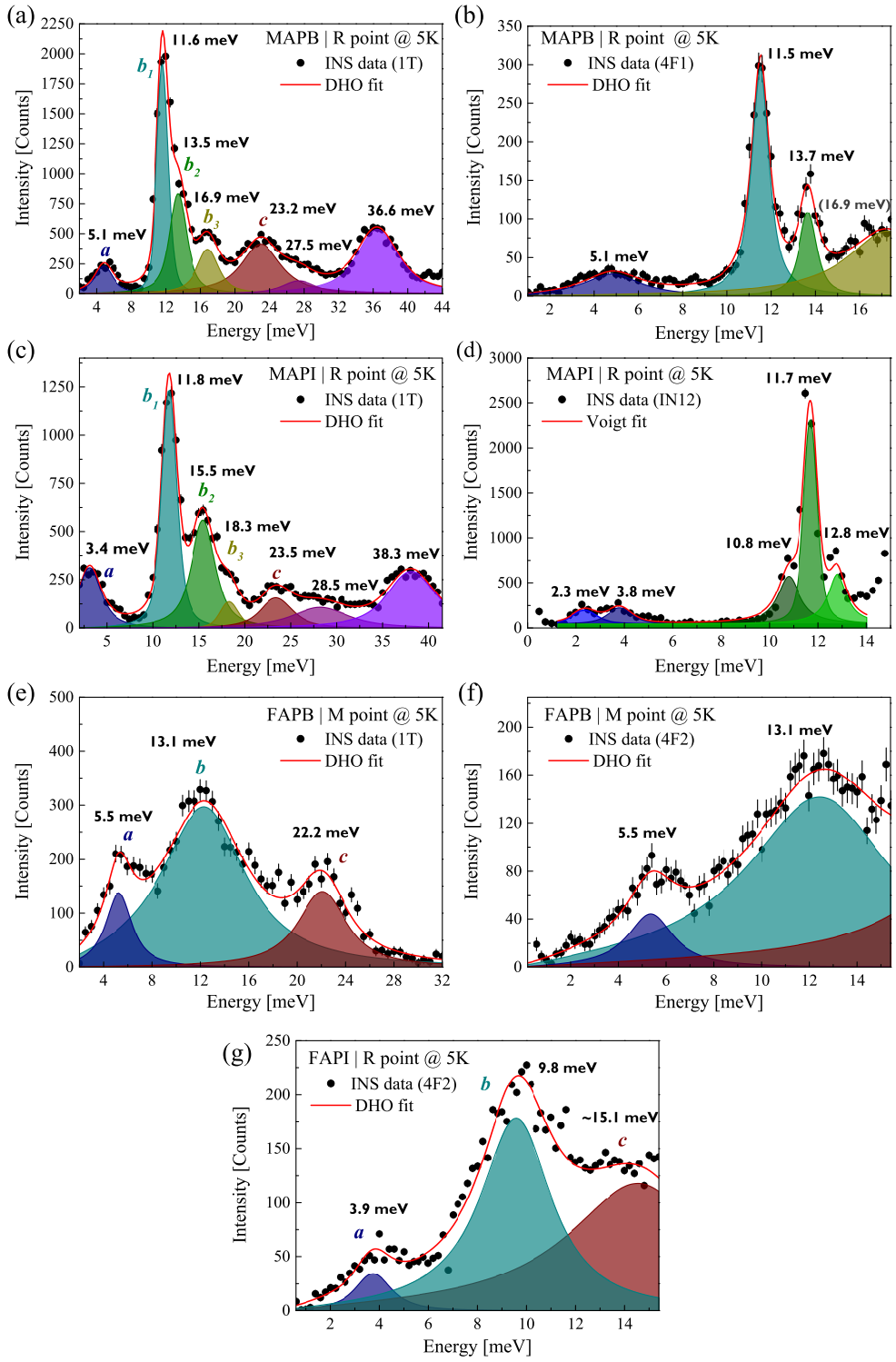

Figure 4.3: INS spectra measured at 5 K, at the R Bragg reflection $(1/2, 1/2, 3/2)$ of **(a,b)** MAPB, **(c,d)** MAPI and **(g)** FAPI and **(e,f)** at the M point $(5/2, 1/2, 0)$ of FAPB. For each system, we show in each row the measurements using a thermal (left) and a cold source (right), with the exception of FAPI. The experimental INS data (black scatter points) is fitted (red line) with a sum of DHOs (Eq. 2.38) and is presented with a removed background. Individual fitted peaks are labelled (filled coloured area).

Table 4.1: Energies of the optical phonon modes measured at 5 K by INS and 20 K by RS. Phonon lines (or bundles of modes for INS) are fitted by a DHO. Energies are given in meV.

	MAPB		MAPI	FAPB	FAPI
Energy	INS	Raman	INS	INS	INS
Low	5.1	4.1, 4.8, 5.1, 5.5	2.3	5.5	3.9
<10 meV		5.9, 7.2, 8.4, 8.9	3.8		
Medium	11.6 , 13.5	11.9, 12.6, 13.5	10.8, 11.7, 12.8	13.1	9.8
10-20 meV	16.9	16.3, 17.3, 18.3	15.5, 18.3		∼15.1
High	23.2, 27.5	21.8	23.5, 28.5	22.2	
>20meV	36.6	40.8	38.3		

sion of bundles since some of these features, as we will see, are a superimposition of two or more phonon modes. To describe the neutron spectra, we use again the DHO model of Eq. 2.38, where only a DHO for each phonon mode and a constant background were necessary (no quasi-elastic signal). The obtained phonon energies are summarized in Table 4.1.

For a first analysis, we define three energy ranges where the different optical modes are located. We have labelled them arbitrarily as low (2-10 meV), medium (10-20 meV) and high (> 20 meV). More specifically, in MAPB we find a low-energy mode at 5 meV; an intense peak at 11.6 meV followed by two smaller shoulders at 13.5 and 16.9 meV; and relatively broader bands at 23.2, 27.2 and 36.6 meV (Fig. 4.3.a,b). These results match well with a previous INS experiment on a MAPB powder sample [136].

Similarly in MAPI, we obtained two low-energy modes located at 2.3 and 3.8 meV, an intense peak centered at 11.7 meV surrounded by two smaller shoulders at 10.8 and 12.8 meV. From one-dimensional cuts at $\zeta = 2$ (*i.e.* $Q = (002)$) of the ToF mapping in Fig. 4.1 (see Supplementary Fig. B3), there could be 4 or 5 bands in the 2-5 meV range and the feature around 12 meV may host up to 4 bands as well. These are followed by two bundles at 15.5 and 18.3 meV, and at higher energy range, other ones at 23.5, 28.5 and 38.3 meV (Fig. 4.3.c,d). Our MAPI spectra and the detected bands are directly comparable with previous INS studies of K. Druzbicki *et al.* [159] and B. Li *et al.* [160].

In FAPB we note a broader central feature dominating the medium energy range (Fig. 4.3.e,f), while, at the same time, identify three distinct bundles at 5.5, 13.1 and 22.2 meV. These results on FAPB are in line with the ones observed in MAPB, although much broader phonon bundles are systematically observed in FAPB, com-

pared to the more numerous (and narrower) modes that appear for MAPB. These two compounds share the same space group (Pnma) at low temperature although the static structural distortions characteristic of the orthorhombic phase are smaller in FAPB [73]. This may be connected to a different dynamics of the FA cation and its coupling to the perovskite lattice, by comparison to the MA cation (vide infra) [161].

Finally in FAPI - a problematic sample and, therefore, scarcely studied at such a low temperature in the literature - we could only perform measurements on the 4F2 cold neutron spectrometer (Fig. 4.3.g). Nevertheless, in the accessible energy range, we detect large optical phonons at 3.9, 9.8 and ∼15.1 meV. Photoluminescence (PL) studies on single CQDs [162] have identified exciton side-bands at 3.2, 7.8 and 15.4 meV, which match rather well with our TAS results on FAPI. The intermediate mode seemingly exhibits a slight discrepancy, but as reported in [162], it undergoes temporal fluctuations under high energy excitation, and is roughly spread between 7.5 and 12.5 meV. Again, our TAS results on FAPI show a significantly broad profile, as in FAPB.

According with nuclear magnetic resonance (NMR) measurements [163], the broader nature of the optical modes of FA-based compounds, compared to their MA-based counterparts, may be attributed to the fact that the FA reorientation in FA-containing materials is faster than that of MA in the MA-based perovskite, despite the fact that FA is larger than MA. This has an impact on the charge carrier lifetime in these compounds. In addition, the acoustic density of states is located at lower energy in FA-based compounds as compared to the MA-based [164], thus leading to enhanced scattering between acoustic and optical phonons and related increased anharmonicity.

The importance of phonon broadening is made even more clear by the comparison with Raman measurements. Raman scattering spectroscopy has been as well performed in the MAPB single crystal at low temperature. Fig. 4.4 shows side by side the low temperature (20 K) spectra of MAPB, from INS (on the thermal 1T) and Raman scattering. The Raman spectra is also fitted with a slightly modified version of the (DHO) model (Eq. 2.38), and the obtained modes have also been included in Table 4.1, results which agree with a previous Raman scattering report [165]). Raman spectra are recorded at very low q, whereas the INS experiments are measured at a Bragg peak position $\mathbf{Q} = (0, 0, 2)$, both are therefore probing optical phonons at the Γ point in the BZ. Contrary to INS, the modes below 10 meV in Raman scattering benefit from a favourable scattering efficiency as compared to those at higher energy. The energy positions of the optical phonon modes here identified

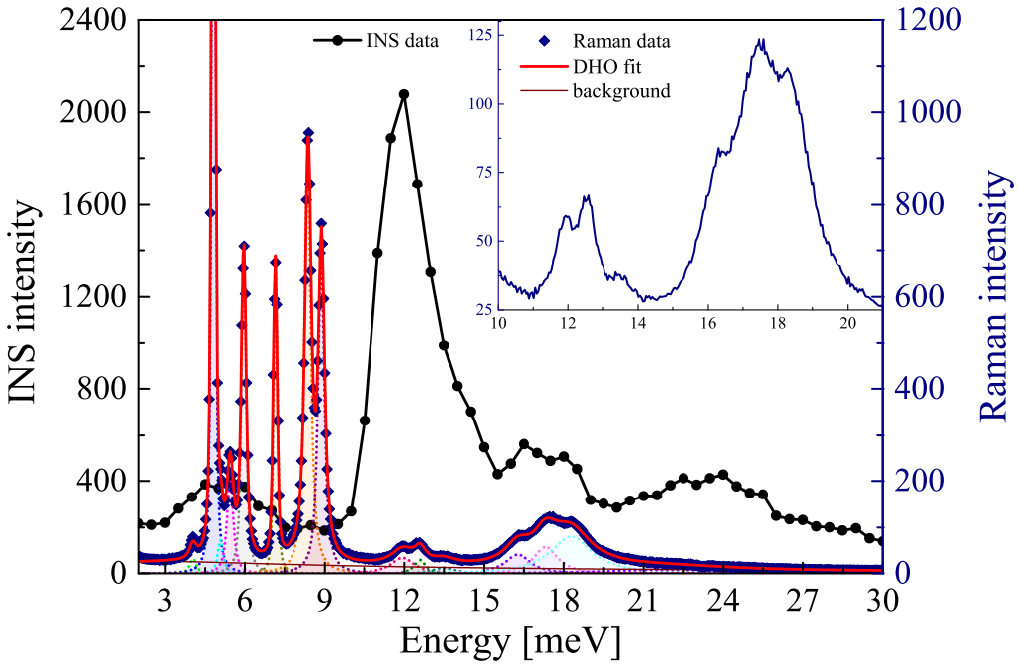

Figure 4.4: Comparison of the INS using the thermal beam instrument 1T at LLB (5 K) and Raman scattering (20 K) optical phonon spectra in MAPB, at the Γ point ($\equiv (0, 0, 2)$ Bragg position for INS). Inset shows a magnification of the Raman scattering spectra in the 10-20 meV range. The energy resolution of Raman scattering is here 0.125 meV compared to the energy resolution of ∼1-2 meV (over the scan energy range) for a thermal TAS.

from INS and Raman are consistent, especially the Raman mode bundles around 5 meV, 12 meV and 18 meV (inset). However, a few of the Raman modes around 9 meV do not appear clearly in INS[2]. This discrepancy may be attributed either to the different scattering factors of both techniques, or poorer INS energy resolution (0.125 meV of Raman vs. 0.2-0.5/1-2 meV at 4F/1T), hiding the mode fine structure. Mode broadening related to instrumental resolution will, therefore, be more important for neutron scattering than for Raman scattering.

Unfortunately, we do not have Raman measurements at low temperature for the other 3 compounds since the Raman study was focused on higher temperatures, around the tetragonal to cubic transition, which will be shown in the next chapter. It is clear nevertheless, from a qualitative comparison between the spectra from INS and Raman (ours and other from literature), on MA-based compounds, that with INS we are not detecting all modes. However, we should also note, that there is in fact, a number of predicted phonon modes from symmetry analysis [166], for the orthorhombic phase, which even with Raman have not been revealed.

Overall, one can then see a commonality between the different perovskite sys-

[2]Even a more generous fitting of the INS spectra (see supplementary Fig. B4), where we include more visible "bumps" from the spectra, only yields some of the modes from Raman - namely at 3.6, 4.7 5.9 7.4 and 8.5 meV.

tems. By cross-referencing our results with the above mentioned previous works and other literature on the subject, we can assign the identified features of the low temperature spectra to the respective vibrational modes. In recent lattice dynamics calculations, Ponce *et al.* [167], predict five modes for MAPI at 3, 4.3, 10.2, 14.4 and 21 meV. A-site displacement (*i.e.* rattling of the organic molecule within the cage) is said to be responsible for the peak at 10.2 meV, while scattering at 21 meV results from libration motions of the organic cations. On the other hand, the modes at 3, 4.3 and 14.4 meV are claimed to be related to the inorganic sub-lattice and arise from the rocking, bending and stretching motions of the PbI_3 network, respectively, the latter one involving hybridization with organic cation motions. The calculated modes match well with our measurements, the already mentioned INS studies [157, 159, 160] and the identifications made based on associated DFT calculations [159].

Regarding MAPB, one is compelled to draw parallel conclusions of those about MAPI. Besides, in the work by Swainson *et al.* [136] on MAPB, the 5 meV mode is again associated to vibrations of the PbX_3 network. Furthermore, their comparative study between non-deuterated and deuterated samples clearly evidenced the influence of the organic cation motions on the modes at 11.5 and 13.7 meV.

In the PL study on FAPI CQDs [162], the authors compare their study with the theoretical predictions and near-infrared spectroscopic measurements on MAPI [166] and, as a result, ascribe the observed side-bands to LO phonon modes related to bending (3.5 meV) and stretching (15 meV) motion of the PbI_3 cage and to rigid-body motions of FA cations (11 meV). All these data point towards the participation of molecular vibrations in the low energy modes of the hybrid perovskites.

As it pertains to the mode at $\sim$37 meV, there is a consensus that it originates from organic molecular vibrations [159, 168, 169], although there is a debate about the exact nature of the involved atomic motions. Park *et al.* [168] describe MA vibrations involving MA wagging, MA rotation and MA-MA stretch. Quarti *et al.* [169] as well as Drùzbicki *et al.* [159], suggest a torsional MA vibration (also called disrotatory vibrations) that involves the terminal NH_3 and CH_3 moieties, which is also in line with the vibrational mode found near 300 cm^{-1} (*i.e.* 37.2 meV) in isolated MA calculations [169, 170].

4.3 Discussion

The low temperature INS (and Raman) optical phonon spectra in our four HOP single crystals, reveal a number of characteristic features down to very low energy.

We have identified three different energy ranges in the spectra and gathered the modes or bundles of modes for each compound in three categories (a, b and c), as can be seen in Fig. 4.3. From our experimental data and based on earlier literature, the following conclusions are drawn. Modes in the low-energy range (below 10 meV) are associated with vibrations of the PbX_3 network, mainly rocking and bending. As for the intermediate energy range, between 10 and 20 meV, a series of mutually coupled modes are observed which arise from both the organic and inorganic sub-lattices and, therefore, show a highly hybridized nature. Here, a prominent feature is the stretching of Pb-X_3, which is predicted to be coupled with the organic sub-lattice. Also, a mode related to the A-site displacement, is identified at least in MAPI. Additional evidence of this coupling comes from the comparison between non-deuterated and deuterated samples [136]. This further corroborates the increased broadening observed in FA-based systems, especially in this medium energy range. This enhanced broadening is consistent with the difference in the dynamics of the FA and MA cations previously reported by NMR [163], and molecular dynamics simulations [161]. It has also been shown by PL studies that the phase transition down to the lowest temperature is much smoother (weaker distortion) in FA-based systems [73, 78] than in MA-based ones [171]. However, it should be stressed that the broadening in the FA compounds can be affected by the possible dispersion of bundles b and c due to the likely incoherent nature of these peaks in INS experiments. Above 20 meV, optical features are essentially a result of molecular motions, although there could be some inorganic contributions to the cation librations of bundle c, at least for MA-containing perovskites. Meanwhile, direct comparison between the MAPB and FAPB spectra leads us to believe that the same mechanisms are possibly at play in the latter. It is apparent at least, that in FA-based compounds, as a result of the hybridized nature of the lowest energy modes, there is significantly more contribution stemming from the coupling between inorganic and organic sub-lattices.

In Fig. 4.5, the relative energy shifts of the labelled phonon bundles, between the four compounds, is presented. One can see that the low-energy bundles a have lower energy in compounds that contain I^- as opposed to Br^-. Analogously, there is a significant decrease in energy in the medium/high energy bundles when coming from MA-based compounds to FA ones. Recalling the harmonic approximation[3],

[3]For a simple harmonic oscillator, where a mass m which experiences a single force F, which pulls the mass in the direction of the point $x = 0$ and depends only on the position x of the mass and a constant k, Newton's second law dictates that $F = m\frac{d^2x}{dt^2} = -kx$. Solving this differential equation we find that the motion is described by the function $x(t) = Acos(\omega t + \varphi)$, where $\omega = \sqrt{k/m}$.

the phonon energy is proportional to the square root of the atomic mass, M, of the halide atom/organic molecule involved in that vibration [126]. Therefore, one expects on general grounds

$$\omega_j \propto \frac{1}{\sqrt{M}} \tag{4.1}$$

The atomic masses of each nucleus or molecule can be easily estimated: $M_{FA} = 45.1$ g/mol; $M_{MA} = 32.1$ g/mol; $M_{Pb} = 205.0$ g/mol; $M_I = 126.9$ g/mol; $M_{Br} = 79.9$ g/mol. One can then estimate relative energies of a given phonon when changing the molecule MA to FA or the halide I to Br when assuming the same atomic interactions. So, for a phonon where only the halide atom is involved, one expects:

$$\frac{\omega_j(iodides)}{\omega_j(bromides)} = \sqrt{\frac{M_{Br}}{M_I}} = 0.79. \tag{4.2}$$

In case the lead atom also participates to the vibration, one expects instead:

$$\frac{\omega_j(iodides)}{\omega_j(bromides)} = \sqrt{\frac{M_{Pb} + 3M_{Br}}{M_{Pb} + 3M_I}} = 0.87. \tag{4.3}$$

In both cases, the phonon energy of iodides will be lower than for bromides. In Fig. 5 of the main text, this corresponds to the bundle *a*, where one can estimate: $\frac{\omega_a(MAPI)}{\omega_a(MAPB)}$=0.6 and $\frac{\omega_a(FAPI)}{\omega_a(FAPB)}$=0.7. One notices that the measured effect is even larger than the estimated one. That suggests that the interactions responsible for that phonon bundles are weaker for bromides than iodides as the phonon energy is $\omega_j \propto \sqrt{\frac{k}{M}}$, where k represents atomic forces. For a given phonon where only the organic molecule is involved, one expects:

$$\frac{\omega_j(FA)}{\omega_j(MA)} = \sqrt{\frac{M_{MA}}{M_{FA}}} = 0.84. \tag{4.4}$$

The phonon energy is lower for the heavier FA molecule compared to MA. That corresponds to the bundle *c* where one can estimate $\frac{\omega_c(FAPB)}{\omega_c(MAPB)}$=0.96 and $\frac{\omega_c(FAPI)}{\omega_c(MAPI)}$=0.64. Here again, one sees that the experimental trend does not exactly match the prediction from the above relationship from atomic masses.

There is however an observable trend relating the total atomic mass of the elements and the respective mode attribution. Actually, the relative shifts observed here, *i.e.* lower energy in FA^+ and I^- based compounds when comparing with MA^+ and Br^-, are consistent with the smaller elastic constants obtained in Chapter 3.

It is now known, as we have established, that carrier scattering in HOPs is dominated by Fröhlich coupling between charge carriers and optical phonon modes. This phonon scattering is believed to be the key fundamental factor in establishing

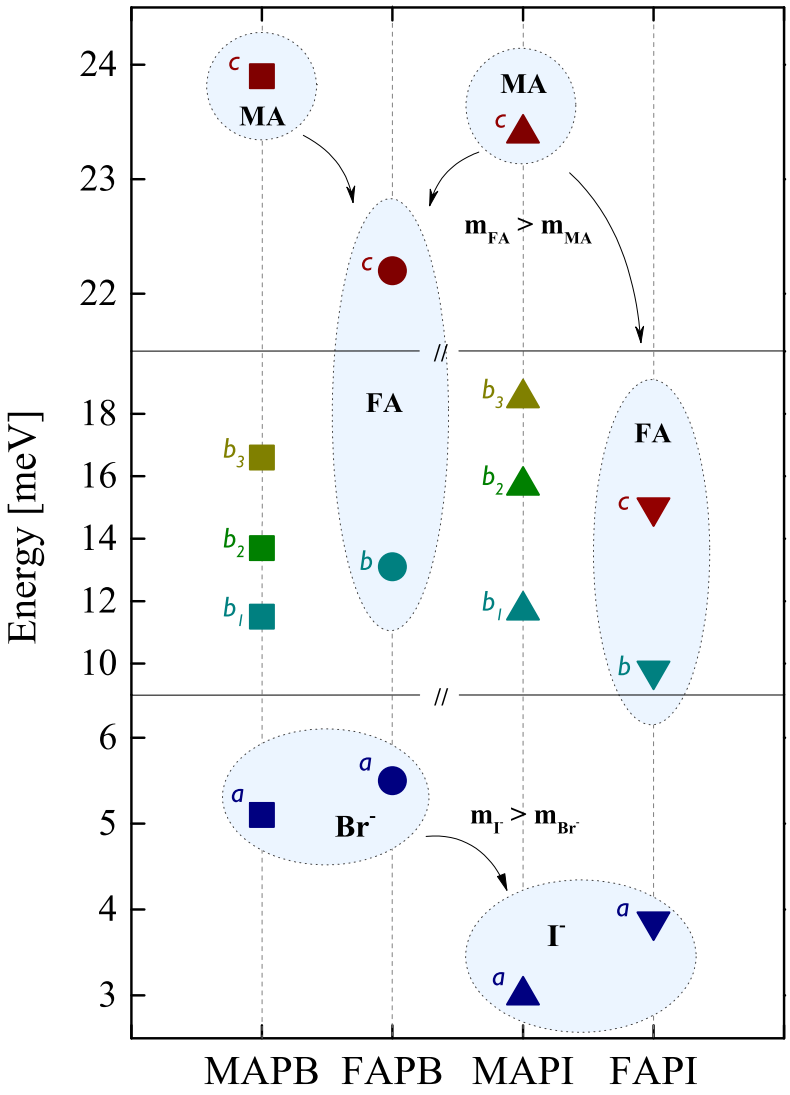

Figure 4.5: Optical phonon bundles a, b and c in MAPB, FAPB, MAPI and FAPI, illustrating the relative energy positions between compounds.

the intrinsic limit of the charge carriers mobility. More specifically, it has been recently suggested that this limit is set by the lower energy LO modes (3-20 meV) [167]. Therefore, the here observed presence of such modes, common in all four compounds, seems to be part of the reason for the relatively low mobilities compared to classical inorganic compounds like Si and GaAs. Furthermore, this also ties back with the hot phonon bottleneck, outlined in chapter 3, in which the Frölich interaction is said to occur mainly between the hot carriers and LO phonons of inorganic sub-lattice.

The lack of dispersion of such low optical modes overlapping with the upper part of the acoustic phonon dispersions has further implications in the proposed bottleneck effect. In 3D hydrid perovskites, substantial interactions between the organic and Pb-halogen neighbouring networks are typically expected, however, besides be-

ing located at low energy range, the optical lattice excitations measured here appear to be basically non-propagating (Figures 4.1 and 4.2), exhibiting nearly no dispersion in the BZ, thus contradicting existing reports on phonon simulations based on the harmonic approximation. This will be further expanded upon in the coming chapter. What is more relevant is the fact that, similarly to phonon modes in thermoelectric chlarates [172], strong anharmonic phonon–phonon scattering processes may lead to a series of anticrossings flattening phonons dispersions. For instance, this strong hybridization between phonons would typically involve rattling of the organic molecule within the PbX_3 cage. Moreover, rattling phonon modes are generally associated with anharmonicity and lower thermal conductivities [173, 174] as it has been proposed through a crystal-liquid duality of HOPs [175]. Interestingly, it has been suggested that optical flat modes (as the ones we here observed) highly scatter acoustic phonons leading to glassy-like thermal conductivity [176]. Therefore, not only the dispersionless nature of the optical modes - responsible in great part for the low thermal conductivities, through the blocking of propagation of the acoustic phonons - but also the overlap of these same acoustic and optical phonons, constitute key factors in the hot phonon bottleneck effect in HOPs, since they facilitate acoustic phonon up-conversion and increase the lifetime of their hot carrier population [52, 154, 177, 178]. However, in the bottleneck process proposed by Yang *et al.* [9], they point to the organic cations as the source of the overlapping optical phonons. From our results, it appears rather, that these originate from the PbX_3 inorganic sublattice.

In conclusion, we present here an extensive comparison of optical phonon excitations in four different hybrid organolead perovskite compounds. INS and complementary Raman scattering measurements revealed various features at low temperature spectra, which we then discussed in terms of the corresponding structural vibrations. The dispersionless nature of these optical modes implicates a glassy-like thermal conductivity, important to the hot phonon bottleneck effect in HOPs. These experimental results could serve as a solid base in future theoretical calculations and modelling, for improved mode assignment and understanding of the electron-phonon interactions, especially for FA-based compounds where measurements of their optical phonon spectrum have been lacking.

Chapter 5

Temperature behaviour of lattice dynamics and phase transitions

Here, we perform temperature studies on the four hybrid perovskites. Ramnan spectra reveal a common behaviour across the cubic-tetragonal transition, which does not seem to be controlled by a soft mode (i.e. non-displacive transition). A pre-transitional effect in FAPB is manifested in the softening of its shear modulus. We also note substantial phonon overdamping, as a result of intrinsic lattice anharmonicity. This may have an important influence in phonon scattering dynamics and, consequently, in charge carrier transport in HOPs.

5.1 Evolution of lattice dynamics by INS

5.1.1 Anharmonicity

It has been made clear that intrinsic anharmonicity of the perovskite lattice is expected to play an important role in the electron-phonon interactions of HOPs and we already see some evidence of the first on the FA-based samples in chapter 4. Besides, we still need to try and address the apparent discrepancy between the experimental acoustic-like temperature dependence of carrier mobilities and the expected dominant Fröhlich process. We then proceeded to measure optical phonon spectra as a function of temperature and look at how the anharmonic effects evolve with it. A temperature range of 5-300 K was covered, in which the same R point in MAPB, MAPI and FAPI (Fig. 5.1.a,b,d) and M point in FAPB (Fig. 5.1.c), were followed.

Anharmonicity manifests itself strongly already at low temperatures well below RT, where optoelectronic devices and solar cells are usually operated. Already above ∼30 K, increased phonon damping is observed across the board in Fig. 5.1, together with an increased low energy signal and reduced phonon intensity. Consistent DHO fitting of the temperature data has proven difficult due to the strong anharmonic behaviour. With increasing temperature, the increase of atomic displacement amplitudes results in a decrease of the Debye–Waller factor (Eq. 2.30, section 2.2.3), larger contribution from the quasi-elastic low energy components and broader phonon modes. These effects lead to a rather quick overdamping of certain phonon modes at temperatures as low as 80 K, making it difficult to properly assign the exact contribution of each phonon mode to the overall spectra at higher temperatures.

5.1.2 Overdamping at high temperature

This phonon overdamping is highlighted in Fig. 5.2. At RT, with a maximum energy range of 13 meV, the full contour plot of $S(q, E)$, for MAPI is provided in Fig. 5.2.a. The TOF mapping shows no well-defined phonon modes within the measured range, which is in line with the already referenced neutron scattering report on MAPI by Li *et al.* [160]. In Fig. 5.2.b we have put together the highest temperature TAS scans for each compound (where MAPI alone is in the tetragonal phase, the other three being in the cubic one). We remind that scans in MAPI, MAPB and FAPB were measured in a thermal neutron source (1T), allowing us to extend the energy range up to 44 meV. However, due to the different reciprocal space configuration used to access the M point on FAPB, a slightly lower energy is reached. Similarly,

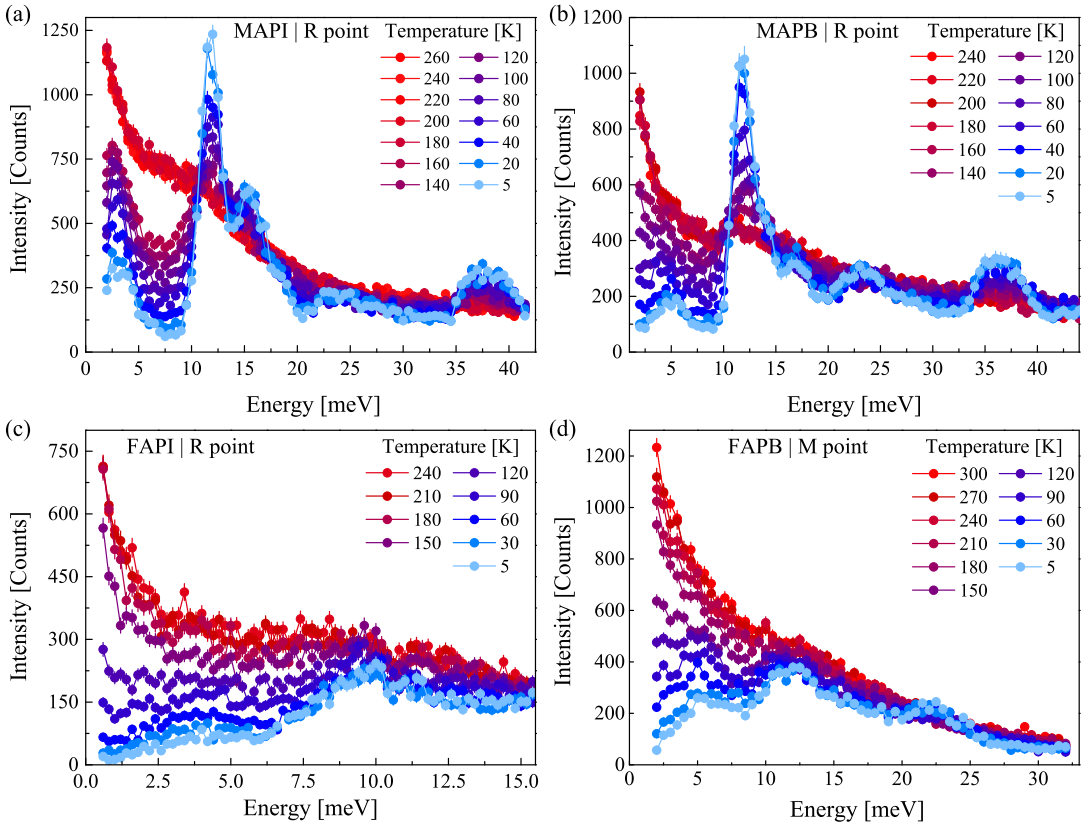

Figure 5.1: Temperature dependence of the INS optical spectra at the R point of **(a)** MAPI, **(b)** MAPB and **(c)** FAPI and **(d)** at the R point of FAPB. **(a), (b) and (d)** are measured at LLB on the thermal TAS (1T) and **(c)** on the cold TAS at LLB (4F2).

these show mainly a big quasi-elastic signal, centered at zero energy. Accordingly, broad optical phonons around 12 meV were hardly visible in MAPB at RT [146] in a previous work of our group.

In agreement with the observed broadening of the acoustic branches at the ZB in $MAPbCl_3$ [179], at high temperature, only low energy acoustic phonons can be identified (see supplementary Fig. B5)[1]. The dispersive optical phonon modes reported at RT by inelastic X-Ray scattering [139], with its broader energy resolution (*i.e.* ∼1.5 meV), are then put into question.

The phonon damping here observed seems to be specially affected by the orthorhombic-tetragonal structural transition, which relates well with the fairly established claim that transitions originate from the tilting of the PbX_3 cage and the orientational ordering of the organic molecules [66, 80–84], driven by instabilities at the M and R Bragg points. The evolution of the spectra shows as well the absence of any particular soft modes at the M or R Point, meaning that they do not seem to condensate with temperature. Only a large increase of the phonon damping is

[1]These are the same type of phonons we report in chapter 3 and in publications [146]

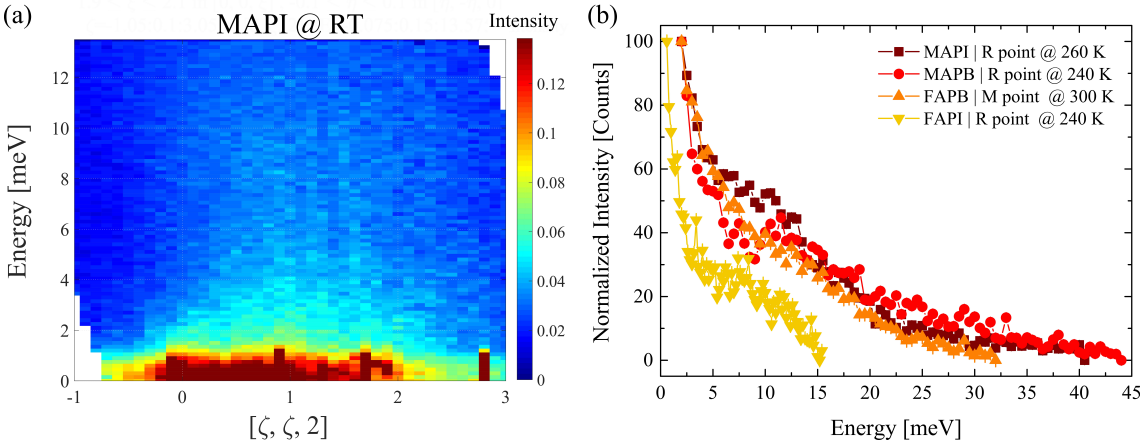

Figure 5.2: (a) ToF contour plot of MAPI at RT, for an energy range of 0-13 meV. (b) Normalized TAS spectra of optical phonons at the M $(5/2, 1/2, 0)$ and R $(1/2, 1/2, 3/2)$ points of the BZ, in MAPB, MAPI, FAPB and FAPI. The temperature of each scan is labelled.

observed. This points towards a non-displacive tetragonal to orthorhombic phase transition. Based on Fig. 5.1, the main bundles identified at low temperature, are expected to be present at the same respective energies at high temperature, although overdamped. This is further supported by the Raman measurements at high temperature range (vide infra).

While the anharmonicity of HOPs leads to low frequency acoustic phonons, which are characteristic of a soft lattice (as seen in chapter 3), it shows off for optical phonons through an overdamped behaviour over the entire BZ at RT. The apparent discrepancy between the experimental acoustic-like temperature dependence of carrier mobilities and the expected dominant process (Fröhlich interaction) may be an unexpected consequence of the HOPs lattice softness, making the overriding anharmonic character of optical phonons specific to this class of halide perovskite materials, most probably an important missing link in current models. The size of the cation and the nature of the halogen are additional features known, to strongly influence softness of the lattice. They also have a direct consequence on the damping of the optical modes. Therefore, this suggests that the coupling between acoustic and optical phonons may play a role in the harmonicity of the lattice, besides nonlinear coupling between optical phonons.

5.2 Cubic to tetragonal phase transition

Just now we saw that with INS, we are not able to properly follow the optical phonon features in our HOPs, above a certain temperature. Remembering the point that we made regarding mode broadening related to instrumental resolution being less

critical in Raman then in neutron scattering, we then used Raman spectroscopy to better investigate the low frequency vibrational response of each compound, across their cubic to tetragonal phase transition. These experiments were conducted in Montpellier by the L3C team in the context of a joint project.

The collected Raman spectra are shown in Fig. 5.3. Four scattering geometries have been explored in MAPB, FAPB, and MAPI, *i.e.* with the wave vector q // [001] and the polarization of the laser beam parallel to either [110] and [100] directions, and the scattered beam polarized parallel (polarized spectra) or perpendicular (depolarized spectra) to it. The polarized and depolarized spectra (selection rules) provides infomation on the symmetry of the modes (*i.e.* if they are T_{2g}, A_{1g}, E_g, ...) However, the intensity of the modes are not the same in polarized and depolarized spectra. The spectra presented in Fig. 5.3 corresponds to polarized spectra with incident polarization parallel to [110], as this is the configuration where the low frequency mode offers the most favourable contrast and easiest to fit in the cubic phase. They have been recorded at the same position into the sample in order to avoid modifications due to the formation of structural domains below the transition temperature, T_c.

A direct observation already suggests that the responses in the cubic phase very much look like a smeared-out version of that of the tetragonal phase, identical to what one appertained from the INS data. In MAPB where the modes are almost spectrally resolved, the lowest frequency bundle (red in Fig. 5.3.a) is comprised by the modes ω_1, ω_2 and ω_3. They are broad but still resolved in the tetragonal phase. However, increasing temperature, they undergo further broadening, leading to the rather overdamped Raman response in the cubic phase. The situation is analogous in FAPB and MAPI. In FAPI on the other hand, mentioned several times to be a challenging compound to perform spectroscopy on, the spectra are limited to one single set obtained along an arbitrary crystallographic direction and performed without polarization analysis. Luckily, ω_1 clearly develops in the tetragonal phase and could be followed with temperature. It was however impossible to choose the scattering conditions that emphasize its scattering in the cubic phase, and we had to satisfy with the spectra of Fig. 5.3 showing an almost monotonous intensity decay of the Raman signal.

All the spectra have been fitted using slightly modified version the DHO model used for INS (see Eq. 2.41, section 2.5.1), which accounts for ω_1, ω_2, ω_3. A fourth DHO (ω_4), at frequency just above the three other modes, was also required to ensure a good fitting quality. In order to extract the individual spectral line shapes underlying these complex Raman responses, we fitted all the spectra collected in

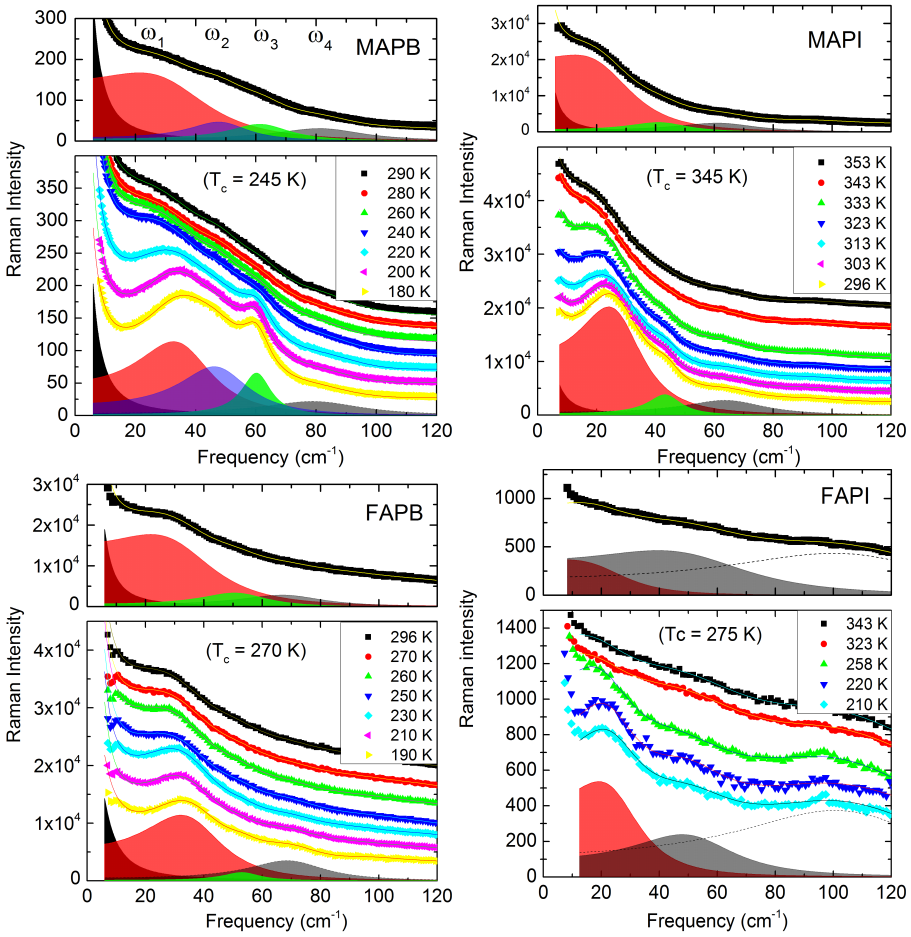

Figure 5.3: Polarized Raman spectra (symbols) in the tetragonal and cubic phases of the four HOPs, with their respective fits (plain lines). For each compound, the individual spectral line shapes $S_i(\omega)$ ($i = 1$ in red, $i = 2$ in blue, $i = 3$ in green, $i = 4$ in gray) are shown for the lowest temperature spectra (bottom, tetragonal phase) and for the highest temperature spectra (top, cubic phase).

the four scattering geometries. Since the modes are more or less active depending on the scattering geometry, this is a clear asset for separating the bands when they are strongly overlapping, in particular at the onset of the cubic phase. For example, it is easier to follow ω_2 in the depolarized spectra of MAPB because, in contrast with the polarized one, ω_1 is significantly weaker and can hardly be distinguished within the other ones (supplementary Fig. B6). In FAPB and MAPI however, it was not necessary to consider it during the spectral analysis, as shown in Fig. 5.3. In the next section we proceed to explore the behaviour of this lowest frequency (LF) Raman mode ω_1, across the tetragonal-cubic transition.

Lowest frequency Raman mode

As opposed to a soft mode behaviour, the frequency ω_1 is fairly constant with temperature in MAPB, FAPB, and MAPI (Fig. 5.4.a). The data in FAPI in the cubic

phase were very difficult to analyse, and to help the fit converging to a reasonable solution we fixed its frequency ω_1 to a constant value extrapolated from the low-T data (dashed line in Fig. 5.4.a). Contrary to the frequencies, the four spectral dampings exhibit a clear drop down at the onset of T_c (Fig. 5.4.b). One has however $\Gamma_1 > \omega_{01}$, and it is known that the experimental determination of ω_0 and Γ from the spectral lineshape of an highly damped oscillator is quite problematic.

When phonons become highly damped, the width and the frequency of their spectral response becomes strongly correlated. In the extreme situation where a mode is overdamped, several couples $\{\omega_0, \Gamma_0\}$ may produce the same spectral shape. The most reliable spectral quantity in that case, is then given by the relaxational frequency

$$\omega_{Rel} = \frac{\omega_0^2}{\Gamma} \tag{5.1}$$

corresponding to the half width at half maximum of the full spectral response of $S_1(\omega)$ (Stoke and anti-Stoke). This can be seen as the inverse characteristic time of the relaxational dynamics associated to the mode in question. It only has physical meaning when the mode is close to overdamping, *i.e.* at the frontier between a relaxator and a vibrator. The results are shown in Fig. 5.4.c as a function of $T - T_c$ and after a normalization by the value of ω_{Rel} in the cubic phase. In all the samples, the cubic to tetragonal phase transition is marked by a clear narrowing of the mode below T_c and the curves overlap very nicely, emphasizing a common dynamical behaviour. The statistical error on ω_{Rel} is smaller than that on ω_{01} and Γ_1, allowing thereby to refine the values of the transition temperatures. From the Raman analysis we find the following T_c's: MAPB ∼245 K, FAPB ∼270 K and FAPI ∼275 K. These agree with the literature mentioned in section 1.3.3. For MAPI, we took the literature data T_c ∼345 K [56]. A similar normalization also works for the width (Fig. 5.4.d), however, with a higher uncertainty in the definition of T_c.

Another reliable quantity that can be extracted from the DHO model of lattice modes with large dampings is the overdamp frequency

$$\omega_{OD} = \pm\sqrt{\omega_{01}^2 - \Gamma_1^2/4} \tag{5.2}$$

defining the frequency of the temporal response $u_1(t)$ of the oscillator in the absence of a driving force

$$u(t) = u_{01} e^{-t\Gamma_1/2} \cos(\omega_{OD} t + \phi) \tag{5.3}$$

where $\omega_{OD} = 0$ (dashed line in Fig. 5.5.a) defines the overdamp limit, corresponding to the transition from a vibrational regime ($\omega_{01} > \Gamma_1/2$), towards a relaxational one ($\omega_{01} < \Gamma_1/2$). Within this model, the atomic displacements $u_1(t)$ plotted in

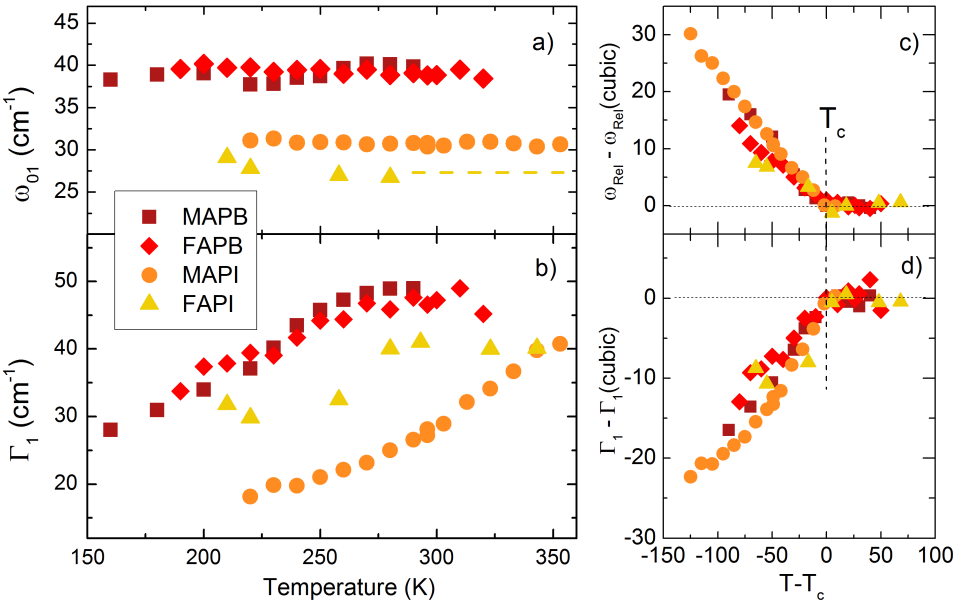

Figure 5.4: Vibrationnal parameters of the Raman mode of lowest frequency in MAPB, FAPB, MAPI, and FAPI: **(a)** Temperature dependence of the frequencies ω_{01} and **(b)** dampings Γ_1. **(c)** Normalized relaxational frequencies ω_{Rel}(T-T$_C$)-ω_{Rel}(cubic) and **(d)** normalized dampings Γ_1(T-T$_C$)-Γ_1(cubic).

Fig. 5.5.a are all harmonic oscillators. Although strongly damped the vibration is therefore vibrational-like rather than relaxational-like. Another interesting quantity is the maximum of the phonon response $S_1(\omega)$ at $\omega_{MAX} = \pm\sqrt{\omega_{01}^2 - \Gamma_1^2/2}$. The limit $\omega_{MAX} = 0$ (*i.e.* $\omega_{01} = \Gamma_1\sqrt{2}$), is reached when the Stoke and anti-Stokes maxima of $S_1(\omega)$ merge into one single peak centered at ω=0. $S_1(\omega)$ are plotted in Fig. 5.5.b using the fitted values of ω_{01} and Γ_1 obtained in the cubic phase and averaged over all the data. The responses of MAPB and FAPB are very similar and almost superpose. Considering the large errorbars on FAPI data, the responses of MAPI and FAPI are also very similar but stand at lower frequency than the two former. The response function of a vibration at the crossover towards a relaxational regime ($\omega_{OD} = 0$) is shown for comparison (dashed line).

The renormalization of the vibrational responses into master curves Γ_1(T-T$_c$) and ω_{Rel}(T-T$_c$) (Fig. 5.4.c,d) strongly supports a unified description of the vibrational properties in the four compounds. In particular, the frequency ω_{01} of the low frequency mode is constant when passing through the cubic-tetragonal transition (Fig. 5.4a). The constant value of ω_0 in the cubic phase goes against a ZC displacive transition and indicates that this vibration cannot be considered as a soft-mode. At the same time, the non-normalized version of the relaxational frequencies ω_{Rel} (supplementary Fig. B7 shows that, although the cubic-tetragonal transition is again clearly marked, it is less abrupt in Br-containing samples, sug-

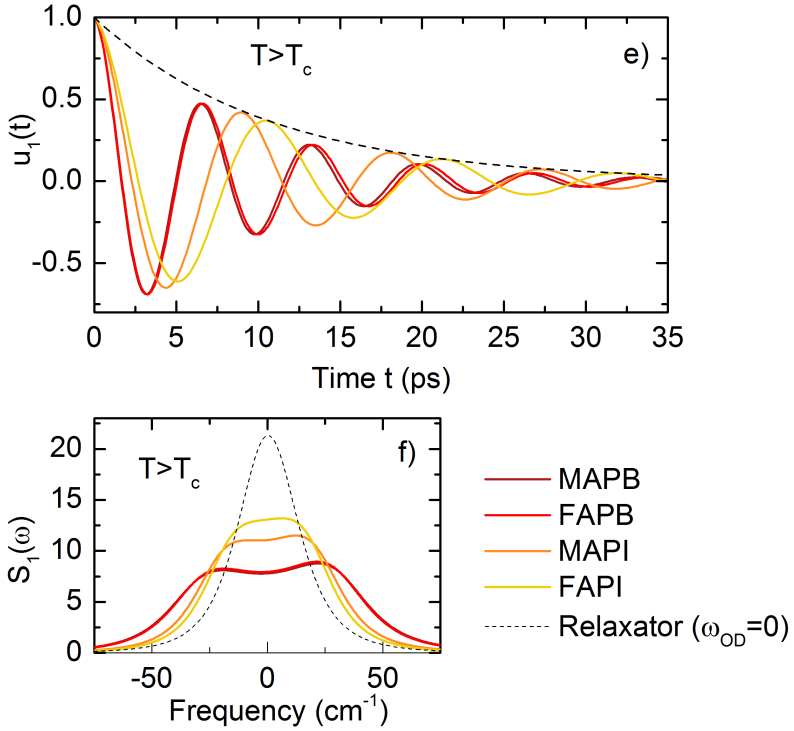

Figure 5.5: **(a)** Temporal responses of the atomic displacements and **(b)** spectral line shapes in the cubic phase of MAPB, FAPB, MAPI, and FAPI.

gesting pre-transitional effects in the latter). In section 5.2.2, we further investigate pre-transitional effects in FAPB.

The two bromide samples exhibit similar frequency and damping in the cubic phase, and same is observed in the two iodine ones (Fig. 5.4.a,b). Furthermore, analogously to what was seen with INS for orthorhombic phase, their frequency is inversely proportional to the square root of the mass of the halide atom, *i.e.* $\omega_{01} \propto 1/\sqrt{M}$, so that ω_{01}(bromides) / ω_{01}(iodines) $= \sqrt{M_I/M_{Br}}$. This can be seen in Fig. 5.6, where the linewidth Γ_{01} and the frequencies ω_{MAX}, ω_{OD}, ω_{Rel} and ω_{01}, in their cubic phases, are summarized for the four compounds. Here, we are forced to note the striking similarity with Fig. 4.5. These observations regarding ω_{01}, reinforce the attribution of the motions of the PbX_6 halide octahedra as the origin of the phonon mode.

One observes that, overall, the vibrational dynamics are of lower frequency in the two iodine-containing samples, where FAPI is clearly the softest of the four samples. The energy of its low-frequency mode is significantly lower than the other three but, despite reaching the critical regime ($\omega_{MAX} = 0$), the mode conserves its vibrational character, as shown by the sinusoidal shape its temporal response in Fig. 5.5.a ($\omega_{OD} \geq 0$). The above conclusions, based solely on the frequency of ω_1, apply to all of its fitting parameters, confirming the consistency of the spectral

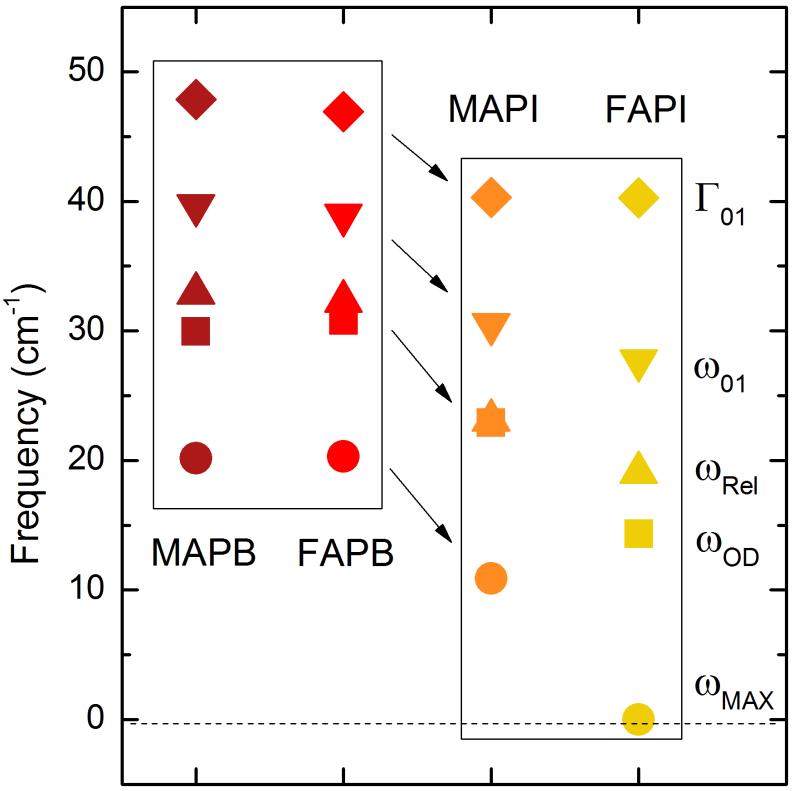

Figure 5.6: Characteristic frequencies and linewidth of the low frequency Raman mode in MAPB, FAPB, MAPI and FAPI, in their cubic phase (290 K, 353 K, 296 K and 343 K, respectively).

analysis.

5.2.1 Intermediate tetragonal phase of $MAPbBr_3$

In MAPB, Raman spectroscopy was performed across a wider temperature range, covering the totality of its phase transitions. The low temperature spectra (20 K) in Fig. 5.7, reveals additional features below 80 cm^{-1} in the orthorhombic phase. More specifically, eight modes are identified, which compose the lowest frequency bundle of MAPB, shown in red in Fig. 5.6. Among them, three main responses can be followed up to high temperatures from the direct inspection of the raw data. These are the ω_1, ω_2 and ω_3 modes identified in the previous section 5.2. They are identified by square symbols in Fig. 5.7 and again, we can see that their frequency has an almost flat temperature dependence (Fig. 5.7.a) while the linewidths are all strongly affected by the structural instabilities (Fig. 5.7.b). These exhibit a steep narrowing at the tetragonal-orthorhombic transition, dropping down (more continuously) close to the cubic-tetragonal transition. It was said in the introductory chapter, that MAPB has an additional intermediate tetragonal (P4/mmm) phase between ∼145-155 K. Our Raman data confirms the existence of the intermediate phase, in our case happening between ∼141 K and ∼147 K, combining the tetrago-

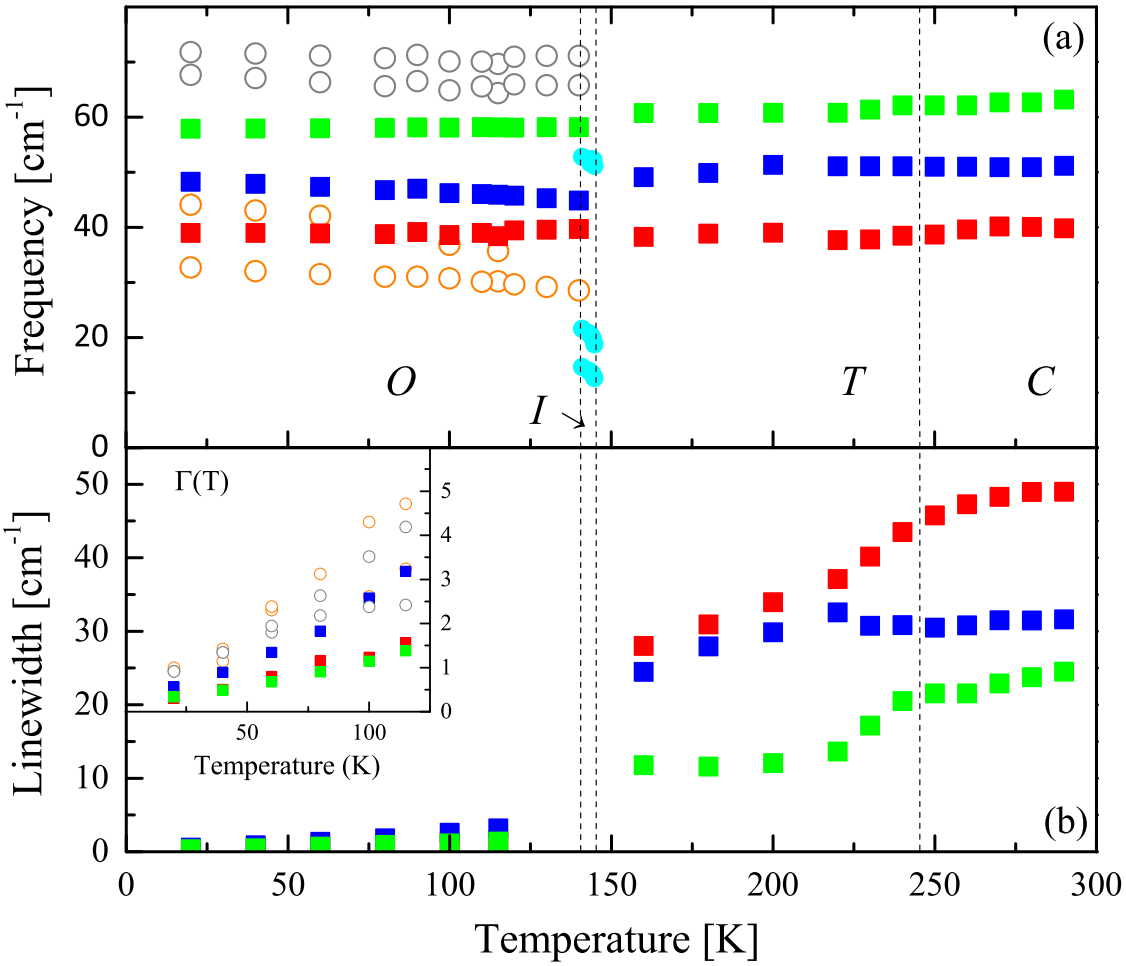

Figure 5.7: Raman spectroscopy in MAPB across the three phase transitions : cubic (C), tetragonal (T), Intermediate (I), and orthorhombic (O). **a)** phonon frequency and **b)** phonon linewidth (zoom in the inset) resulting from a fit with damped harmonic oscillators. **c)** Low-frequency Raman responses at the tetragonal-orthorhombic transition and **d)** same spectra in the medium and high frequency domain, as defined in the text. The main phonon bands are identified by black, green and red filled squares (panels a,b,c) and double arrows (panel c).

nal structure and an intermediate one characterized by very sharp bands (cyan dots in the region I in Fig. 5.7). We have also observed an hysteresis effect on cooling and heating, and therefore the temperature interval of the cubic phase (C) may slightly move downward in temperature, depending on the thermal route.

We take this opportunity to further compare Raman scattering spectra in MAPB, above and below the orthorhombic to tetragonal first order transition ∼150 K, as shown in Fig. 5.8. When passing the phase transition and on cooling down to 20 K one notices a considerable narrowing of the phonons lines below 10 meV, while higher frequency vibrations evolve much more smoothly and continuously. Furthermore, phonon modes are split at low temperature below 10 meV (Fig. 4.4). We can now see that the additional Raman scattering modes, not easily seen with INS (see Fig. 4.3 and/or Fig. 4.4), result from the band folding in the low temperature phase,

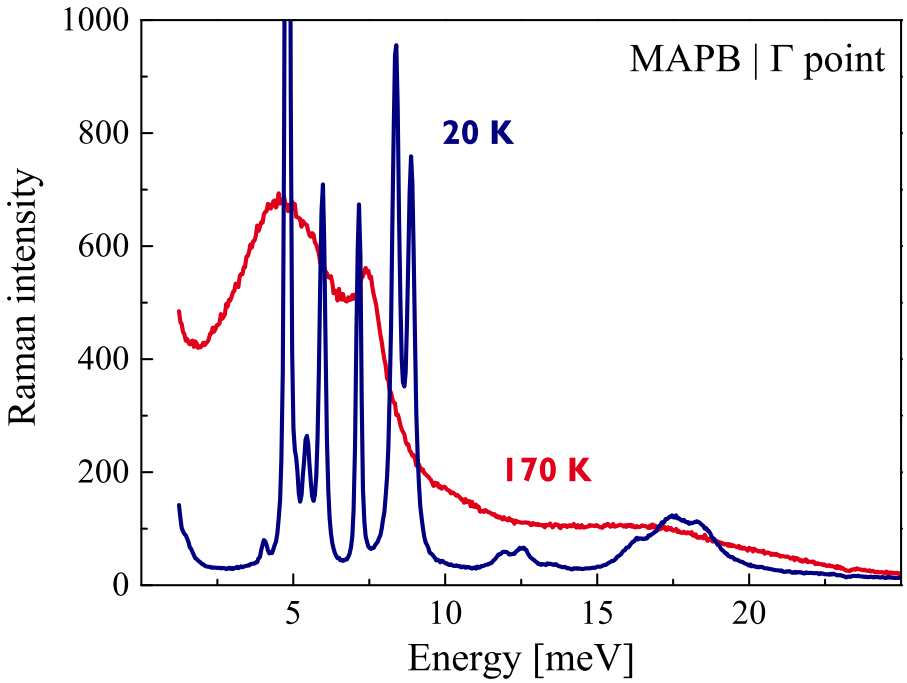

Figure 5.8: Comparison of the Raman responses in MAPB, above (170 K) and below (20 K) the orthorhombic-tetragonal transition.

induced by the structural distortion caused by the phase transition.

When examining the low temperature INS spectra of the four HOPs, we drew attention to an increased broadening of the phonon bundles of FA-based compounds compared to the MA counterparts. This apparent broad nature can be simply due to the incoherent scattering from the modes, which, in FA-based systems, seem to be packed together in a narrower energy range, magnifying their hydrized nature. However, the difference in broadening between the compounds relates well, not only with the re-orientational dynamics of the FA and MA molecules, but also with the claims of weaker distortion across phase transitions in FAPI compared to MA-based systems. In fact, we also observe a smooth evolution of the lattice parameter of FAPB with temperature (vide infra). If that is the case, the band folding of the modes (as seen in MAPB) should be noticeably reduced in FA-based HOPs. Unfortunately, as it was said already, we do not have the Raman spectra on FA-based compounds at low temperature, to verify this hypothesis.

5.2.2 Phonon softening in $FAPbBr_3$

As we have just seen from the analysis of the lowest frequency optical mode in Raman, there is some indication of pre-transitional effects in Br-based samples. Besides, when investigating the acoustic phonons in our HOP compounds, we noticed a discrepancy between BLS and INS, which highlighted a softening of the transverse

mode C_{44} in FAPB, as a function of q. The softening of the shear modulus is typically related to the proximity of a ferroelastic transition [148], however such is not reported for these systems. To better understand this pseudo-ferroelastic behaviour we proceeded to look at how C_{44} evolves with temperature, across the phase cubic-tetragonal transition.

We started by looking how the elastic behaviour of the different Bragg reflections evolved with temperature across full temperature range. As mentioned in the introduction (section 1.3.3), FAPB is reported to undergo a 1st order transition at T_c ∼160 K and a 2nd order one at T_C ∼260 K. We verify this in Fig. 5.9, where INS measurements of the elastic response of the (110), (002), R (1/2 1/2 3/2) and M (3/2 1/2 0) points as a function of temperature are shown. In these measurements we are simply measuring the intensity of the Bragg peak via Q-scans with zero energy transfer. The cubic to tetragonal phase transition is driven by structural distortion originating at the M point, *e.g.* $Q = (3/2, 1/2, 0)$, reflected by the marked increase of its scattering intensity, right above 250 K, which prolongs until 160 K (green data points in Fig. 5.9), when the tetragonal-orthorhombic transition is supposed to happen. This transition is mainly driven by the R point, *e.g.* $Q = (1/2, 1/2, 3/2)$ and, being a 1st order transition into the most ordered phase, where the molecular orientations are frozen, it leads to the most significant change in terms of structural re-ordering, clearly seen in the overall fluctuations in scattering intensity from all four measured Bragg reflections. However, curiously, the "activation" of the R point is happening at around 180 K, before the expected transition is reached. This is also where the gradual increase of the elastic responses of the (110) and (002) Bragg reflections that had accompany the rise of the M point, suffer an oscillation (Fig. 5.9, yellow and orange). So, although the steep intensity drop of not only the R point, but also the other measured Bragg peaks, seems to signalize the consummation of a 1st order transition, it appears that, like it is observed in MAPB, an intermediate phase might be present.

From the inset of Fig. 5.9, we can also observe that, throughout the phase transitions, the average lattice parameter[2] of FAPB evolves very smoothly, showing an absolute variation of simply ∼0.007. This suggest that the crystal maintains a pseudo-cubic unit cell [73] tying back with the already mentioned PL studies claiming that transitions in FA-based compounds, implicate relatively weaker distortion comparing to MA-based ones [73, 78, 171].

Next we performed the temperature study of the C_{44} acoustic branch in

[2]Due to the presence of phase domains in HOPs, one has to consider an average lattice parameter.

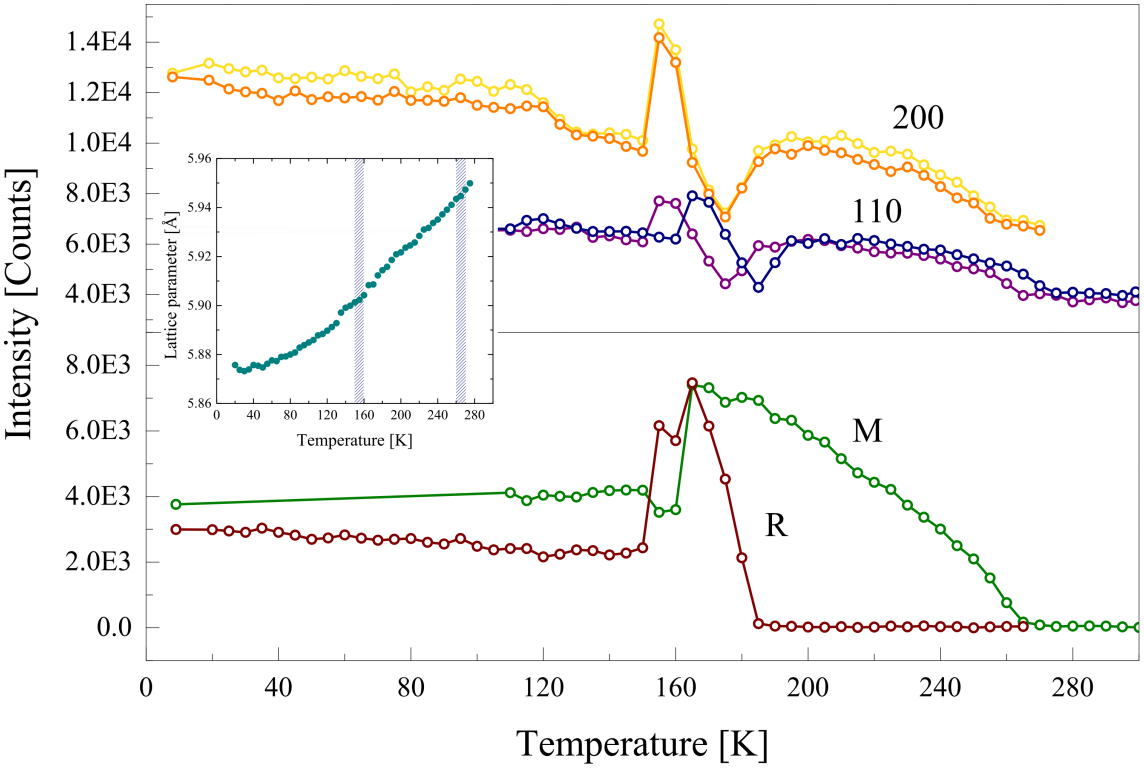

Figure 5.9: Elastic scattering intensity from the 002, 110, R and M Bragg reflections in FAPB, as a function of temperature. The structural phase transitions are marked with vertical lines. Inset shows the evolution of the (pseudocubic) lattice parameter of FAPB within the same temperature range.

$FAPbBr_3$, using INS at constant $Q = (2, 0.025, 0.025)$. This reciprocal point was chosen since, as explained in chapter 3, one can obtain the shear modulus by measuring phonons transverse to the 002 Γ point.

In Fig. 5.10.a, one can indeed observe that C_{44} is drastically reduced as soon as we start to cool down the sample below RT. However, that effect is blocked once we reach ∼260 K. As we have said, at around 265 K, $FAPbBr_3$ undergoes a cubic to tetragonal 2^{nd} order phase transition, characterized by the doubling of the unit cell of the crystal, revealed by the appearance of a Bragg reflection at the M point (Figures 5.9.a and 5.10.a). It is known that lead perovskites exhibit structural instabilities at both the M and R points [158]. However, such anti-ferrodistorsive instabilities cannot generate any softening of the elastic constants, in the disordered phase (here above 265 K) [148]. Therefore, the softening of C_{44} at high temperature is due to an independent tendency towards a ferroelastic instability, which is blocked by the cubic to tetragonal phase transition, limiting ferroelastic pre-transitional effects compared to what would be expected for a full phase transition [148]. In Fig. 5.10.a, one can easily see how the two processes coincide. By linearly extrapolating the softening rate at high temperature (before it is blocked), one can estimate

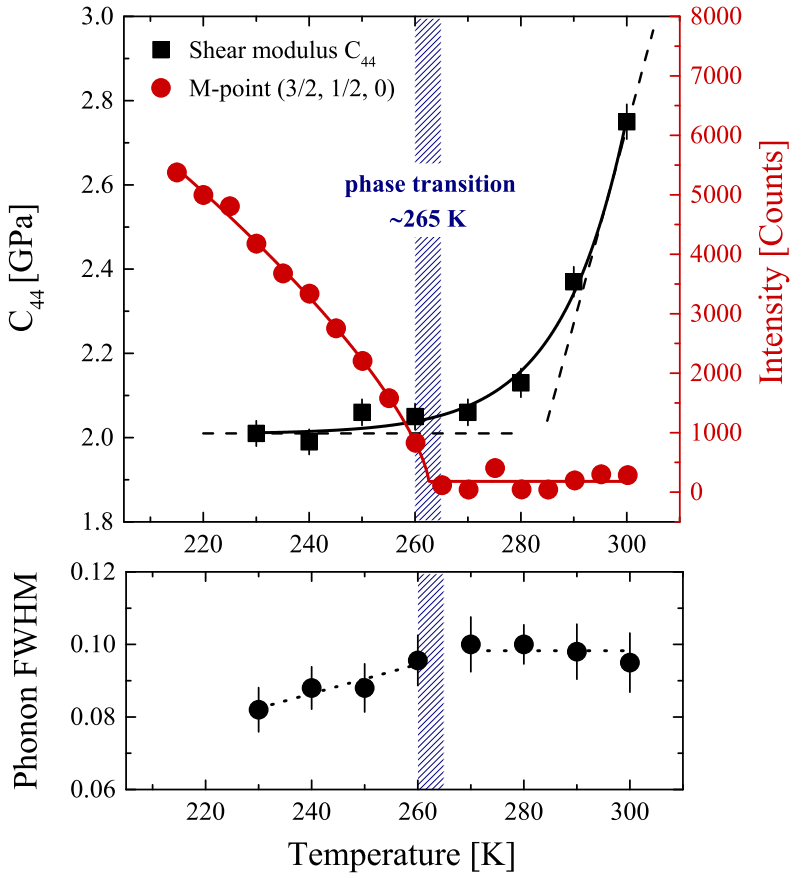

Figure 5.10: (a) Softening of C_{44} and (b) phonon width in $FAPbBr_3$ as function of temperature, between 230 and 300 K, at around the (002) Bragg reflection. Also in (a) the Bragg M point intensity (red) across a similar temperature range.

that such a ferroelastic transition would occur around 240±20 K. Consistent also with an aborted ferroelastic instability, a very modest phonon broadening is observed with decreasing temperature from 300 to 230 K (Fig. 5.10.b). Down at 100 K, C_{44} is then restored to its original value (see supplementary Fig. B8).

Again unfortunately, due to beam-time constraints, where we had to give priority to other studies presented in this manuscript, we do not have a cohesive set of measurements for the other three systems, of the elastic constants as a function of temperature.

5.3 Conclusion

We have employed Raman scattering to investigate vibrational dynamics at ZC across the cubic-tetragonal transition. The analysis focuses on the accurate description of lowest frequency mode in the Raman response spectra of the four HOPs. With INS, a wider temperature range was covered (5-300 K), in which main Bragg

reflections and the evolution of their optical phonon spectra were followed. The temperature-dependent measurements of optical excitations across both the structural phase transitions, show that these are not controlled by a soft mode, indicative of non-displacive structural phase transitions. Additionally, we observe indications of pre-transitional effects in FAPB, with INS. More specifically, the softening of the transverse acoustic mode C_{44}, points towards an incipient ferroelastic transition. The Raman study also confirms the existence of an intermediate tetragonal phase structure in MAPB, between ∼141 K and ∼147 K, which agrees within some slight deviation with previous literature reports.

Our experimental study of optical phonons clearly indicates that a missing ingredient of nowadays attempt to reproduce the observed temperature dependence of charge carrier mobilities in HOPs, is related to the underlying harmonic or quasi-harmonic assumptions of phonon modelling. Both the INS and Raman spectra show significant phonon overdamping at high temperatures. This large damping of phonons is a signature of substancial anharmonicity, which results from the dispersionless nature of optical phonons and the ensuing strong acoustic-optical phonon coupling. More, this coupling shows off as well in the anharmonicity of the upper part of the acoustic phonon branches. This is further enhanced by the mutually coupled organic and inorganic sub-lattices and the resulting hybridized nature of various phonon modes. This damping of the phonons seems to be particularly affected by the tetragonal-orthorhombic transition. However, the anharmonic behaviour, is even observed at temperatures well below the ones used for operating optoelectronic devices and solar cells, which makes it questionable defining optical phonons as well-defined quasi-particles above 80-100 K. So, together with an apparent correlation between lattices softness (*i.e.* elastic constants) and optical phonon energy/frequency, our results point to the influence of the acoustic and optical phonon coupling on the harmonicity of the lattice and the Fröhlich interaction between charge carriers and optical phonons. The low thermal conductivity and the phonon bottleneck, promoting hot carrier effects in HOPs, are additional manifestations of the strong acousto-optical anharmonic coupling.

Chapter 6

Final remarks and outlook

In recent years, research into halide perovskite PVs has flourished, drawing a lot of attention from the scientific community. The advent of this new technology resulted in a sustained research effort, yielding rapid advances of understanding and ever improving record efficiencies. However, most of the progress has been through empirical device improvements. A number of key fundamental questions regarding the interaction of charge-carriers with lattice vibrations (*i.e.* phonons) remains a subject of intense debate.

This project aimed to shine a light on some of these EPIs and the correlations between structural and optoelectronics properties in HOPs. For that purposed we have performed a number of neutron scattering experiments, along with optical spectroscopy measurements such as Raman and Brillouin, on four different HOP compounds. $MAPbBr_3$, $MAPbI_3$, $FAPbBr_3$ and $FAPbI_3$ constitute the most relevant set of perovskite samples in the current landscape and the probing of single crystals via neutron scattering provides the ideal platform to uncover their fundamental characteristics.

By measuring low frequency excitations, we are able to determine, for the first time, a complete set of experimentally measured elastic constants, in four of the technologically important HOP compounds. The lattice softness of these materials is evidenced by their overall very low C_{44} constant and bulk modulus, especially in the case of α-$FAPbI_3$ resulting in its structural instability and metastable nature at RT. The dispersion curves of acoustic phonons also highlight a systematic lower sound group velocity in the iodine-based samples, which should, theoretically, lead to lower charge-carrier mobilities. However, such is not the case. In fact, looking at the relationship between experimentally determined elastic constants and carrier mobilities, together with PL lineshape broadening studies, it has been deduced that optical phonons, rather than acoustic ones, dominate carrier scattering and mobilities at RT. On the other hand, this interpretation is not consistent with the observation of an acoustic-like temperature dependence of the mobility. We try to address this issue via the study of the full phonon spectrum of the HOPs.

In the low temperature spectra we identify a number of different optical features, the origin of which we then proceeded to thoroughly discuss. These flat modes appear at energies as low as 2-5 meV, merging with the high part of the acoustic phonon branches and could be part of the reason for the modest charge-carrier mobilities in HOPs, comparing to classic inorganic semiconductors. Generally speaking, the low- and high-energy range modes arise from the PbX_6 network and the organic cations, respectively. In the medium range (10-20 meV), the modes have a highly hybridized character. The low thermal conductivity and the hot-phonon bottleneck

effect in HOPs are further manifestations of the strong acousto-optical anharmonic coupling. In fact we observe an apparent correlation between, not only carrier thermalization and lattice softness, but also between the latter and optical phonon energy/frequency. We conclude that the dispersionless nature of the optical modes, responsible for the anharmonicity of the acoustic modes in HOPs, leads to their characteristic low elastic stiffness, which in turn implicates a glassy-like thermal conductivity. The hot-phonon bottleneck is then expected to be enhanced by elastic softness.

Temperature-dependent measurements accentuate the highly localized and anharmonic nature of the optical phonon modes. Such anharmonicity becomes overwhelming above 80-100 K, manifesting itself mainly through phonon overdamping. It is particularly affected by the tetragonal-orthorhombic transition but can be even seen at temperatures as low as 30 K, questioning, therefore, the current modelling of charge carrier mobilities based on a quasi-particle picture for low-energy optical lattice modes. Lattice softness in HOPs, and the underlying anharmonic nature of the mutually coupled acoustic and optical phonons, seems to be a missing component for a proper description of the carrier mobilities in these materials.

Moreover, both INS and Raman temperature-dependent measurements of optical spectra, indicate that the vibrational dynamics at the Brillouin zone-center, across the orthorhombic-tetragonal and tetragonal-cubic transitions, do not appear to be displacive (*i.e.* driven by a soft mode). The results from the Raman measurements also indicate pre-transitional effects in the Br-containing samples. This is reinforced by an observed tendency towards an incipient ferroelastic transition in $FAPbBr_3$ (manifested in the softening of the shear modulus C_{44}), which is interpreted as further evidence of the influence of plasticity in hybrid perovskites. Further measurement of the temperature dependence of the elastic constants should be made in the remaining three compounds.

Although we present here an extensive comparison of optical phonon excitations in the four different HOPs, additional experiments in deuterated samples are necessary in order to better isolate and determine the contributions from the organic and inorganic sub-lattices. By reducing incoherent scattering we will also be able to verify if the optical phonon modes that involve the organic cations are indeed essentially non-didispersive. Nevertheless, our experimental work can provide not only a reference for the on-going experimental studies dedicated to exciton-phonon coupling in hybrid nanostructures, such as quantum dots, but also a solid starting point for further theoretical calculations to understand the fundamental properties of these materials.

Future perspectives

The Shockley–Queisser limit (SQ limit) sets the maximum solar conversion efficiency around 33.7% for a single p-n junction PV cell, assuming typical sunlight conditions (unconcentrated, AM 1.5 solar spectrum). The limit for organic-inorganic halide perovskite solar cells is believed to also be around 30%, however, some reports predict a more practical maximum PCE to be in the 25–27% range regardless of actual chemical composition, provided optimal band alignment is satisfied [180]. More, record efficiencies (>25.2%) are usually obtained on lab cells with small area (1 cm^2), therefore industrial upscaling is now a very active field. In fact in September of 2019, CEA-INES in Chambery announced a new world record of 20.3% for a 11.5 cm^2 perovskite PV module [181].

A substantial efficiency boost will be obtained by moving to advanced concepts beyond single-junction PV cells. These may include multi-exciton generation, singlet fission, hot-carrier collection and even intermediate band-gap cells [182]. In a tandem configuration, two materials with band-gaps E_{g1} and E_{g2} are combined, thus enabling the overall tandem cell to cover a wide spectral range. The tunability of the band-gap and high open-circuit voltages (V_{oc}) make perovskite solar cells ideal to combine with silicon in a multi-junction/tandem architectures, and to achieve efficiencies higher than 30% [183]. Naturally, all-perovskite tandem solar cells are equally feasible where the bottom cell is replaced with a perovskite absorber [184, 185].

On the other hand, we have also mentioned the hot-phonon bottleneck effect in HOPs. Cooling of photo-generated hot carriers in a classical semiconductor material dissipates the absorbed optical energy as lattice heat via LO phonon emission and decay. Thermalization by this mechanism leads to about 50% of the energy losses in a traditional single junction solar cell [186]. This mechanism is expected to be affected by the unique lattice structure and phonon properties of lead-halide perovskites, especially in the organic–inorganic hybrid types. Material engineering with the purpose of introducing overlapping acoustic and optical modes is likely be more important than opening a large phonon band gap. A strong phonon bottleneck effect is proposed in HOPs as a key mechanism to establish a long-lived hot carrier population, which is critical to achieve a working hot carrier PV device [187–189] and break the Shockley–Queisser limit [85] for PV energy conversion.

Furthermore, future research should focus on the reduction of parasitic non-radiative carrier recombination through strategies such as passivation and reduction of defects, as well as boosting efficiency through better-optimised interface materials. This is in big part because regardless of device configuration, solution-processed per-

ovskite films are polycrystalline and thus cannot avoid the formation of grain boundaries, which is an important factor influencing PV performance through the acceleration of electron–hole recombination. The deposited perovskite films tend also to have also high densities of crystalline defects, leading to ion migration through the perovskite film. Moreover, stronger J–V hysteresis was observed at grain boundaries than in grain interiors because of faster ion migration at the boundaries [190]. Typically, the active layer of a perovskite solar cell is deposited via spin coating of a precursor solution. A post-treatment with an antisolvent method is also common [191, 192]. However, solution-processed perovskite films are polycrystalline and the grain boundaries are believed to accelerate the electron–hole recombination. Some solutions have been explored based on the development of methods to control the crystal growth of perovskite films. For example, additives can be used to control cluster size in the precursor solution and modulate the nucleation rate. By slowing nucleation, the growth of large perovskite grains with higher crystallinity is facilitated [193–195]. Utilization of solvent annealing facilitates the diffusion of precursors and coarsening of small grains to form larger grains [196]. Other additives can also provide scaffold structures or nucleation sites to aid in producing uniform films or reducing external penetration [197]. Alternative deposition methods (*e.g.* vacuum flash-assisted deposition [198] and the Lewis acid–base adduct approach [199]) have also shown to allow high quality perovskite films to be prepared and recombination reduced.

However, the biggest issue for market implementation of perovskite based devices is still long-term instability and degradation. This has been shown to be due to external pathway factors, such as water, light, and oxygen [200] and also as a result of intrinsic instability, such as degradation upon heating because of the properties of the material [201]. The organic cations used in perovskite solar cells are very hygroscopic and ambient humidity can cause rapid degradation of perovskite films. Several strategies have been proposed in order to improve stability, a central one being material engineering. As mentioned before, many of the highest-efficiency systems published recently use mixed-cation and/or mixed halide perovskite systems. Lattice contraction by incorporating inorganic cations such as rubidium or caesium has been shown to improve both stability and efficiency [49]. Combining 2D-layered (Ruddlesden-Popper) perovskites with conventional 3D perovskites has enabled PCEs as high as 22% while showing enhanced operational stability, mainly due to improved resilience to moisture-induced degradation, over pure 3D perovskites [202–205]. Another key element of improving stability is device encapsulation. The rate of deterioration due to humidity increases when the latter

is combined with UV light, high temperatures, or the application of an electric field [206]. Movement towards UV-curable epoxies, photopolymer that downshift UV, hydroscopic and UV-stable interlayers and glass cover slips [207, 208] have significantly improved stability. These efforts have vastly improved the stability of perovskites since their initial introduction, and lifetimes are well on their way to meeting industrial standards.

References

[1] J.-P. Correa-Baena, M. Saliba, T. Buonassisi, M. Grätzel, A. Abate, W. Tress, and A. Hagfeldt, "Promises and challenges of perovskite solar cells," *Science*, vol. 358, pp. 739–744, nov 2017.

[2] H. Bilz and W. Kress, *Phonon dispersion relations in insulators*, vol. 10. Springer , Berlin, Heidelberg, 1978.

[3] M. I. Saidaminov, A. L. Abdelhady, G. Maculan, and O. M. Bakr, "Retrograde solubility of formamidinium and methylammonium lead halide perovskites enabling rapid single crystal growth," *Chemical Communications*, vol. 51, no. 100, pp. 17658–17661, 2015.

[4] J. Su, D. Chen, and C. Lin, "Growth of large CH3nh3pbx3 (x=i, br) single crystals in solution," *Journal of Crystal Growth*, vol. 422, pp. 75–79, jul 2015.

[5] S. Yakunin, L. Protesescu, F. Krieg, M. I. Bodnarchuk, G. Nedelcu, M. Humer, G. D. Luca, M. Fiebig, W. Heiss, and M. V. Kovalenko, "Low-threshold amplified spontaneous emission and lasing from colloidal nanocrystals of caesium lead halide perovskites," *Nature Communications*, vol. 6, aug 2015.

[6] T. J. Jacobsson, J.-P. Correa-Baena, M. Pazoki, M. Saliba, K. Schenk, M. Grätzel, and A. Hagfeldt, "Exploration of the compositional space for mixed lead halogen perovskites for high efficiency solar cells," *Energy & Environmental Science*, vol. 9, no. 5, pp. 1706–1724, 2016.

[7] D. M. Jang, K. Park, D. H. Kim, J. Park, F. Shojaei, H. S. Kang, J.-P. Ahn, J. W. Lee, and J. K. Song, "Reversible halide exchange reaction of organometal trihalide perovskite colloidal nanocrystals for full-range band gap tuning," *Nano Letters*, vol. 15, pp. 5191–5199, jul 2015.

[8] R. L. Milot, G. E. Eperon, H. J. Snaith, M. B. Johnston, and L. M. Herz, "Temperature-dependent charge-carrier dynamics in CH3nh3pbi3perovskite thin films," *Advanced Functional Materials*, vol. 25, pp. 6218–6227, sep 2015.

[9] J. Yang, X. Wen, H. Xia, R. Sheng, Q. Ma, J. Kim, P. Tapping, T. Harada, T. W. Kee, F. Huang, Y.-B. Cheng, M. Green, A. Ho-Baillie, S. Huang, S. Shrestha, R. Patterson, and G. Conibeer, "Acoustic-optical phonon up-conversion and hot-phonon bottleneck in lead-halide perovskites," *Nature Communications*, vol. 8, jan 2017.

[10] I. Anusca, S. Balčiūnas, P. Gemeiner, Š. Svirskas, M. Sanlialp, G. Lackner, C. Fettkenhauer, J. Belovickis, V. Samulionis, M. Ivanov, *et al.*, "Dielectric response: Answer to many questions in the methylammonium lead halide solar cell absorbers," *Advanced Energy Materials*, 2017.

[11] A. V. Humboldt, C. G. Ehrenberg, and G. Rose, "Theil 1: Mineralogisch-geognostische reise nach dem ural, dem altai und dem kaspischen meere. band 1: Reise nach dem nördlichen ural und dem altai," 1837.

[12] V. M. Goldschmidt, "Die gesetze der krystallochemie," *Die Naturwissenschaften*, vol. 14, pp. 477–485, may 1926.

[13] H. L. Wells, "Über die cäsium- und kalium-bleihalogenide," *Zeitschrift für anorganische Chemie*, vol. 3, no. 1, pp. 195–210, 1893.

[14] C. K. MØLLER, "A phase transition in cæsium plumbochloride," *Nature*, vol. 180, pp. 981–982, nov 1957.

[15] C. K. MØLLER, "Crystal structure and photoconductivity of cæsium plumbohalides," *Nature*, vol. 182, pp. 1436–1436, nov 1958.

[16] H. Thurnaurer and J. Deaderick, Oct. 21 1947 (filled 1941). U.S. Patent No. 2,429,588.

[17] E. Wainer and A. Salomon, "Electrical report no. 8 and 10, titanium alloy mfg," 1942, 1943.

[18] S. Ogawa, "On polymorphic change of barium titanate," *J Phys Soc Jpn*, vol. 1, pp. 32–33, 1946.

[19] B. M. Wul and I. M. Goldman, "Dielectric constants of titanates of metals of the second group," *Dokl. Mad. Nauk. SSSR*, vol. 46, 1945.

[20] B. M. Wul, "Dielectric constants of some titanates," *Nature*, vol. 156, pp. 480–480, oct 1945.

[21] H. D. Megaw, "Crystal structure of double oxides of the perovskite type," *Proceedings of the Physical Society*, vol. 58, pp. 133–152, mar 1946.

[22] S. Miyake and R. Ueda, "On polymorphic change of BaTiO3," *Journal of the Physical Society of Japan*, vol. 1, pp. 32–33, jan 1946.

[23] A. von Hippel, R. G. Breckenridge, F. G. Chesley, and L. Tisza, "High dielectric constant ceramics," *Industrial & Engineering Chemistry*, vol. 38, pp. 1097–1109, nov 1946.

[24] R. B. Gray, "Transducer and method of making the same," Nov. 1 1949. US Patent 2,486,560.

[25] H. Jaffe, "Titanate ceramics for electromechanical purposes," *Industrial & Engineering Chemistry*, vol. 42, pp. 264–268, feb 1950.

[26] L. Cross and R. Newnham, "History of ferroelectrics," *Ceramics and Civilization*, vol. 3, pp. 289–305, 1987.

[27] D. Weber, "CH3nh3pbx3, ein pb(II)-system mit kubischer perowskitstruktur / CH3nh3pbx3, a pb(II)-system with cubic perovskite structure," *Zeitschrift für Naturforschung B*, vol. 33, pp. 1443–1445, dec 1978.

[28] D. Weber, "CH3nh3snbrxi3-x (x = 0-3), ein sn(II)-system mit kubischer perowskitstruktur / CH3nh3snbrxi3-x(x = 0-3), a sn(II)-system with cubic perovskite structure," *Zeitschrift für Naturforschung B*, vol. 33, pp. 862–865, aug 1978.

[29] D. B. Mitzi, C. A. Feild, W. T. A. Harrison, and A. M. Guloy, "Conducting tin halides with a layered organic-based perovskite structure," *Nature*, vol. 369, pp. 467–469, jun 1994.

[30] D. B. Mitzi, S. Wang, C. A. Feild, C. A. Chess, and A. M. Guloy, "Conducting layered organic-inorganic halides containing ¡110¿-oriented perovskite sheets," *Science*, vol. 267, pp. 1473–1476, mar 1995.

[31] M. Era, S. Morimoto, T. Tsutsui, and S. Saito, "Electroluminescent device using two dimensional semiconductor (c6h5c2h4nh3)2pbi4 as an emitter," *Synthetic Metals*, vol. 71, pp. 2013–2014, apr 1995.

[32] T. Hattori, T. Taira, M. Era, T. Tsutsui, and S. Saito, "Highly efficient electroluminescence from a heterostructure device combined with emissive layered-perovskite and an electron-transporting organic compound," *Chemical Physics Letters*, vol. 254, pp. 103–108, may 1996.

[33] K. Chondroudis and D. B. Mitzi, "Electroluminescence from an organic-inorganic perovskite incorporating a quaterthiophene dye within lead halide perovskite layers," *Chemistry of Materials*, vol. 11, pp. 3028–3030, nov 1999.

[34] C. R. Kagan, "Organic-inorganic hybrid materials as semiconducting channels in thin-film field-effect transistors," *Science*, vol. 286, pp. 945–947, oct 1999.

[35] D. B. Mitzi, C. D. Dimitrakopoulos, and L. L. Kosbar, "Structurally tailored organic-inorganic perovskites: optical properties and solution-processed channel materials for thin-film transistors," *Chemistry of Materials*, vol. 13, pp. 3728–3740, oct 2001.

[36] D. Mitzi, C. Dimitrakopoulos, J. Rosner, D. Medeiros, Z. Xu, and C. Noyan, "Hybrid field-effect transistor based on a low-temperature melt-processed channel layer," *Advanced Materials*, vol. 14, pp. 1772–1776, dec 2002.

[37] A. Kojima, K. Teshima, Y. Shirai, and T. Miyasaka, "Organometal halide perovskites as visible-light sensitizers for photovoltaic cells," *Journal of the American Chemical Society*, vol. 131, pp. 6050–6051, may 2009.

[38] J.-H. Im, C.-R. Lee, J.-W. Lee, S.-W. Park, and N.-G. Park, "6.5% efficient perovskite quantum-dot-sensitized solar cell," *Nanoscale*, vol. 3, no. 10, p. 4088, 2011.

[39] M. M. Lee, J. Teuscher, T. Miyasaka, T. N. Murakami, and H. J. Snaith, "Efficient hybrid solar cells based on meso-superstructured organometal halide perovskites," *Science*, vol. 338, pp. 643–647, oct 2012.

[40] H.-S. Kim, C.-R. Lee, J.-H. Im, K.-B. Lee, T. Moehl, A. Marchioro, S.-J. Moon, R. Humphry-Baker, J.-H. Yum, J. E. Moser, M. Grätzel, and N.-G. Park, "Lead iodide perovskite sensitized all-solid-state submicron thin film mesoscopic solar cell with efficiency exceeding 9%," *Scientific Reports*, vol. 2, aug 2012.

[41] J. M. Ball, M. M. Lee, A. Hey, and H. J. Snaith, "Low-temperature processed meso-superstructured to thin-film perovskite solar cells," *Energy & Environmental Science*, vol. 6, no. 6, p. 1739, 2013.

[42] M. Liu, M. B. Johnston, and H. J. Snaith, "Efficient planar heterojunction perovskite solar cells by vapour deposition," *Nature*, vol. 501, pp. 395–398, sep 2013.

[43] G. E. Eperon, V. M. Burlakov, P. Docampo, A. Goriely, and H. J. Snaith, "Morphological control for high performance, solution-processed planar heterojunction perovskite solar cells," *Advanced Functional Materials*, vol. 24, pp. 151–157, sep 2013.

[44] M. Saliba, K. W. Tan, H. Sai, D. T. Moore, T. Scott, W. Zhang, L. A. Estroff, U. Wiesner, and H. J. Snaith, "Influence of thermal processing protocol upon the crystallization and photovoltaic performance of organic–inorganic lead trihalide perovskites," *The Journal of Physical Chemistry C*, vol. 118, pp. 17171–17177, apr 2014.

[45] W. S. Yang, J. H. Noh, N. J. Jeon, Y. C. Kim, S. Ryu, J. Seo, and S. I. Seok, "High-performance photovoltaic perovskite layers fabricated through intramolecular exchange," *Science*, vol. 348, pp. 1234–1237, may 2015.

[46] D. Bi, W. Tress, M. I. Dar, P. Gao, J. Luo, C. Renevier, K. Schenk, A. Abate, F. Giordano, J.-P. C. Baena, J.-D. Decoppet, S. M. Zakeeruddin, M. K. Nazeeruddin, M. Grätzel, and A. Hagfeldt, "Efficient luminescent solar cells based on tailored mixed-cation perovskites," *Science Advances*, vol. 2, p. e1501170, jan 2016.

[47] C. Momblona, L. Gil-Escrig, E. Bandiello, E. M. Hutter, M. Sessolo, K. Lederer, J. Blochwitz-Nimoth, and H. J. Bolink, "Efficient vacuum deposited p-i-n and n-i-p perovskite solar cells employing doped charge transport layers," *Energy Environ. Sci.*, vol. 9, no. 11, pp. 3456–3463, 2016.

[48] E. H. Anaraki, A. Kermanpur, L. Steier, K. Domanski, T. Matsui, W. Tress, M. Saliba, A. Abate, M. Grätzel, A. Hagfeldt, and J.-P. Correa-Baena, "Highly efficient and stable planar perovskite solar cells by solution-processed tin oxide," *Energy & Environmental Science*, vol. 9, no. 10, pp. 3128–3134, 2016.

[49] M. Saliba, T. Matsui, K. Domanski, J.-Y. Seo, A. Ummadisingu, S. M. Zakeeruddin, J.-P. Correa-Baena, W. R. Tress, A. Abate, A. Hagfeldt, and M. Gratzel, "Incorporation of rubidium cations into perovskite solar cells improves photovoltaic performance," *Science*, vol. 354, pp. 206–209, sep 2016.

[50] H. Tan, A. Jain, O. Voznyy, X. Lan, F. P. G. de Arquer, J. Z. Fan, R. Quintero-Bermudez, M. Yuan, B. Zhang, Y. Zhao, F. Fan, P. Li, L. N. Quan, Y. Zhao, Z.-H. Lu, Z. Yang, S. Hoogland, and E. H. Sargent, "Efficient and stable solution-processed planar perovskite solar cells via contact passivation," *Science*, vol. 355, pp. 722–726, feb 2017.

[51] S. S. Shin, E. J. Yeom, W. S. Yang, S. Hur, M. G. Kim, J. Im, J. Seo, J. H. Noh, and S. I. Seok, "Colloidally prepared la-doped BaSnO 3 electrodes for efficient, photostable perovskite solar cells," *Science*, vol. 356, pp. 167–171, mar 2017.

[52] W. S. Yang, B.-W. Park, E. H. Jung, N. J. Jeon, Y. C. Kim, D. U. Lee, S. S. Shin, J. Seo, E. K. Kim, J. H. Noh, and S. I. Seok, "Iodide management in formamidinium-lead-halide–based perovskite layers for efficient solar cells," *Science*, vol. 356, pp. 1376–1379, jun 2017.

[53] "NREL chart." http://www.nrel.gov/pv/assets/images/efficiency_chart.jpg. Accessed: 25.03.2017.

[54] H. Tsai, R. Asadpour, J.-C. Blancon, C. C. Stoumpos, O. Durand, J. W. Strzalka, B. Chen, R. Verduzco, P. M. Ajayan, S. Tretiak, J. Even, M. A. Alam, M. G. Kanatzidis, W. Nie, and A. D. Mohite, "Light-induced lattice expansion leads to high-efficiency perovskite solar cells," *Science*, vol. 360, pp. 67–70, apr 2018.

[55] K. A. Bush, A. F. Palmstrom, Z. J. Yu, M. Boccard, R. Cheacharoen, J. P. Mailoa, D. P. McMeekin, R. L. Z. Hoye, C. D. Bailie, T. Leijtens, I. M. Peters, M. C. Minichetti, N. Rolston, R. Prasanna, S. Sofia, D. Harwood, W. Ma, F. Moghadam, H. J. Snaith, T. Buonassisi, Z. C. Holman, S. F. Bent, and M. D. McGehee, "23.6%-efficient monolithic perovskite/silicon tandem solar cells with improved stability," *Nature Energy*, vol. 2, feb 2017.

[56] N. Onoda-Yamamuro, T. Matsuo, and H. Suga, "Calorimetric and IR spectroscopic studies of phase transitions in methylammonium trihalogenoplumbates (II)†," *Journal of Physics and Chemistry of Solids*, vol. 51, pp. 1383–1395, jan 1990.

[57] I. Swainson, R. Hammond, C. Soullière, O. Knop, and W. Massa, "Phase transitions in the perovskite methylammonium lead bromide, CH3nd3pbbr3," *Journal of Solid State Chemistry*, vol. 176, pp. 97–104, nov 2003.

[58] D. B. Mitzi, "Synthesis, structure, and properties of organic-inorganic perovskites and related materials," in *Progress in Inorganic Chemistry*, pp. 1–121, John Wiley & Sons, Inc., mar 1999.

[59] R. D. Shannon, "Revised effective ionic radii and systematic studies of interatomic distances in halides and chalcogenides," *Acta Crystallographica Section A*, vol. 32, pp. 751–767, sep 1976.

[60] M. Born and K. Huang, *Dynamical theory of crystal lattices*. Clarendon press, 1954.

[61] K. Aizu, "Theoretical investigation of the variety of first-order transitions between prototypic and ferroic phases," *Physical Review B*, vol. 23, pp. 1292–1303, feb 1981.

[62] P. Tolédano and J.-C. Tolédano, "Nonferroic phase transitions," *Physical Review B*, vol. 25, pp. 1946–1964, feb 1982.

[63] J.-C. Tolédano and P. Tolédano, "Order parameter symmetries and free-energy expansions for purely ferroelastic transitions," *Physical Review B*, vol. 21, pp. 1139–1172, feb 1980.

[64] C. J. Howard and H. T. Stokes, "Group-theoretical analysis of octahedral tilting in perovskites," *Acta Crystallographica Section B Structural Science*, vol. 54, pp. 782–789, dec 1998.

[65] H. T. Stokes, E. H. Kisi, D. M. Hatch, and C. J. Howard, "Group-theoretical analysis of octahedral tilting in ferroelectric perovskites," *Acta Crystallographica Section B Structural Science*, vol. 58, pp. 934–938, nov 2002.

[66] A. M. Glazer, "The classification of tilted octahedra in perovskites," *Acta Crystallographica Section B Structural Crystallography and Crystal Chemistry*, vol. 28, pp. 3384–3392, nov 1972.

[67] X.-H. Zhao, X.-C. Huang, S.-L. Zhang, D. Shao, H.-Y. Wei, and X.-Y. Wang, "Cation-dependent magnetic ordering and room-temperature bistability in azido-bridged perovskite-type compounds," *Journal of the American Chemical Society*, vol. 135, pp. 16006–16009, oct 2013.

[68] L. C. Gómez-Aguirre, B. Pato-Doldán, A. Stroppa, L.-M. Yang, T. Frauenheim, J. Mira, S. Yáñez-Vilar, R. Artiaga, S. Castro-García, M. Sánchez-Andújar, and M. A. Señarís-Rodríguez, "Coexistence of three ferroic orders in the multiferroic compound [(CH3)4 n][mn(n3)3] with perovskite-like structure," *Chemistry - A European Journal*, vol. 22, pp. 7863–7870, apr 2016.

[69] M. T. Weller, O. J. Weber, P. F. Henry, A. M. D. Pumpo, and T. C. Hansen, "Complete structure and cation orientation in the perovskite photovoltaic methylammonium lead iodide between 100 and 352 k," *Chemical Communications*, vol. 51, no. 20, pp. 4180–4183, 2015.

[70] C. C. Stoumpos, C. D. Malliakas, and M. G. Kanatzidis, "Semiconducting tin and lead iodide perovskites with organic cations: Phase transitions, high mobilities, and near-infrared photoluminescent properties," *Inorganic Chemistry*, vol. 52, pp. 9019–9038, jul 2013.

[71] J.-H. Lee, N. C. Bristowe, P. D. Bristowe, and A. K. Cheetham, "Role of hydrogen-bonding and its interplay with octahedral tilting in CH3nh3pbi3," *Chemical Communications*, vol. 51, no. 29, pp. 6434–6437, 2015.

[72] P. S. Whitfield, N. Herron, W. E. Guise, K. Page, Y. Q. Cheng, I. Milas, and M. K. Crawford, "Structures, phase transitions and tricritical behavior of the hybrid perovskite methyl ammonium lead iodide," *Scientific Reports*, vol. 6, oct 2016.

[73] E. C. Schueller, G. Laurita, D. H. Fabini, C. C. Stoumpos, M. G. Kanatzidis, and R. Seshadri, "Crystal structure evolution and notable thermal expansion in hybrid perovskites formamidinium tin iodide and formamidinium lead bromide," *Inorganic Chemistry*, vol. 57, pp. 695–701, dec 2017.

[74] A. A. Zhumekenov, M. I. Saidaminov, M. A. Haque, E. Alarousu, S. P. Sarmah, B. Murali, I. Dursun, X.-H. Miao, A. L. Abdelhady, T. Wu, O. F. Mohammed, and O. M. Bakr, "Formamidinium lead halide perovskite crystals with unprecedented long carrier dynamics and diffusion length," *ACS Energy Letters*, vol. 1, pp. 32–37, apr 2016.

[75] Q. Han, S.-H. Bae, P. Sun, Y.-T. Hsieh, Y. M. Yang, Y. S. Rim, H. Zhao, Q. Chen, W. Shi, G. Li, and Y. Yang, "Single crystal formamidinium lead iodide (FAPbI3): Insight into the structural, optical, and electrical properties," *Advanced Materials*, vol. 28, pp. 2253–2258, jan 2016.

[76] A. Binek, F. C. Hanusch, P. Docampo, and T. Bein, "Stabilization of the trigonal high-temperature phase of formamidinium lead iodide," *The Journal of Physical Chemistry Letters*, vol. 6, pp. 1249–1253, mar 2015.

[77] D. H. Fabini, C. C. Stoumpos, G. Laurita, A. Kaltzoglou, A. G. Kontos, P. Falaras, M. G. Kanatzidis, and R. Seshadri, "Reentrant structural and optical properties and large positive thermal expansion in perovskite formamidinium lead iodide," *Angewandte Chemie International Edition*, vol. 55, pp. 15392–15396, nov 2016.

[78] H.-H. Fang, F. Wang, S. Adjokatse, N. Zhao, J. Even, and M. A. Loi, "Photoexcitation dynamics in solution-processed formamidinium lead iodide perovskite thin films for solar cell applications," *Light: Science & Applications*, vol. 5, no. 4, p. e16056, 2016.

[79] M. T. Weller, O. J. Weber, J. M. Frost, and A. Walsh, "Cubic perovskite structure of black formamidinium lead iodide, α-[HC(NH2)2]PbI3, at 298 k," *The Journal of Physical Chemistry Letters*, vol. 6, pp. 3209–3212, aug 2015.

[80] G. P. O'Leary and R. G. Wheeler, "Phase transitions and soft librational modes in cubic crystals," *Physical Review B*, vol. 1, pp. 4409–4439, jun 1970.

[81] B. I. Swanson, "Displacive phase transformations in k2snbr6," *Physica Status Solidi (a)*, vol. 47, pp. K95–K98, may 1978.

[82] N. A. Benedek and C. J. Fennie, "Why are there so few perovskite ferroelectrics?," *The Journal of Physical Chemistry C*, vol. 117, pp. 13339–13349, may 2013.

[83] J. Even, L. Pedesseau, J.-M. Jancu, and C. Katan, "Importance of spin–orbit coupling in hybrid organic/inorganic perovskites for photovoltaic applications," *The Journal of Physical Chemistry Letters*, vol. 4, pp. 2999–3005, aug 2013.

[84] A. N. Beecher, O. E. Semonin, J. M. Skelton, J. M. Frost, M. W. Terban, H. Zhai, A. Alatas, J. S. Owen, A. Walsh, and S. J. L. Billinge, "Direct observation of dynamic symmetry breaking above room temperature in methylammonium lead iodide perovskite," *ACS Energy Letters*, vol. 1, pp. 880–887, oct 2016.

[85] W. Shockley and H. J. Queisser, "Detailed balance limit of efficiency of p-n junction solar cells," *Journal of Applied Physics*, vol. 32, pp. 510–519, mar 1961.

[86] P. Umari, E. Mosconi, and F. D. Angelis, "Relativistic GW calculations on CH3nh3pbi3 and CH3nh3sni3 perovskites for solar cell applications," *Scientific Reports*, vol. 4, mar 2014.

[87] F. Brivio, K. T. Butler, A. Walsh, and M. van Schilfgaarde, "Relativistic quasiparticle self-consistent electronic structure of hybrid halide perovskite photovoltaic absorbers," *Physical Review B*, vol. 89, apr 2014.

[88] J. Even, L. Pedesseau, and C. Katan, "Analysis of multivalley and multibandgap absorption and enhancement of free carriers related to exciton screening in hybrid perovskites," *The Journal of Physical Chemistry C*, vol. 118, pp. 11566–11572, may 2014.

[89] A. Miyata, A. Mitioglu, P. Plochocka, O. Portugall, J. T.-W. Wang, S. D. Stranks, H. J. Snaith, and R. J. Nicholas, "Direct measurement of the exciton binding energy and effective masses for charge carriers in organic–inorganic tri-halide perovskites," *Nature Physics*, vol. 11, pp. 582–587, jun 2015.

[90] M. Hirasawa, T. Ishihara, T. Goto, K. Uchida, and N. Miura, "Magnetoabsorption of the lowest exciton in perovskite-type compound (CH3nh3)PbI3," *Physica B: Condensed Matter*, vol. 201, pp. 427–430, jul 1994.

[91] K. Tanaka, T. Takahashi, T. Ban, T. Kondo, K. Uchida, and N. Miura, "Comparative study on the excitons in lead-halide-based perovskite-type crystals CH3nh3pbbr3 CH3nh3pbi3," *Solid State Communications*, vol. 127, pp. 619–623, sep 2003.

[92] S. D. Stranks, G. E. Eperon, G. Grancini, C. Menelaou, M. J. P. Alcocer, T. Leijtens, L. M. Herz, A. Petrozza, and H. J. Snaith, "Electron-hole diffusion lengths exceeding 1 micrometer in an organometal trihalide perovskite absorber," *Science*, vol. 342, pp. 341–344, oct 2013.

[93] M. A. Green, "Radiative efficiency of state-of-the-art photovoltaic cells," *Progress in Photovoltaics: Research and Applications*, vol. 20, pp. 472–476, sep 2011.

[94] F. Deschler, M. Price, S. Pathak, L. E. Klintberg, D.-D. Jarausch, R. Higler, S. Hüttner, T. Leijtens, S. D. Stranks, H. J. Snaith, M. Atatüre, R. T. Phillips, and R. H. Friend, "High photoluminescence efficiency and optically pumped lasing in solution-processed mixed halide perovskite semiconductors," *The Journal of Physical Chemistry Letters*, vol. 5, pp. 1421–1426, apr 2014.

[95] M. Lundstrom, *Fundamentals of carrier transport*. Cambridge university press, 2009.

[96] S. M. Sze and K. K. Ng, *Physics of semiconductor devices*. John wiley & sons, 2006.

[97] G. Xing, N. Mathews, S. Sun, S. S. Lim, Y. M. Lam, M. Gratzel, S. Mhaisalkar, and T. C. Sum, "Long-range balanced electron- and hole-transport lengths in organic-inorganic CH3nh3pbi3," *Science*, vol. 342, pp. 344–347, oct 2013.

[98] Q. Dong, Y. Fang, Y. Shao, P. Mulligan, J. Qiu, L. Cao, and J. Huang, "Electron-hole diffusion lengths $>$ 175 μm in solution-grown CH3nh3pbi3single crystals," *Science*, vol. 347, pp. 967–970, jan 2015.

[99] L. M. Herz, "Charge-carrier dynamics in organic-inorganic metal halide perovskites," *Annual Review of Physical Chemistry*, vol. 67, pp. 65–89, may 2016.

[100] J. Chen, D. Lee, and N.-G. Park, "Stabilizing the ag electrode and reducing j–v hysteresis through suppression of iodide migration in perovskite solar cells," *ACS Applied Materials & Interfaces*, vol. 9, pp. 36338–36349, oct 2017.

[101] E. Edri, S. Kirmayer, A. Henning, S. Mukhopadhyay, K. Gartsman, Y. Rosenwaks, G. Hodes, and D. Cahen, "Why lead methylammonium tri-iodide perovskite-based solar cells require a mesoporous electron transporting scaffold (but not necessarily a hole conductor)," *Nano Letters*, vol. 14, pp. 1000–1004, jan 2014.

[102] W. Pisula, X. Feng, and K. Müllen, "Charge-carrier transporting graphene-type molecules†," *Chemistry of Materials*, vol. 23, pp. 554–567, feb 2011.

[103] Y. Tamai, H. Ohkita, H. Benten, and S. Ito, "Exciton diffusion in conjugated polymers: From fundamental understanding to improvement in photovoltaic conversion efficiency," *The Journal of Physical Chemistry Letters*, vol. 6, pp. 3417–3428, aug 2015.

[104] T. M. Brenner, D. A. Egger, L. Kronik, G. Hodes, and D. Cahen, "Hybrid organic—inorganic perovskites: low-cost semiconductors with intriguing charge-transport properties," *Nature Reviews Materials*, vol. 1, jan 2016.

[105] C. Wehrenfennig, G. E. Eperon, M. B. Johnston, H. J. Snaith, and L. M. Herz, "High charge carrier mobilities and lifetimes in organolead trihalide perovskites," *Advanced Materials*, vol. 26, pp. 1584–1589, dec 2013.

[106] G. E. Eperon, S. D. Stranks, C. Menelaou, M. B. Johnston, L. M. Herz, and H. J. Snaith, "Formamidinium lead trihalide: a broadly tunable perovskite for efficient planar heterojunction solar cells," *Energy & Environmental Science*, vol. 7, no. 3, p. 982, 2014.

[107] D. Shi, V. Adinolfi, R. Comin, M. Yuan, E. Alarousu, A. Buin, Y. Chen, S. Hoogland, A. Rothenberger, K. Katsiev, Y. Losovyj, X. Zhang, P. A. Dowben, O. F. Mohammed, E. H. Sargent, and O. M. Bakr, "Low trap-state density and long carrier diffusion in organolead trihalide perovskite single crystals," *Science*, vol. 347, pp. 519–522, jan 2015.

[108] Z. Guo, J. S. Manser, Y. Wan, P. V. Kamat, and L. Huang, "Spatial and temporal imaging of long-range charge transport in perovskite thin films by ultrafast microscopy," *Nature Communications*, vol. 6, jun 2015.

[109] D. A. Valverde-Chávez, C. S. Ponseca, C. C. Stoumpos, A. Yartsev, M. G. Kanatzidis, V. Sundström, and D. G. Cooke, "Intrinsic femtosecond charge generation dynamics in single crystal CH3nh3pbi3," *Energy & Environmental Science*, vol. 8, no. 12, pp. 3700–3707, 2015.

[110] W. Rehman, R. L. Milot, G. E. Eperon, C. Wehrenfennig, J. L. Boland, H. J. Snaith, M. B. Johnston, and L. M. Herz, "Charge-carrier dynamics and mobilities in formamidinium lead mixed-halide perovskites," *Advanced Materials*, vol. 27, pp. 7938–7944, sep 2015.

[111] C. L. o vorakiat, T. Salim, J. Kadro, M.-T. Khuc, R. Haselsberger, L. Cheng, H. Xia, G. G. Gurzadyan, H. Su, Y. M. Lam, R. A. Marcus, M.-E. Michel-Beyerle, and E. E. M. Chia, "Elucidating the role of disorder and free-carrier recombination kinetics in CH3nh3pbi3 perovskite films," *Nature Communications*, vol. 6, jul 2015.

[112] C. S. Ponseca, T. J. Savenije, M. Abdellah, K. Zheng, A. Yartsev, T. Pascher, T. Harlang, P. Chabera, T. Pullerits, A. Stepanov, J.-P. Wolf, and V. Sundström, "Organometal halide perovskite solar cell materials rationalized: Ultrafast charge generation, high and microsecond-long balanced mobilities, and slow recombination," *Journal of the American Chemical Society*, vol. 136, pp. 5189–5192, mar 2014.

[113] E. M. Hutter, G. E. Eperon, S. D. Stranks, and T. J. Savenije, "Charge carriers in planar and meso-structured organic–inorganic perovskites: Mobilities, lifetimes, and concentrations of trap states," *The Journal of Physical Chemistry Letters*, vol. 6, pp. 3082–3090, jul 2015.

[114] M. I. Saidaminov, A. L. Abdelhady, B. Murali, E. Alarousu, V. M. Burlakov, W. Peng, I. Dursun, L. Wang, Y. He, G. Maculan, A. Goriely, T. Wu, O. F. Mohammed, and O. M. Bakr, "High-quality bulk hybrid perovskite single crystals within minutes by inverse temperature crystallization," *Nature Communications*, vol. 6, jul 2015.

[115] R. Sheng, A. Ho-Baillie, S. Huang, S. Chen, X. Wen, X. Hao, and M. A. Green, "Methylammonium lead bromide perovskite-based solar cells by vapor-assisted deposition," *The Journal of Physical Chemistry C*, vol. 119, pp. 3545–3549, feb 2015.

[116] O. E. Semonin, G. A. Elbaz, D. B. Straus, T. D. Hull, D. W. Paley, A. M. van der Zande, J. C. Hone, I. Kymissis, C. R. Kagan, X. Roy, and J. S. Owen, "Limits of carrier diffusion in n-type and p-type CH3nh3pbi3 perovskite single crystals," *The Journal of Physical Chemistry Letters*, vol. 7, pp. 3510–3518, aug 2016.

[117] D. H. Kim, J. Park, Z. Li, M. Yang, J.-S. Park, I. J. Park, J. Y. Kim, J. J. Berry, G. Rumbles, and K. Zhu, "300% enhancement of carrier mobility in uniaxial-oriented perovskite films formed by topotactic-oriented attachment," *Advanced Materials*, vol. 29, p. 1606831, apr 2017.

[118] H. Oga, A. Saeki, Y. Ogomi, S. Hayase, and S. Seki, "Improved understanding of the electronic and energetic landscapes of perovskite solar cells: High local charge carrier mobility, reduced recombination, and extremely shallow traps," *Journal of the American Chemical Society*, vol. 136, pp. 13818–13825, sep 2014.

[119] M. Karakus, S. A. Jensen, F. D'Angelo, D. Turchinovich, M. Bonn, and E. Cánovas, "Phonon–electron scattering limits free charge mobility in methylammonium lead iodide perovskites," *The Journal of Physical Chemistry Letters*, vol. 6, pp. 4991–4996, dec 2015.

[120] A. D. Wright, C. Verdi, R. L. Milot, G. E. Eperon, M. A. Pérez-Osorio, H. J. Snaith, F. Giustino, M. B. Johnston, and L. M. Herz, "Electron–phonon coupling in hybrid lead halide perovskites," *Nature Communications*, vol. 7, may 2016.

[121] J. Even, M. Carignano, and C. Katan, "Molecular disorder and translation/rotation coupling in the plastic crystal phase of hybrid perovskites," *Nanoscale*, vol. 8, no. 12, pp. 6222–6236, 2016.

[122] H. Zhu, K. Miyata, Y. Fu, J. Wang, P. P. Joshi, D. Niesner, K. W. Williams, S. Jin, and X.-Y. Zhu, "Screening in crystalline liquids protects energetic carriers in hybrid perovskites," *Science*, vol. 353, pp. 1409–1413, sep 2016.

[123] J. Timmermans, "Un nouvel état mésomorphe les cristaux organiques plastiques," *Journal de Chimie Physique*, vol. 35, pp. 331–344, 1938.

[124] L. D. Whalley, J. M. Skelton, J. M. Frost, and A. Walsh, "Phonon anharmonicity, lifetimes, and thermal transport in CH3nh3pbi3 from many-body perturbation theory," *Physical Review B*, vol. 94, dec 2016.

[125] G. L. Squires, *Introduction to the theory of thermal neutron scattering*. Dover Publications, 1966.

[126] S. W. Lovesey, "Theory of neutron scattering from condensed matter," 1984.

[127] https://www.nobelprize.org/prizes/physics/1994/press-release, 1994. Nobel prize press release.

[128] J. Chadwick, "Possible existence of a neutron," *Nature*, vol. 129, pp. 312–312, feb 1932.

[129] L. V. Hove, "Correlations in space and time and born approximation scattering in systems of interacting particles," *Physical Review*, vol. 95, pp. 249–262, jul 1954.

[130] B. Dorner, "The normalization of the resolution function for inelastic neutron scattering and its application," *Acta Crystallographica Section A*, vol. 28, pp. 319–327, jul 1972.

[131] P. Bourges, M. H. Lemée-Cailleau, P. Launois, C. Ecolivet, H. Cailleau, F. Moussa, and A. Mierzejewski, "Pretransitional dynamics of the structural phase transition in anthracene-TCNB: A comparison of raman-scattering and inelastic-neutron-scattering experiments," *Physical Review B*, vol. 54, pp. 15002–15015, dec 1996.

[132] http://www-llb.cea.fr/en/fr-en/spectros_p.php. LLB's instrument list.

[133] https://www.ill.eu/users/instruments/instruments-list/. ILL's instrument list.

[134] G. Shirane, S. M. Shapiro, and J. M. Tranquada, *Neutron Scattering with a Triple-Axis Spectrometer*. Cambridge University Press, 2002.

[135] J. R. D. Copley. Physica 136B (1986) xxvii-xxxi (North-Holland, Amsterdam).

[136] I. P. Swainson, C. Stock, S. F. Parker, L. V. Eijck, M. Russina, , and J. W. Taylor, "From soft harmonic phonons to fast relaxational dynamics in ch3nh3pbbr3," *Physical Review B*, vol. 92, no. 10, p. 100303(R), 2015.

[137] D. Halliday, R. Resnick, and J. Walker, *Fundamentals of Physics. 5th Extended*. Wiley, 1997.

[138] C. Zener, *Elasticity and anelasticity of metals*. University of Chicago, 1948.

[139] R. Comin, M. K. Crawford, A. H. Said, N. Herron, W. E. Guise, X. Wang, P. S. Whitfield, A. Jain, X. Gong, A. J. H. McGaughey, and E. H. Sargent, "Lattice dynamics and the nature of structural transitions in organolead halide perovskites," *Physical Review B*, vol. 94, sep 2016.

[140] M. Born, "On the stability of crystal lattices. i," *Mathematical Proceedings of the Cambridge Philosophical Society*, vol. 36, pp. 160–172, apr 1940.

[141] F. Mouhat and F.-X. Coudert, "Necessary and sufficient elastic stability conditions in various crystal systems," *Physical Review B*, vol. 90, no. 22, p. 224104, 2014.

[142] I. Vurgaftman, J. Meyer, and L. Ram-Mohan, "Band parameters for iii–v compound semiconductors and their alloys," *Journal of applied physics*, vol. 89, no. 11, pp. 5815–5875, 2001.

[143] I. P. Swainson, M. G. Tucker, D. J. Wilson, B. Winkler, and V. Milman, "Pressure response of an organic-inorganic perovskite: methylammonium lead bromide," *Chemistry of Materials*, vol. 19, pp. 2401–2405, may 2007.

[144] Y. Rakita, S. R. Cohen, N. K. Kedem, G. Hodes, and D. Cahen, "Mechanical properties of apbx3 (a= cs or ch3nh3; x= i or br) perovskite single crystals," *MRS Communications*, vol. 5, no. 4, pp. 623–629, 2015.

[145] G. A. Elbaz, W.-L. Ong, E. A. Doud, P. Kim, D. W. Paley, X. Roy, and J. A. Malen, "Phonon speed, not scattering, differentiates thermal transport in lead halide perovskites," *Nano Letters*, 2017.

[146] A. Létoublon, S. Paofai, B. Rufflé, P. Bourges, B. Hehlen, T. Michel, C. Ecolivet, O. Durand, S. Cordier, C. Katan, *et al.*, "Elastic constants, optical phonons, and molecular relaxations in the high temperature plastic phase of the ch3nh3pbbr3 hybrid perovskite," *The Journal of Physical Chemistry Letters*, vol. 7, no. 19, pp. 3776–3784, 2016.

[147] A. M. Lomonosov, X. Yan, C. Sheng, V. E. Gusev, C. Ni, and Z. Shen, "Exceptional elastic anisotropy of hybrid organic-inorganic perovskite CH3nh3pbbr3measured by laser ultrasonic technique," *physica status solidi (RRL) - Rapid Research Letters*, vol. 10, pp. 606–612, jul 2016.

[148] H. Z. Cummins, "Brillouin scattering spectroscopy of ferroelectric and ferroelastic phase transitions," *Philosophical Transactions of the Royal Society A: Mathematical, Physical and Engineering Sciences*, vol. 293, pp. 393–405, dec 1979.

[149] R. G. Chambers, *Electron in Metals and Semiconductors*. 1990.

[150] H. Diab, G. Trippé-Allard, F. Lédée, K. Jemli, C. Vilar, G. Bouchez, V. L. Jacques, A. Tejeda, J. Even, J.-S. Lauret, E. Deleporte, and D. Garrot, "Narrow linewidth excitonic emission in organic–inorganic lead iodide perovskite single crystals," *The Journal of Physical Chemistry Letters*, vol. 7, pp. 5093–5100, nov 2016.

[151] M. Wang and S. Lin, "Anisotropic and ultralow phonon thermal transport in organic–inorganic hybrid perovskites: Atomistic insights into solar cell thermal management and thermoelectric energy conversion efficiency," *Adv. Funct. Mater.*, vol. 26, pp. 5297–5306, 2016.

[152] A. Pisoni, J. Jaćimović, O. S. Barišić, M. Spina, R. Gaál, L. Forró, and E. Horváth, "Ultra-low thermal conductivity in organic–inorganic hybrid perovskite CH3nh3pbi3," *The Journal of Physical Chemistry Letters*, vol. 5, pp. 2488–2492, jul 2014.

[153] A. Kovalsky, L. Wang, G. T. Marek, C. Burda, and J. S. Dyck, "Thermal conductivity of ch3nh3pbi3 and cspbi3: Measuring the effect of the methylammonium ion on phonon scattering," *The Journal of Physical Chemistry C*, vol. 121, no. 6, pp. 3228–3233, 2017.

[154] Y. Yang, D. P. Ostrowski, R. M. France, K. Zhu, J. Van De Lagemaat, J. M. Luther, and M. C. Beard, "Observation of a hot-phonon bottleneck in lead-iodide perovskites," *Nature Photonics*, vol. 10, no. 1, pp. 53–59, 2016.

[155] A. Caretta, M. C. Donker, D. W. Perdok, D. Abbaszadeh, A. O. Polyakov, R. W. A. Havenith, T. T. M. Palstra, and P. H. M. van Loosdrecht, "Measurement of the acoustic-to-optical phonon coupling in multicomponent systems," *Physical Review B*, vol. 91, feb 2015.

[156] C. Katan, A. Mohite, and J. Even, "Entropy in halide perovskites," *Nature Materials*, vol. 17, pp. 377–379, April 2018.

[157] G. Schuck, F. Lehmann, J. Ollivier, H. Mutka, and S. Schorr, "Influence of chloride substitution on the rotational dynamics of methylammonium in mapbi$_{3-x}$cl$_x$ perovskites," *J. Phys. Chem. C*, vol. 213, pp. 11436–11446, 2019.

[158] Y. Fujii, S. Hoshino, Y. Yamada, and G. Shirane, "Neutron-scattering study on phase transitions of cspb cl 3," *Physical Review B*, vol. 9, no. 10, p. 4549, 1974.

[159] K. Drużbicki, R. S. Pinna, S. Rudić, M. Jura, G. Gorini, and F. Fernandez-Alonso, "Unexpected cation dynamics in the low-temperature phase of methylammonium lead iodide: The need for improved models," *The Journal of Physical Chemistry Letters*, vol. 7, pp. 4701–4709, nov 2016.

[160] B. Li, Y. Kawakita, Y. Liu, M. Wang, M. Matsuura, K. Shibata, S. Ohira-Kawamura, T. Yamada, S. Lin, K. Nakajima, and S. F. Liu, "Polar rotor scattering as atomic-level origin of low mobility and thermal conductivity of perovskite CH3nh3pbi3," *Nature Communications*, vol. 8, p. 16086, jun 2017.

[161] M. A. Carignano, S. A. Aravindh, I. S. Roqan, J. Even, and C. Katan, "Critical fluctuations and anharmonicity in lead iodide perovskites from molecular dynamics supercell simulations," *The Journal of Physical Chemistry C*, vol. 121, pp. 20729–20738, sep 2017.

[162] M. Fu, P. Tamarat, J.-B. Trebbia, M. I. Bodnarchuk, M. V. Kovalenko, J. Even, and B. Lounis, "Unraveling exciton–phonon coupling in individual FAPbI3 nanocrystals emitting near-infrared single photons," *Nature Communications*, vol. 9, aug 2018.

[163] D. J. Kubicki, D. Prochowicz, A. Hofstetter, P. Péchy, S. M. Zakeeruddin, M. Grätzel, and L. Emsley, "Cation dynamics in mixed-cation (MA)x(FA)1–xPbI3 hybrid perovskites from solid-state NMR," *Journal of the American Chemical Society*, vol. 139, pp. 10055–10061, jul 2017.

[164] A. Ferreira, A. Létoublon, S. Paofai, S. Raymond, C. Ecolivet, B. Rufflé, S. Cordier, C. Katan, M. Saidaminov, A. Zhumekenov, O. Bakr, J. Even, and P. Bourges, "Elastic softness of hybrid lead halide perovskites," *Physical Review Letters*, vol. 121, aug 2018.

[165] Y. Guo, O. Yaffe, T. D. Hull, J. S. Owen, D. R. Reichman, and L. E. Brus, "Polar rotor scattering as atomic-level origin of low mobility and thermal conductivity of perovskite $CH_3nh_3pbi_3$," *Nature Communications*, vol. 10, p. 1175, 2019.

[166] M. A. Pérez-Osorio, R. L. Milot, M. R. Filip, J. B. Patel, L. M. Herz, M. B. Johnston, and F. Giustino, "Vibrational properties of the organic–inorganic halide perovskite CH3nh3pbi3 from theory and experiment: Factor group analysis, first-principles calculations, and low-temperature infrared spectra," *The Journal of Physical Chemistry C*, vol. 119, pp. 25703–25718, nov 2015.

[167] S. Poncé, M. Schlipf, and F. Giustino, "Origin of low carrier mobilities in halide perovskites," *ACS Energy Letters*, vol. 4, pp. 456–463, jan 2019.

[168] N.-G. Park, "Perovskite solar cells: an emerging photovoltaic technology," *Materials Today*, vol. 18, no. 2, pp. 65–72, 2015.

[169] C. Quarti, G. Grancini, E. Mosconi, P. Bruno, J. M. Ball, M. M. Lee, H. J. Snaith, A. Petrozza, and F. D. Angelis, "The raman spectrum of the CH3nh3pbi3 hybrid perovskite: Interplay of theory and experiment," *The Journal of Physical Chemistry Letters*, vol. 5, pp. 279–284, dec 2013.

[170] L. Zhou, A. J. Neukirch, D. J. Vogel, D. S. Kilin, L. Pedesseau, M. A. Carignano, A. D. Mohite, J. Even, C. Katan, and S. Tretiak, "Density of states broadening in CH3nh3pbi3 hybrid perovskites understood from ab initio molecular dynamics simulations," *ACS Energy Letters*, vol. 3, pp. 787–793, mar 2018.

[171] H.-H. Fang, R. Raissa, M. Abdu-Aguye, S. Adjokatse, G. R. Blake, J. Even, and M. A. Loi, "Photophysics of organic-inorganic hybrid lead iodide perovskite single crystals," *Advanced Functional Materials*, vol. 25, pp. 2378–2385, feb 2015.

[172] H. Euchner, S. Pailhès, L. T. K. Nguyen, W. Assmus, F. Ritter, A. Haghighirad, Y. Grin, S. Paschen, and M. de Boissieu, "Phononic filter effect of rattling phonons in the thermoelectric clathrate $ba_8ge_{40+x}ni_{6+x}$," *Physical Review B*, vol. 86, p. 224003, 2012.

[173] G. A. Slack, *CRC Handbook of Thermoelectrics*. CRC Press, 1995.

[174] D. J. Voneshen, K. Refson, E. Borissenko, M. Krisch, A. Bosak, A. Piovano, E. Cemal, M. Enderle, M. J. Gutmann, M. Hoesch, M. Roger, L. Gannon, A. T. Boothroyd, S. Uthayakumar, D. G. Porter, and J. P. Goff, "Suppression of thermal conductivity by rattling modes in thermoelectric sodium cobaltate," *Nature Materials*, vol. 12, pp. 1028–1032, aug 2013.

[175] K. Miyata, T. L. Atallah, and X.-Y. Zhu, "Lead halide perovskites: Crystal-liquid duality, phonon glass electron crystals, and large polaron formation," *Science Advances*, vol. 3, p. e1701469, oct 2017.

[176] D. G. Cahill and R. O. Pohl, "Lattice vibrations and heat transport in crystals and glasses," *Annual Review of Physical Chemistry*, vol. 39, pp. 93–121, oct 1988.

[177] M. Li, J. Fu, Q. Xu, and T. C. Sum, "Slow hot-carrier cooling in halide perovskites: Prospects for hot-carrier solar cells," *Advanced Materials*, p. 1802486, jan 2019.

[178] S. Kahmann and M. A. Loi, "Hot carrier solar cells and the potential of perovskites for breaking the shockley–queisser limit," *Journal of Materials Chemistry C*, vol. 7, no. 9, pp. 2471–2486, 2019.

[179] M. Songvilay, M. Bari, Z.-G. Ye, G. Xu, P. M. Gehring, W. D. Ratcliff, K. Schmalzl, F. Bourdarot, B. Roessli, and C. Stock, "Lifetime shortened acoustic phonons and static order at the brillouin zone boundary in the organic-inorganic perovskite ch3nh3pbcl3," *Physical Review Materials*, vol. 2, p. 123601, Dec 2018.

[180] O. Grånäs, D. Vinichenko, and E. Kaxiras, "Establishing the limits of efficiency of perovskite solar cells from first principles modeling," *Scientific Reports*, vol. 6, nov 2016.

[181] "CEA-INES new record for perovskite module technology." http://liten.cea.fr/cea-tech/liten/en/Pages/News/2019/New-record-for-Perovskite-Module-technology.aspx. Accessed: 11.2019.

[182] M. A. Green, "Third generation photovoltaics: solar cells for 2020 and beyond," *Physica E: Low-dimensional Systems and Nanostructures*, vol. 14, pp. 65–70, apr 2002.

[183] Q. Wali, N. K. Elumalai, Y. Iqbal, A. Uddin, and R. Jose, "Tandem perovskite solar cells," *Renewable and Sustainable Energy Reviews*, vol. 84, pp. 89–110, mar 2018.

[184] D. Forgács, L. Gil-Escrig, D. Pérez-Del-Rey, C. Momblona, J. Werner, B. Niesen, C. Ballif, M. Sessolo, and H. J. Bolink, "Efficient monolithic perovskite/perovskite tandem solar cells," *Advanced Energy Materials*, vol. 7, p. 1602121, dec 2016.

[185] D. Zhao, Y. Yu, C. Wang, W. Liao, N. Shrestha, C. R. Grice, A. J. Cimaroli, L. Guan, R. J. Ellingson, K. Zhu, X. Zhao, R.-G. Xiong, and Y. Yan, "Low-bandgap mixed tin–lead iodide perovskite absorbers with long carrier lifetimes for all-perovskite tandem solar cells," *Nature Energy*, vol. 2, mar 2017.

[186] A. P. Kirk and M. V. Fischetti, "Fundamental limitations of hot-carrier solar cells," *Physical Review B*, vol. 86, oct 2012.

[187] R. T. Ross and A. J. Nozik, "Efficiency of hot-carrier solar energy converters," *Journal of Applied Physics*, vol. 53, pp. 3813–3818, may 1982.

[188] G. Conibeer, N. Ekins-Daukes, J.-F. Guillemoles, D. Kőnig, E.-C. Cho, C.-W. Jiang, S. Shrestha, and M. Green, "Progress on hot carrier cells," *Solar Energy Materials and Solar Cells*, vol. 93, pp. 713–719, jun 2009.

[189] D. König, K. Casalenuovo, Y. Takeda, G. Conibeer, J. Guillemoles, R. Patterson, L. Huang, and M. Green, "Hot carrier solar cells: Principles, materials and design," *Physica E: Low-dimensional Systems and Nanostructures*, vol. 42, pp. 2862–2866, sep 2010.

[190] Y. Shao, Y. Fang, T. Li, Q. Wang, Q. Dong, Y. Deng, Y. Yuan, H. Wei, M. Wang, A. Gruverman, J. Shield, and J. Huang, "Grain boundary dominated ion migration in polycrystalline organic–inorganic halide perovskite films," *Energy & Environmental Science*, vol. 9, no. 5, pp. 1752–1759, 2016.

[191] N. J. Jeon, J. H. Noh, Y. C. Kim, W. S. Yang, S. Ryu, and S. I. Seok, "Solvent engineering for high-performance inorganic–organic hybrid perovskite solar cells," *Nature Materials*, vol. 13, pp. 897–903, jul 2014.

[192] M. Xiao, F. Huang, W. Huang, Y. Dkhissi, Y. Zhu, J. Etheridge, A. Gray-Weale, U. Bach, Y.-B. Cheng, and L. Spiccia, "A fast deposition-crystallization procedure for highly efficient lead iodide perovskite thin-film solar cells," *Angewandte Chemie International Edition*, vol. 53, pp. 9898–9903, jul 2014.

[193] J.-H. Im, I.-H. Jang, N. Pellet, M. Grätzel, and N.-G. Park, "Growth of CH3nh3pbi3 cuboids with controlled size for high-efficiency perovskite solar cells," *Nature Nanotechnology*, vol. 9, pp. 927–932, aug 2014.

[194] J.-W. Lee, H.-S. Kim, and N.-G. Park, "Lewis acid–base adduct approach for high efficiency perovskite solar cells," *Accounts of Chemical Research*, vol. 49, pp. 311–319, jan 2016.

[195] J.-W. Lee, S.-H. Bae, Y.-T. Hsieh, N. D. Marco, M. Wang, P. Sun, and Y. Yang, "A bifunctional lewis base additive for microscopic homogeneity in perovskite solar cells," *Chem*, vol. 3, pp. 290–302, aug 2017.

[196] Z. Xiao, Q. Dong, C. Bi, Y. Shao, Y. Yuan, and J. Huang, "Solvent annealing of perovskite-induced crystal growth for photovoltaic-device efficiency enhancement," *Advanced Materials*, vol. 26, pp. 6503–6509, aug 2014.

[197] S. Emami, L. Andrade, and A. Mendes, "Recent progress in long-term stability of perovskite solar cells," *U.Porto Journal of Engineering*, vol. 1, pp. 52–62, mar 2018.

[198] X. Li, D. Bi, C. Yi, J.-D. Décoppet, J. Luo, S. M. Zakeeruddin, A. Hagfeldt, and M. Grätzel, "A vacuum flash–assisted solution process for high-efficiency large-area perovskite solar cells," *Science*, vol. 353, pp. 58–62, jun 2016.

[199] N. Ahn, D.-Y. Son, I.-H. Jang, S. M. Kang, M. Choi, and N.-G. Park, "Highly reproducible perovskite solar cells with average efficiency of 18.3% and best efficiency of 19.7% fabricated via lewis base adduct of lead(II) iodide," *Journal of the American Chemical Society*, vol. 137, pp. 8696–8699, jul 2015.

[200] T. A. Berhe, W.-N. Su, C.-H. Chen, C.-J. Pan, J.-H. Cheng, H.-M. Chen, M.-C. Tsai, L.-Y. Chen, A. A. Dubale, and B.-J. Hwang, "Organometal halide perovskite solar cells: degradation and stability," *Energy & Environmental Science*, vol. 9, no. 2, pp. 323–356, 2016.

[201] H. J. Snaith, "Present status and future prospects of perovskite photovoltaics," *Nature Materials*, vol. 17, pp. 372–376, apr 2018.

[202] Y. Liu, S. Akin, L. Pan, R. Uchida, N. Arora, J. V. Milić, A. Hinderhofer, F. Schreiber, A. R. Uhl, S. M. Zakeeruddin, A. Hagfeldt, M. I. Dar, and M. Grätzel, "Ultrahydrophobic 3d/2d fluoroarene bilayer-based water-resistant perovskite solar cells with efficiencies exceeding 22%," *Science Advances*, vol. 5, p. eaaw2543, jun 2019.

[203] Z. Ahmad, T. Noma, S. Paek, K. T. Cho, D. Taguchi, M. Iwamoto, T. Manaka, M. K. Nazeeruddin, F. Touati, and S. A. Al-Muhtaseb, "Stability in 3d and 2d/3d hybrid perovskite solar cells studied by EFISHG and IS techniques under light and heat soaking," *Organic Electronics*, vol. 66, pp. 7–12, mar 2019.

[204] J.-W. Lee, Z. Dai, T.-H. Han, C. Choi, S.-Y. Chang, S.-J. Lee, N. D. Marco, H. Zhao, P. Sun, Y. Huang, and Y. Yang, "2d perovskite stabilized phase-pure formamidinium perovskite solar cells," *Nature Communications*, vol. 9, aug 2018.

[205] M.-H. Li, H.-H. Yeh, Y.-H. Chiang, U.-S. Jeng, C.-J. Su, H.-W. Shiu, Y.-J. Hsu, N. Kosugi, T. Ohigashi, Y.-A. Chen, P.-S. Shen, P. Chen, and T.-F. Guo, "Highly efficient 2d/3d hybrid perovskite solar cells via low-pressure vapor-assisted solution process," *Advanced Materials*, vol. 30, p. 1801401, jun 2018.

[206] A. Rajagopal, K. Yao, and A. K.-Y. Jen, "Toward perovskite solar cell commercialization: A perspective and research roadmap based on interfacial engineering," *Advanced Materials*, vol. 30, p. 1800455, jun 2018.

[207] M. Wong-Stringer, O. S. Game, J. A. Smith, T. J. Routledge, B. A. Alqurashy, B. G. Freestone, A. J. Parnell, N. Vaenas, V. Kumar, M. O. A. Alawad, A. Iraqi, C. Rodenburg, and D. G. Lidzey, "High-performance multilayer encapsulation for perovskite photovoltaics," *Advanced Energy Materials*, vol. 8, p. 1801234, jul 2018.

[208] F. Bella, G. Griffini, J.-P. Correa-Baena, G. Saracco, M. Gratzel, A. Hagfeldt, S. Turri, and C. Gerbaldi, "Improving efficiency and stability of perovskite solar cells with photocurable fluoropolymers," *Science*, vol. 354, pp. 203–206, sep 2016.

[209] N. W. Ashcroft, N. D. Mermin, *et al.*, *Solid state physics*. New York: Holt, Rinehart and Winston„ 1976.

Appendices

Appendix A

Crystal lattices and reciprocal space

The atoms in a crystal can be mathematically represented as points in a three-dimensional (3D) real space lattice. If these lattice points are arranged in a periodic fashion, then one can define real space unit cell in terms of three non-coplanar basic vectors $\boldsymbol{a}$, $\boldsymbol{b}$ and $\boldsymbol{c}$ and the angles α, β, and γ (see Fig. A1). In diffraction experiments using crystalline samples, atoms are arranged in a highly ordered fashion with specific periodic positions and symmetry. All atoms are equivalent when they follow the periodicity. For a reference or origin located at any of these atoms, the crystal is exactly the same. Their relative position can then be described by the translational vector $\mathbf{T}$ defined as

$$\mathbf{T} = n_1\mathbf{a} + n_2\mathbf{b} + n_3\mathbf{c} \tag{A.1}$$

where the integers n_1, n_2 and n_3 are also known as cell indices and frequently denoted for brevity by the single letter n. If the unit cell contains just one lattice site, so that the lattice vectors n give every lattice site in the crystal, then we have a Bravais lattice. There are in total 14 Bravais lattices [209] which come from 7 different lattice systems. The simple cubic, face-centered cubic (FCC) and the body-centered cubic (BCC), which are represented in Fig. A1.b,c,d, make up the cubic lattice system. The remaining six are the hexagonal, triclinic, trigonal, monoclinic (two Bravais types), orthorhombic (four types) and tetragonal (two types) systems. See **Table A.1** for all 14 Bravais lattices and their basic properties. In general crystal lattices have more than on atom per unit cell

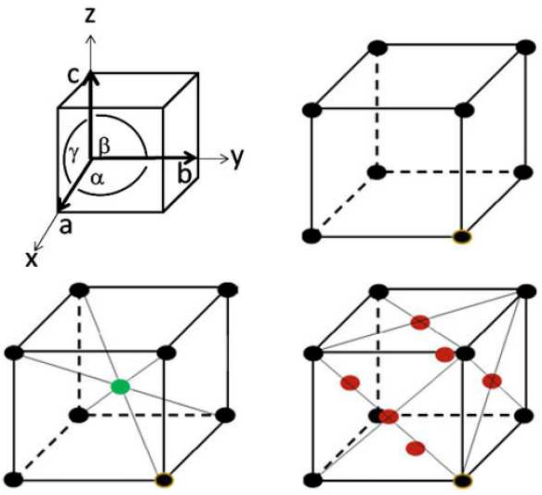

Figure A1: (a) The three basic vectors $\boldsymbol{a}$, $\boldsymbol{b}$ and $\boldsymbol{c}$ and the angles between a pair of vectors, α, β, and γ. Three lattices of the cubic system, namely the (b) simple cubic, (c) face-centered cubic (FCC) and (d) body-centered cubic (BCC).

Table A.1: The 14 bravais lattices.

System	Cell axes and angles	Number of lattices
Cubic	a = b = c $\alpha = \beta = \gamma = 90°$	3
Hexagonal	a = b ≠ c $\alpha = \beta = 90°$, $\gamma = 120°$	1
Triclinic	a ≠ b ≠ c $\alpha \neq \beta \neq \gamma$	1
Trigonal	a = b = c $\alpha = \beta = \gamma > 120°, \neq 90°$	1
Monoclinic	a ≠ b ≠ c $\alpha = \gamma = 90° \neq \beta$	2
Tetragonal	a = b ≠ c $\alpha = \beta = \gamma = 90°$	2
Orthorhombic	a ≠ b ≠ c $\alpha = \beta = \gamma = 90°$	4

and are constructed from several interpenetrating identical Bravais lattices. The positions of the r atoms within a unit cell are denoted by the vectors $\mathbf{d}$, which can be defined in terms of the basic $\boldsymbol{a}$, $\boldsymbol{b}$ and $\boldsymbol{c}$ vectors

$$\mathbf{d} = d_1\mathbf{a} + d_2\mathbf{b} + d_3\mathbf{c} \tag{A.2}$$

with $0 \leqslant \mathrm{d}_i \leqslant 1$, $i = 1, 2, 3$, the site d = 0 coinciding with the corner of the unit cell. The position vector $\mathbf{R}_{td}$ of an atom in the crystal will then be given by

$$\mathbf{R}_{td} = \mathbf{T} + \mathbf{d} \tag{A.3}$$

A lattice plane of a given Bravais lattice is any plane containing at least three noncollinear Bravais lattice points. Alternatively, it can be interpreted as a plane (or family of parallel planes) whose intersections with the lattice are periodic and intersect the Bravais lattice. One can easily define a lattice plane by taking a lattice point as a reference and then choosing the lattice vector joining a point away from the reference and along the line in a direction $\mathbf{T} = n_1\mathbf{a} + n_2\mathbf{b} + n_3\mathbf{c}$. The direction of a plane being the integral triplet $[n_1 n_2 n_3]$. For example, if we choose 0 as the reference and a lattice point at 1a, 1b, and 1c, then $\mathbf{T} = 1\mathbf{a} + 1\mathbf{b} + 1\mathbf{c}$ and the direction is [111]. The most typical notation system in crystallography for planes in crystal lattices is the Miller index. The orientation of a plane can be specified by the Miller indices (hkl). Fig. A2 illustrate the examples of (002), (110), (011), and (111). All planes, even non-parallel ones, that through rotational symmetry are equivalent to the plane (hkl), are represented by {hkl}, which defines the (hkl) family of planes. Again as an example, the $(\bar{1}00)$, $(0\bar{1}0)$, $(00\bar{1})$ planes are parallel

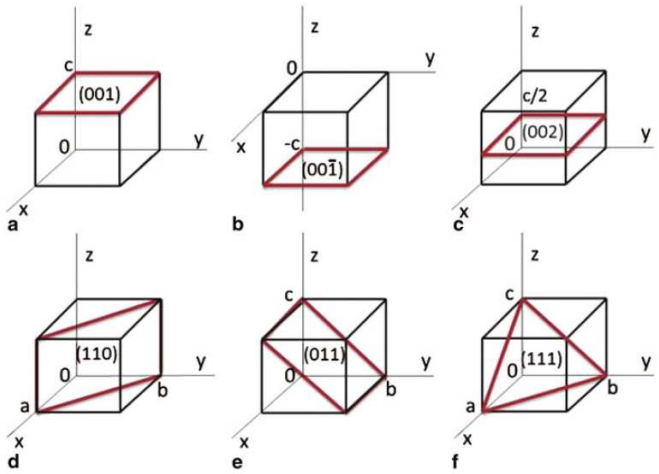

Figure A2: Various planes in a cubic lattice: (a) The (001) plane; (b) (00$\bar{1}$) plane; (c) (002) plane; (d) (110) plane; (e) (011) plane and (f) (111) plane.

to (100), (010), and (001), respectively, and so these six planes can be labelled as {100}. This is important because most diffraction experiments involve the scattering of waves from a family of equivalent planes, not just one single plane. In Fig. A1, a unit cell in real space was illustrated, with basic vectors a, b, and c. Analogously, we can also define a reciprocal lattice vector $\mathbf{G}(hkl)$ as

$$\mathbf{G}(hkl) = h\mathbf{a}^* + k\mathbf{b}^* + l\mathbf{c}^* \tag{A.4}$$

where h, k, and l are the Miller indices of a crystal plane (hkl) and $\mathbf{a}^*$, $\mathbf{b}^*$, and $\mathbf{c}^*$ are the reciprocal unit vectors. One can then show that $\mathbf{G}(hkl) \bullet \mathbf{T}$ is always an integer

$$(h\mathbf{a}^* + k\mathbf{b}^* + l\mathbf{c}^*) \bullet (n_1\mathbf{a} + n_2\mathbf{b} + n_3\mathbf{c}) = \text{integer} \tag{A.5}$$

From vector algebra, when the previous equation is satisfied, one obtains the reciprocal lattice vectors

$$\mathbf{a}^* = 2\pi\frac{\mathbf{b}\times\mathbf{c}}{V},\ \mathbf{b}^* = 2\pi\frac{\mathbf{c}\times\mathbf{a}}{V},\ \mathbf{c}^* = 2\pi\frac{\mathbf{a}\times\mathbf{b}}{V}, \tag{A.6}$$

Where $\mathrm{V} = \mathbf{a}\cdot(\mathbf{b}\times\mathbf{c})$ is the volume of a unit cell in real space. This means, for example, that vector $\mathbf{a}^*$ is perpendicular to the plane consisting of $\mathbf{b}$ and $\mathbf{c}$. At the same time, the magnitude of $\mathbf{a}^*$ is inversely proportional to the magnitude of $\mathbf{a}$, implying that the size of a reciprocal lattice unit cell is inversely proportional to the size of the real space unit cell.

Basically, the reciprocal lattice corresponds to the Fourier transform of a Bravais lattice. While the Bravais lattice exists in real-space and is what one would commonly understand as a physical lattice, the reciprocal lattice exists in reciprocal space, or **Q**-space. This symmetry relationship between both spaces will is also described via the basics of scattering theory in Chapter 2.

Appendix B

Results: supplementary figures

B.1 Elastic softness of hybrid lead halide perovskites

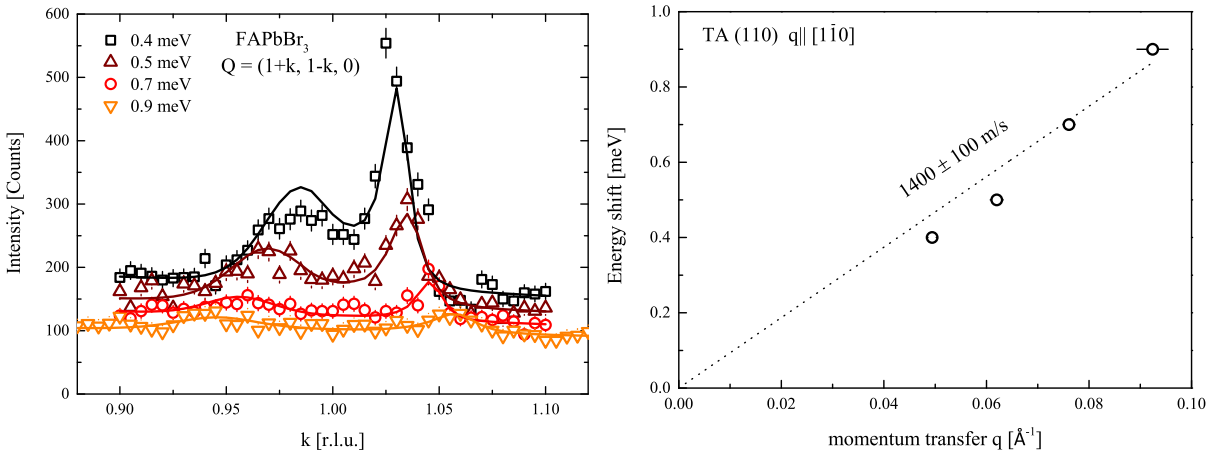

Figure B1: (a) TA phonon spectra in $FAPbBr_3$, for different energy values around the (110) Bragg peak. To access the T2 branch, measurements were made along [1$\bar{1}$0] with a scattering plane of [100][010]. (b) Dispersion curve for the same phonons.

B.2 Direct evidence of weakly dispersed optical phonon at low temperature

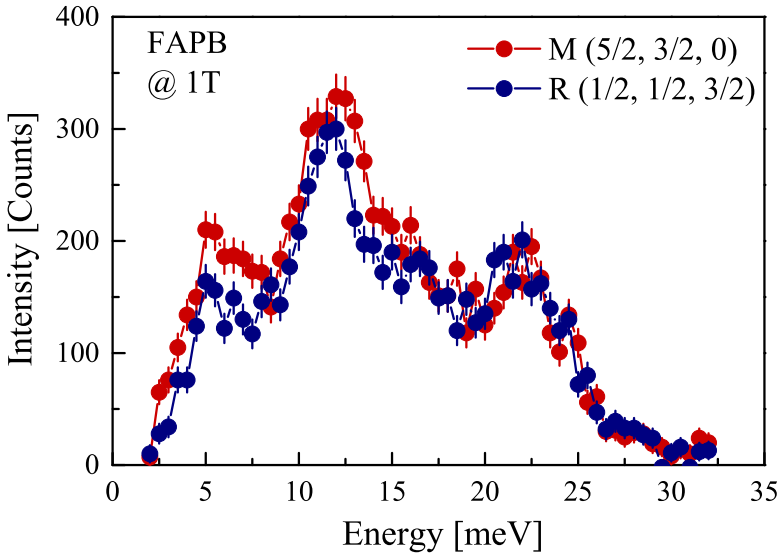

Figure B2: Optical phonon spectra, measured by TAS inelastic neutron scattering at low temperature (5 K), in $FAPbBr_3$ at the R (1/2 1/2 3/2) and M (5/2 3/2 0) Bragg points. Only a small negligible difference (in amplitude) is seen between the spectra of both points, illustrating the weak dispersion nature of the phonon modes.

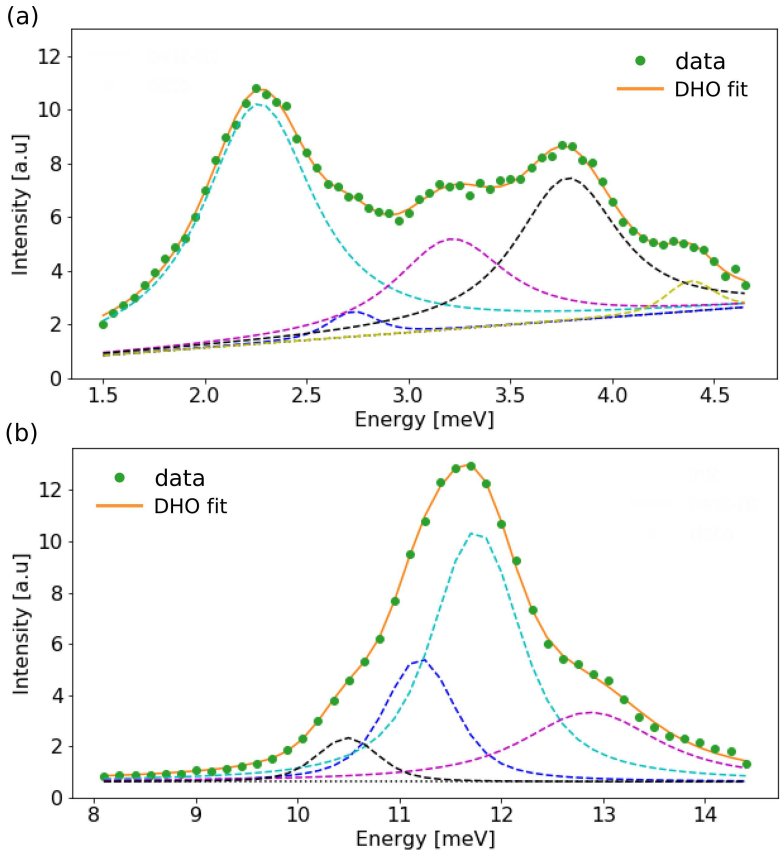

Figure B3: 1D cuts of the ToF mapping of MAPI, at Q = (002), between (a) 1.5-4.6 meV and (b) 8-14.5 meV. The data (green scatter points) is fitted (orange line) with a sum of a sum of DHOs (Eq. 2.38, section X).

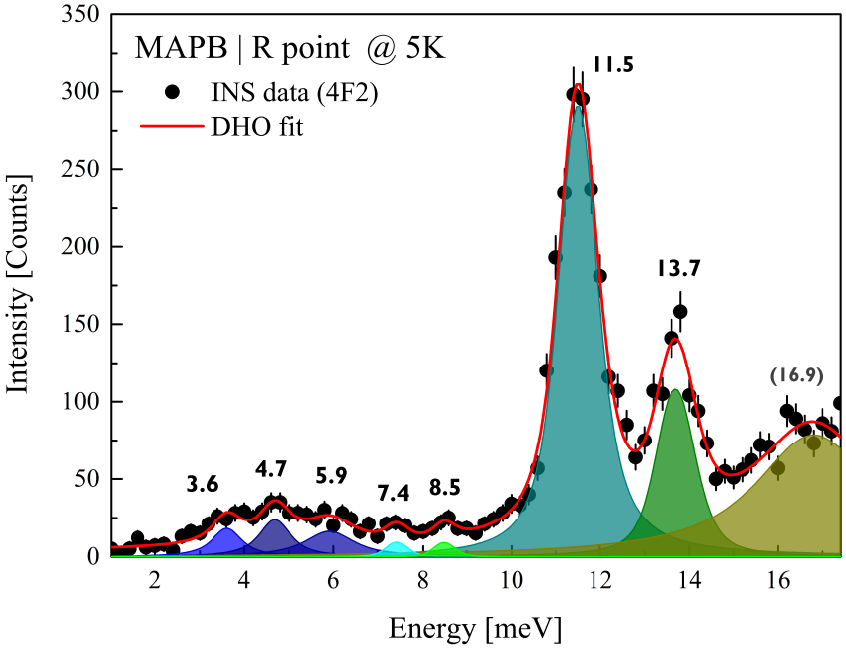

Figure B4: Optical phonon spectra, measured by TAS inelastic neutron scattering at low temperature (5 K), in $MAPbBr_3$ at the R (1/2 1/2 3/2). The experimental INS data (black scatter points) is fitted (red line) with a sum of DHOs (Eq. 2.38, section 2.2.5) and is presented with a removed background.

B.3 Temperature behaviour of lattice dynamics and phase transitions

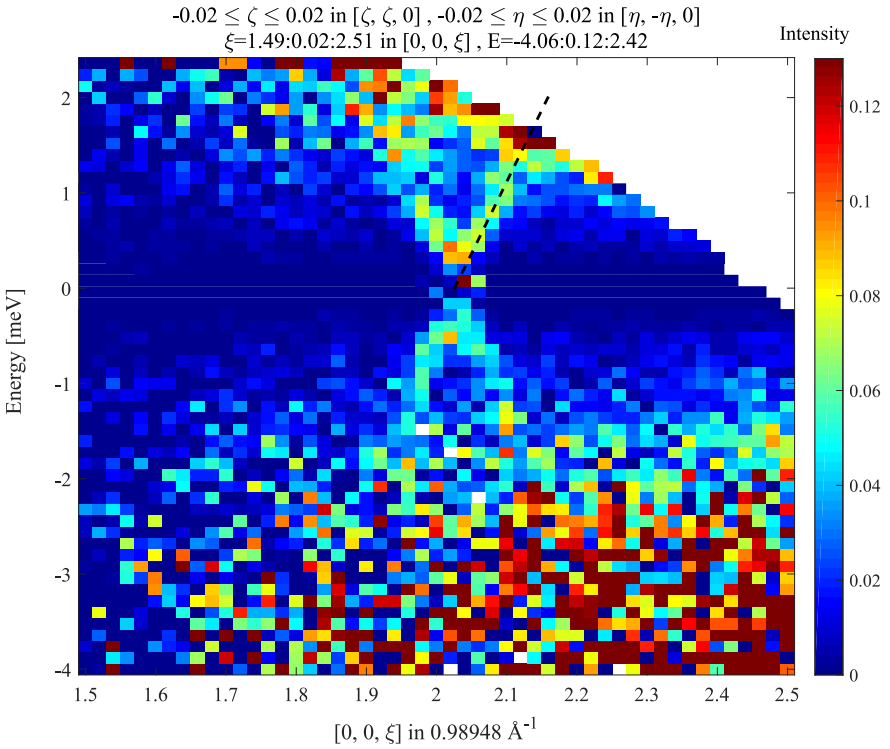

Figure B5: ToF neutron spectra measured at room temperature in $MAPbI_3$. Longitudinal acoustic (LA) phonons around the 002 Bragg reflection are clearly seen up to energies of ∼2 meV. The slope (dashed line), corresponding to the sound velocity from the previously reported dispersion curves of the same LA phonons (Fig. 3.2), is also plotted for comparison.

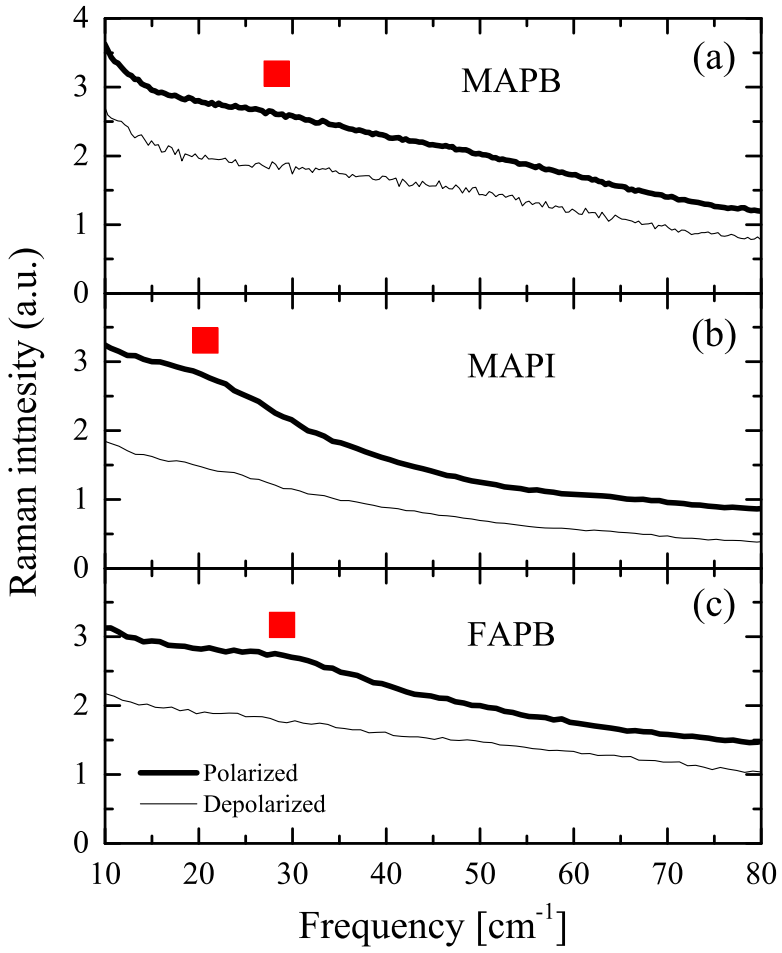

Figure B6: Comparison between the polarized and depolarized Raman spectra at room temperature for (a) MAPB and (c) FAPB, and at 353 K for (b) MAPI. The red square indicates approximately the position of the lowest frequency mode ω_1.

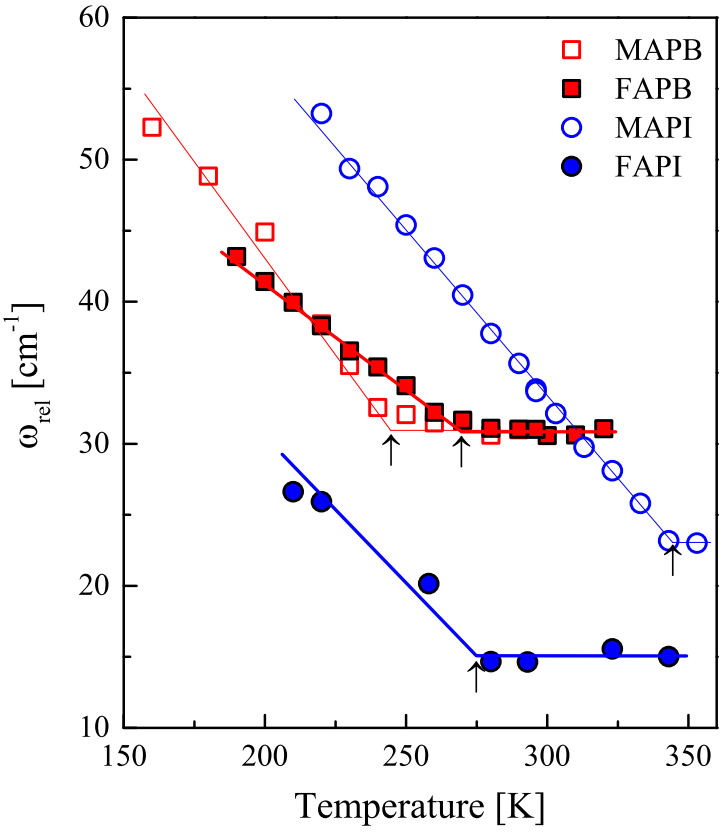

Figure B7: Relaxational frequencies $\omega_{rel} = \omega_0^2/\Gamma$ of the lowest frequency Raman mode ω_1, in $MAPbBr_3$, $MAPbI_3$, $FAPbBr_3$ and $FAPbI_3$, as a function of temperature. The cubic-tetragonal transitions are marked (arrows), appearing to be of a less abrupt nature in Br-based samples, suggesting pre-transitional effects.

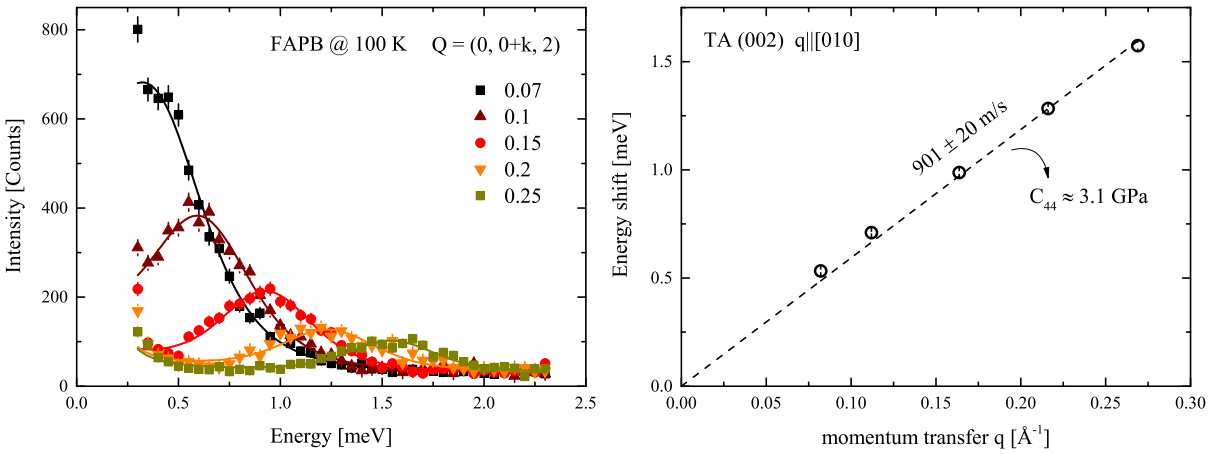

Figure B8: (a) TA phonon spectra in $FAPbBr_3$ at 100 K, for different Q positions going away from the (002) Bragg peak, along the [010]. (b) Dispersion curve for the same phonons.

Titre : Propriétés structurales et dynamiques des pérovskites hybrides organo-plombiques pour les applications photovoltaïques

Mots clés : Pérovskites hybrides ; Photovoltaïque ; Spectroscopie ; Diffraction ; Neutrons

Resumé : Ce projet se concentre sur l'étude de pérovskites hybrides organo-plombiques (HOP), à savoir $MAPbBr_3$, $MAPbI_3$, $FAPbBr_3$ et α-$FAPbI_3$. Pour ce faire, nous nous appuyons beaucoup sur la spectroscopie de diffusion inélastique de neutrons (INS), car elle permet de sonder systématiquement les propriétés structurales de ces matériaux. Avec ça, nous pouvons présenter une étude détaillée des excitations de réseau cristallin (phonons) dans les quatre composés HOP les plus pertinents sur le plan technologique dans le domaine du photovoltaïque. En mesurant les courbes de dispersion des phonons acoustiques, nous donnons une image claire de la faible élasticité, qui montre une réduction des constantes élastiques dans les composés avec le FA par rapport au MA, et aussi avec l'iode par rapport au brome. L'évolution des paramètres d'élasticité avec le paramètre de réseau permet aussi d'expliquer leurs conductivités thermiques ultra-basses, et de comprendre l'instabilité structurale de FAPI. Nous présentons également ici une comparaison détaillée des excitations optiques dans les quatre composés différents, dans laquelle nous discutons avec soin de l'attribution des modes de vibrations structurales respectives.

Contrairement aux attentes théoriques et au comportement classique des composés semi-conducteurs classiques, les modes de phonon ne montrent pas de dispersion, ce qui suggère un comportement anharmonique très fort et des effets de localisation. Ce comportement remet en question la validité de l'image de quasi-particule pour décrire les phonons utilisée dans l'interaction des porteurs de charges avec le réseau, c'est-à-dire la compréhension de l'interaction de Fröhlich pour la mobilité des porteurs. Par ailleurs, le recouvrement des modes acoustique avec les modes optiques de basses énergie peut aider à résoudre le paradoxe apparent de la dépendance en température de type phonons acoustiques de la mobilité des porteurs de charge et des processus directs dominants supposés être liés aux phonons optiques. Nos résultats mettent également en évidence le rôle du fort couplage anharmonique acousto-optique (responsable de la faible élasticité) dans la conductivité thermique faible, comme dans des phases vitreuses (glassy like) et l'effet de goulet d'étranglement des phonons dans les HOP. Cette étude expérimentale pourrait également fournir un solide point de départ pour des calculs théoriques permettant de mieux comprendre les propriétés fondamentales de ces matériaux

Titre : Structural and dynamic properties of hybrid organolead perovskites for photovoltaic applications

Keywords: Hybrid Perovskites ; Photovoltaics ; Spectroscopy ; Neutron diffraction

Abstract : This project focuses on the study of halide organolead perovskite (HOP) compounds, namely MAPbBr3, MAPbI3, FAPbBr3 and α-FAPbI3. To do this, we rely heavily on neutron inelastic scattering spectroscopy (INS), because it allows to systematically probe the structural properties of these materials. As a result, we are able to present a comprehensive investigation of lattice excitations (i.e. phonons) in the four of the most technologically relevant HOP compounds in the photovoltaics field. By measuring dispersion curves of acoustic phonons we give a clear picture of the difference in softness between FA and MA based compounds and how it relates to their structural stability and their ultralow thermal conductivities. We also present here an extensive comparison of optical phonon excitations in the four different hybrid, in which we carefully discuss mode attribution to the respective structural vibrations.

In contrast to theoretical expectation and classical behavior in standard semiconductor compounds, the phonon modes show no dispersion, suggesting strong anharmonic behavior and localization effects. This behaviour puts into question the validity of the quasi-particle picture used for phonon simulation and the present understanding of the Fröhlich interaction for carrier mobilities. This may help in solving the apparent paradox of acoustic-like temperature dependence of the charge carrier mobilities and dominant direct processes expected to be related to optical phonons. Our results also highlight the role of the strong acousto-optical anharmonic coupling (responsible for the characteristic low elastic stiffness) in the glassy-like thermal conductivities and hot-phonon bottleneck effect in HOPs. This experimental study could also provide a solid starting point for further theoretical calculations to understand the fundamental properties of these materials.